Dublin City University
School of Physical Sciences

Chemical investigations of ruthenium based barrier layer systems for future interconnect technologies

Anthony McCoy B.Sc., M.Sc.
Doctor of Philosophy
June 2014
Supervised by Professor Greg Hughes

Declaration

I hereby certify that this material, which I now submit for assessment on the programme of study leading to the award of doctor of philosophy is entirely my own work, that I have exercised reasonable care to ensure that the work is original, and does not to the best of my knowledge breach any law of copyright, and has not been taken from the work of others save and to the extent that such work has been cited and acknowledged within the text of my work.

Signed: _____ (Candidate)

ID No.: 50401251

Date: _____

Dedications and Acknowledgements

Thanks to the following:

My supervisor Greg Hughes for providing me with the opportunity to work with his group. His experience and knowledge in the field was essential to the successful completion of this work.

My wife Marie Claire for her patience, encouragement and support throughout the three years.

The team – Paddy, Justin, Lee, Conor and Rob - for teaching me to be a world leading expert in....everything. I can now debate the pro's and con's of any subject without any facts.

To my parents Peter and Miriam for sacrificing so much in providing me with the education necessary to embark on this project. Thanks also to my sister Bronagh.

To the excellent support team at DCU – Pat Wogan, Des Lavelle and Lisa Peyton.

I would like to acknowledge Science Foundation Ireland for the financial support of this work.

Publications arising from this work

Chemical and structural investigations of the incorporation of metal manganese into ruthenium thin films for use as copper diffusion barrier layers

AP McCoy, P Casey, J Bogan, JG Lozano, PD Nellist, G Hughes Applied Physics Letters **101** (23), 231603-231603-4 (2012).

Investigation of the release of Si from SiO_2 during the formation of manganese/ruthenium barrier layers

AP McCoy, P Casey, J Bogan, C Byrne, G Hughes Applied Physics Letters **102** (20), 201603-201603-4 (2013).

In-situ investigations into the mechanism of oxygen catalysis on ruthenium/manganese surfaces and the thermodynamic stability of Ru/Mn-based copper diffusion barrier layers

P Casey, AP McCoy, J Bogan, C Byrne, L Walsh, R O'Connor, G Hughes The Journal of Physical Chemistry C **117** (31), 16136-16143 (2013).

Scanning transmission electron microscopy investigations of self-forming diffusion barrier formation in Cu (Mn) alloys on SiO_2

JG Lozano, J Bogan, P Casey, AP McCoy, G Hughes, PD Nellist APL Materials **4**, 042105 (2013).

The addition of aluminium to ruthenium liner layers for use as copper diffusion barriers

A.P. McCoy, J. Bogan, L. Walsh, C. Byrne, P. Casey and G. Hughes. App. Sur. Sci **307**, 677-681 (2014).

Oxygen modification of carbon doped oxide surfaces for manganese silicate barrier formation

J. Bogan, A. P. McCoy, C. Byrne and G. Hughes (In preparation)

Photoemission study of the impact of carbon content on Mn-silicate barrier formation in ultra low-k dielectrics.

J. Bogan, A. P. McCoy, C. Byrne and G. Hughes (In preparation)

Table of Contents

Table of figures

and at the Ru surface. There is a much reduced Mn signal intensity in the Ru film itself suggesting that the Mn migrated through the film where it interacted with the SiO_2 substrate.

Figure 3.5 O 1s and Si 2p spectra taken from the Ru/SiO_2 surface following $Mn\text{-}MnO_x$ deposition and subsequent UHV thermal annealing treatments**.**

Figure 3.6 Mn 2p and Ru 3d spectra corresponding to figure 3.5. Mn 2p spectra showing no significant change after thermal anneal due to the conversion of Mn-oxide to Mn-silicate, both of which have similar BE positions. Ru 3d spectra (290 eV – 275 eV) show no change in profile during the experiment.

Figure 3.7(a) High resolution TEM image of the interfacial Ru layer and overlying $Mn\text{-}MnO_x$ layer on the SiO_2 substrate with the protective Cu capping layer. **(b)** Corresponding EDX analysis showing the presence of a Si signal in the Ru layer.

Figure 3.8 SIMS analysis taken from the $Mn\text{-}MnO_x/Ru/SiO_2$ structure following the completion of XPS analysis. SIMS profile shows the presence of a Si signal at the surface of the Ru film indicating the upward diffusion following Mn-silicate growth at the Ru/SiO_2 interface.

Figure 4.1 O 1s and Al 2p spectra taken from the Al/SiO_2 surface following Al deposition and subsequent UHV thermal annealing treatments**.**

Figure 4.2 Si 2p spectra taken from the SiO_2 surface following Al deposition and subsequent UHV thermal annealing treatments showing the reduction of the oxide and the presence of unbonded silicon.

Figure 4.3 O 1s and Al 2p spectra taken from the Al/3nm Ru/SiO_2 structure following Al deposition and subsequent UHV thermal annealing treatments.

Figure 4.4 Ru $3d_{5/2}$ and Si 2p spectra taken from the Al/3 nm Ru/SiO_2 structure. The Ru$3d_{5/2}$ shows the growth of an additional HBE component due to the interaction of Ru-O following thermal anneal. There is also evidence for peak broadening on the LBE side of the Ru $3d_{5/2}$. The Si 2p spectra show the emergence of released Si following a 400 ^{o}C thermal anneal.

Figure 4.5 Ru $3d_{5/2}$ and Si 2p spectra taken from deposited Si on a 3nm ALD Ru film. The spectra show the growth of Ru-silicide with thermal anneal.

Figure 5.1 Schematic diagram representing the three separate experimental samples analysed in this study. **(a)** represents the formation of a ~2 nm MnO layer on Ru (~10 nm) investigated in section 5.3. **(b)** represents the deposition of a Ru liner layer (~2 nm) onto a mixed phase MnO/$MnSiO_3$ barrier layer (~5 nm) and **(c)** represents the deposition of a Ru liner layer (~2 nm) onto a single phase $MnSiO_3$ barrier layer (~5 nm), both of which will be investigated in section 5.4.

Figure 5.2 Non-normalised and curve fitted Mn $2p_{3/2}$ XPS spectra taken following the deposition of a ~2 nm Mn film onto Ru and subsequent O_2 exposure and thermal annealing treatments. Spectra show the formation of metallic Mn and sub-stoichiometric Mn following 500 °C annealing, attributed to MnO dissociation.

Figure 5.3 Non-normalised and curve fitted O 1s and Ru $3d_{5/2}$ XPS spectra corresponding to Fig 5.1. MnO dissociation following 500 °C annealing is shown by a reduction in the integrated area of relevant O 1s MnO component peak, which results in a corresponding change in the attenuation of the Ru $3d_{5/2}$ peak. For the purpose of image clarity the intensity each of the Ru $3d_{5/2}$ spectra are magnified by a factor of 1.6.

Figure 5.4 Normalised and curve fitted O 1s and Si 2p XPS spectra showing the interaction of Ru (~2 nm) with a mixed phase MnO/$MnSiO_3$ barrier layer (~5 nm). O 1s spectra show the dissociation of MnO within the barrier layer following interaction within Ru at 500 °C.

Figure 5.5 Normalised and non-curve fitted Mn $2p_{3/2}$ XPS spectra corresponding to Fig 5.3. Spectra show the formation of metallic Mn following MnO dissociation at 500 °C.

Figure 5.6 Normalised and curve fitted O 1s and Si 2p XPS spectra showing the interaction of Ru (~2 nm) with a single phase $MnSiO_3$ barrier layer (~5 nm).

Figure 5.7 Normalised and non-curve fitted Mn $2p_{3/2}$ XPS spectra corresponding to Fig 5.5. The Mn $2p_{3/2}$ spectrum taken following 500 °C annealing in the presence of Ru has been overlaid with the Mn $2p_{3/2}$ spectrum taken from the $MnSiO_3$ barrier layer (solid line) in order to clearly show the formation of metallic Mn in the absence of relevant curve fitting parameters.

Figure 6.1 Si 2p spectra taken from Si deposited on multiple carbon doped oxide surfaces showing substrate shift to LBE with increasing carbon content.

Figure 6.2 Curve fitted Si 2p spectra taken from 5nm SiO_2, $MnSiO_3$ on SiO_2 and as received 'CDO 48' highlighting the difficulty in confirming silicate formation on high carbon content carbon doped oxide surface.

Figure 6.3 Curve fitted O 1s spectra taken from MnO deposited on multiple carbon doped oxide surfaces showing a similar shift to L.B.E with increasing carbon content as observed in Figure 6.1. There is a ~1.2 eV binding energy separation between MnO and $MnSiO_3$.

Figure 6.4 Mn 2p spectra of Mn oxide deposited on various substrates. Spectra show the reproducibility of deposited Mn oxide across multiple samples and can be used as a chemical reference within O 1s spectra.

Figure 6.5 Curve fitted O 1s spectra showing Mn-silicate growth on SiO_2 after thermal anneal.

Figure 6.14(a) Ru 3d, C 1s and Si 2p spectra taken from a Ru/Mn barrier/liner bilayer deposited on a high porosity carbon doped oxide surface.

Figure 6.14(b) Ru 3d, C 1s and Si 2p spectra taken from a thin Ru/Mn barrier/liner bilayer deposited on a high carbon content carbon doped oxide surface.

Chemical investigations of ruthenium based barrier layer systems for future interconnect technologies

Anthony Peter McCoy

Abstract

This thesis utilises X-ray photoelectron spectroscopy (XPS) to investigate the chemical interactions of Ru and Mn based Cu diffusion barrier layer structures with dielectric substrates with a view to incorporating these materials into future generations of interconnect technology. The current barrier layer arrangement of Ta/TaN will imminently fail to meet the demanding requirements associated with aggressive device miniaturization. The first part of the thesis investigates the incorporation of manganese into a 3 nm Ru thin-film as a potential mechanism to improve its performance as a copper diffusion barrier/liner combination layer. Mn and Al (~1 nm) were deposited in separate studies on an atomic layer deposited (ALD) Ru film and the Metal/Ru/SiO_2 structures were subsequently thermally annealed. XPS studies revealed the chemical interaction of both Mn and Al with the SiO_2 substrate to form $MnSiO_3$ and Al_2O_3 respectively, implying the migration of both metals through the Ru film. Electron energy loss spectroscopy (EELS) line profile measurements of the intensity of the Mn signal across the Ru film confirm the presence of Mn at the Ru/SiO_2 interface. In addition, secondary ion mass spectroscopy (SIMS) studies suggest the release and upward diffusion of Si from the SiO_2 dielectric substrate formed as a result of Mn-silicate formation at the Ru/SiO_2 interface. The second part of the thesis provides direct experimental evidence of the catalytic activity of bimetallic Ru/Mn surfaces towards oxygen and determines how this activity impacts upon the thermodynamic stability of Ru/Mn based Cu diffusion barrier layers. XPS analysis showed the thermal dissociation of Mn-based barrier layers and the desorption of O in the presence of Ru at lower temperatures than in systems without Ru present. Finally, XPS analysis of Ru/Mn on industrially relevant dielectric materials with varying carbon content and porosity is presented, along with the reduction of surface C concentration through exposure to atomic O.

Chapter 1

Introduction

1.1 Moore's Law

In 1965 one of the co-founders of Intel, Gordon Moore, published a paper noting that the number of components in integrated circuits (IC's) had doubled every year from 1958 through 1965, and he predicted the trend would continue for 'at least 10 years'.[1,2] The semiconductor industry adopted Moore's prediction and used it as a guide for long term planning and target setting. Consequently, the number of transistors on a single chip has doubled every two years in a relentless fashion through to the present day, and as such, Moore's prediction became somewhat of a self-fulfilling prophecy. The exponential reduction in component size greatly improves the capabilities of digital electronic devices such as processing speed and memory capacity, and has impacted society on almost every level. Figure 1.1 shows the increase in the number of transistors on a single chip from 1971 through 2011. Current transistor counts for high specification microprocessors range between ~2 billion (e.g. Intel Core i7) and ~5 billion (e.g. 62 core Xeon Phi). It is believed that the chip sector is rapidly approaching an end to Moore's law due to the physical limits imposed by the size of the silicon atom, and hence the size of the transistor itself.

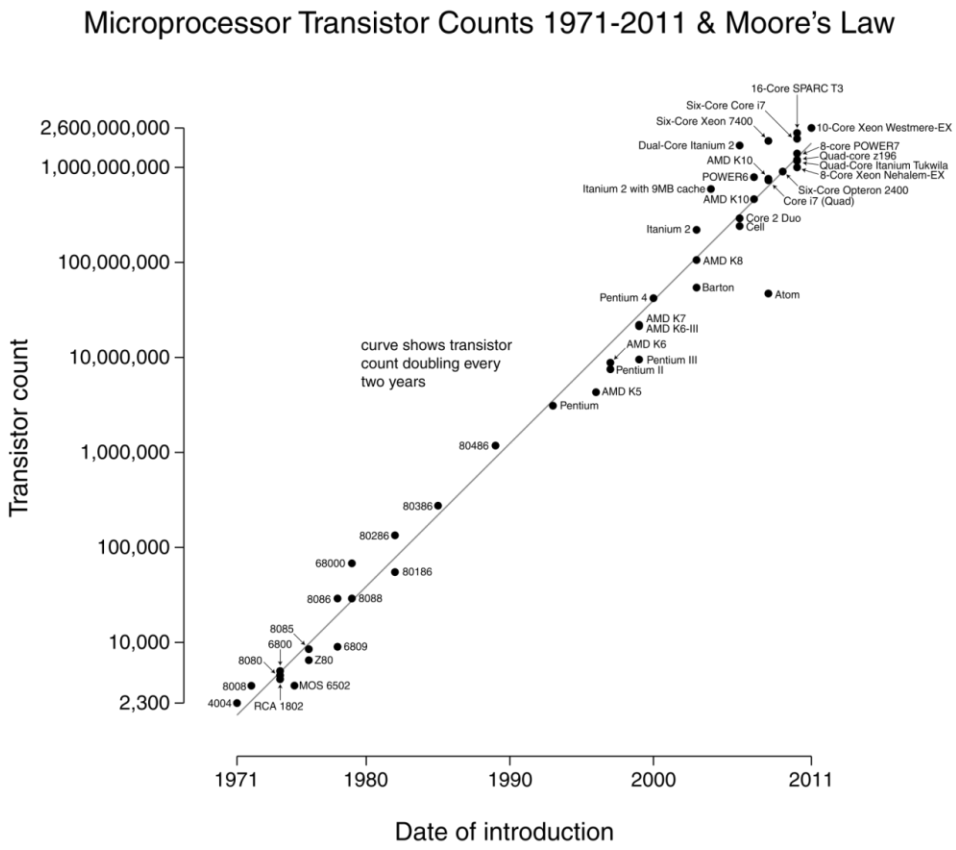

Figure 1.1 Graph of transistor count on a single chip from 1971 to 2011.[3]

1.2 Interconnect overview

The construction of an integrated circuit can be divided into two main processing steps; (1) front-end-of-line (FEOL) and (2) back-end-of-line (BEOL). FEOL processing refers to the formation of the transistors directly in the ultrapure silicon wafer. Once the transistors have been fabricated, they must then be interconnected to form the desired electrical circuits. This occurs in a series of processing steps collectively referred to as BEOL. The structure of a typical chip is illustrated graphically in Figure 1.2 with the

areas manufactured by FEOL and BEOL processes labeled. BEOL processing involves creating metal interconnecting wires that are isolated by dielectric layers. Historically, Al has been used as the interconnecting metal because of its low resistivity (2.7 μΩ/cm) and well established and reliable production process. Silicon dioxide (SiO_2) was used as the interlayer dielectric (ILD) material as it was very well characterised and easy to deposit and etch. However, diffusion of Al into the surrounding ILD has been a problem since the fabrication of the first IC in 1959.[4] Silicon is soluble in Al[5] which resulted in inter-diffusion, high leakage current and device shorting. The solution to this interdiffusion problem came in the form of a physical barrier layer inserted between the ILD and the metal Al lines. For much of the 80's and 90's a combination of Ti and Ti-nitride were successfully adopted as the barrier layer structure.

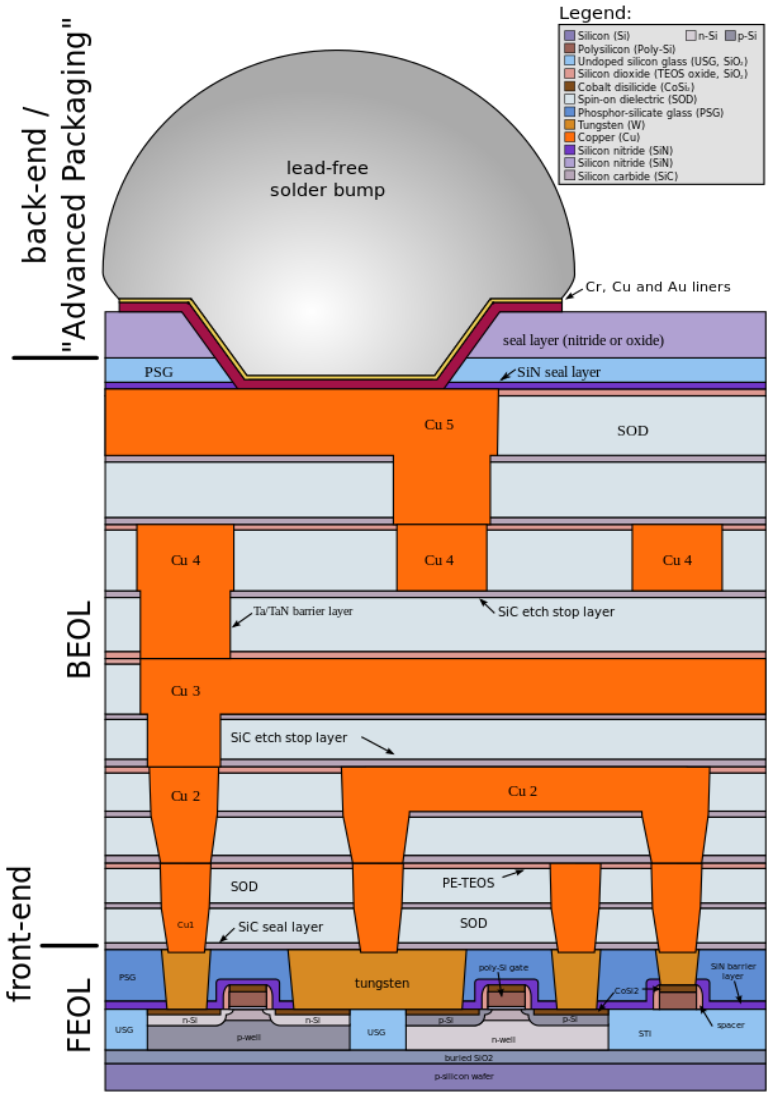

Figure 1.2 Schematic diagram of a microprocessor with a hierarchical wiring approach for multilevel interconnects.[6]

1.3 RC time constant

The miniaturisation of device features greatly enhances chip performance, mainly as a result of shortening proximity between adjacent transistors leading to a decrease in gate switching delay. However, as the gate delay

decreases, other elements of the device begin to have a proportionately larger impact on performance. For example, the electrical resistance of the interconnects increases as the cross sectional area of the wires are reduced to facilitate increased numbers of devices (Equation 1.1),

$$R = \frac{\rho L}{A} \tag{1.1}$$

where R is the reistance of a line of length L and cross-sectional area A for a material with resistivity ρ. Additionally, the capacitance between adjacent lines as a result of increased wire density also impacts negatively on device speed (Equation 1.2), as the thickness of the dielectric layers must also decrease,

$$C = \frac{\varepsilon_0 \varepsilon_R l w}{D} \tag{1.2}$$

The increase in both wire resistance and capacitance contributes to a deterioration in interconnect delay also known as the RC time constant, defined as the product of the resistance and the capacitance.[7,8] Figure 1.3 illustrates the increasing impact of RC delay on IC performance with decreasing feature size.

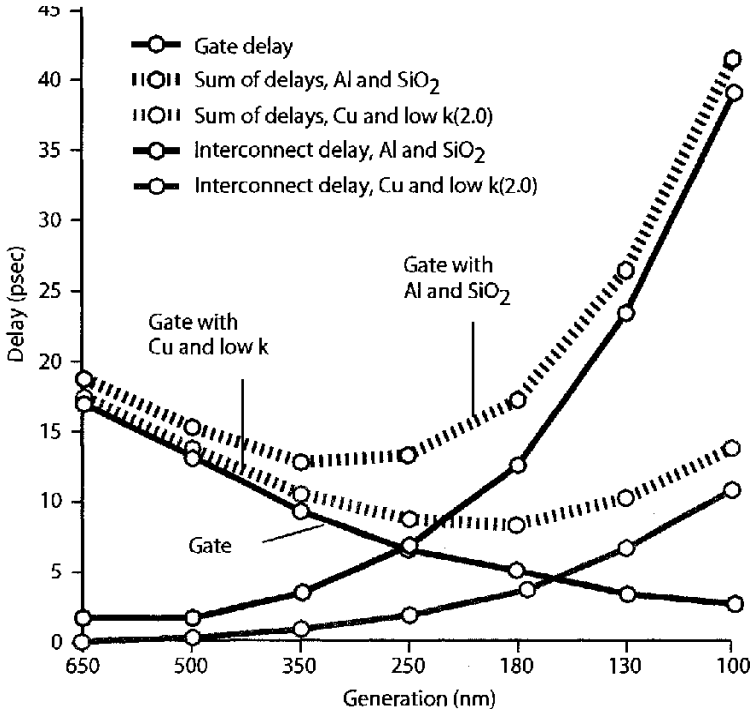

Figure 1.3 RC delay as a function of the gate length. The gate delay can be reduced by decreasing the feature size. The interconnect delay (RC delay) starts to dominate the overall delay at shorter feature size.[6]

As seen from Equations 1.1 and 1.2, the RC time constant can be improved by reducing the resistivity of the interconnecting metal and/or using a dielectric material with a lower dielectric constant. Both of these methods have been adopted in recent years by the IC processing industry. Cu has replaced Al as the interconnect metal of choice due to its lower resistivity (Cu: 1.7 μΩ /cm, Al: 2.7 μΩ /cm),[9] and lower dielectric constant materials have replaced SiO_2 in attempts to improve device performance.

1.4 Cu diffusion barrier

Although copper improves the conductivity and the RC time constant of the interconnect, implementation problems exist. Cu readily diffuses into interlayer dielectrics (ILD) due to the formation of Cu oxides, and is also known to have poor adhesion to dielectric surfaces.[10,11] The diffusivity of Cu in Si ranges from $5x10^{-14}$ to $5x10^{-4}$ cm^2s^{-1} with activation energy of ~1 eV for temperature ranges of 900 ^oC to 1300 ^oC. These high diffusion rates of elemental Cu have necessitated the further development of physical barrier layers between the dielectric and the interconnect in order to prevent interdiffusion across the interface. It has been reported that Cu diffusion in Si degrades device performance by introducing deep electronic levels into the Si band gap resulting in the reduction in the minority carrier lifetime.[12]

The optimal barrier needs to meet a range of criteria; (1) limit Cu diffusivity, (2) be conformal, (3) exhibit resistance to mechanical stress, (4) display good Cu wetting/adhesion properties and most importantly (5) have low resistivity. The barrier layers currently used to fulfil this function are composed of a $Cu/Ta/TaN/SiO_2$ layered structure as shown in Figure 1.4. The Ti/TiN barrier layers used for Al were no longer effective as a barrier against Cu diffusion due to the formation of bulk alloy between the Cu and Ti. However, as device geometry continues its downward trend, there is a need to develop a scalable alternative to the current barrier layer

arrangement to Ta/TaN as they tend to have poor electrical conductivity and exhibit poor adhesion to the Cu necessitating inclusion of a copper seed layer. As device miniaturisation continues, the thickness of the barrier layer region becomes important - too thick a barrier and the overall barrier metal/Cu film will have a greater total resistance than Al interconnects, negating any benefit. As such, the barrier layer should be as thin as possible. Additionally, the deposition of barrier layers will need to evolve from the current Physical Vapour Deposition (PVD) process to a more conformal alternative such as Atomic Layer Deposition (ALD). Non-uniform coverage of sidewalls and trenches will eventually limit further thickness reduction in conventional PVD layer deposition.

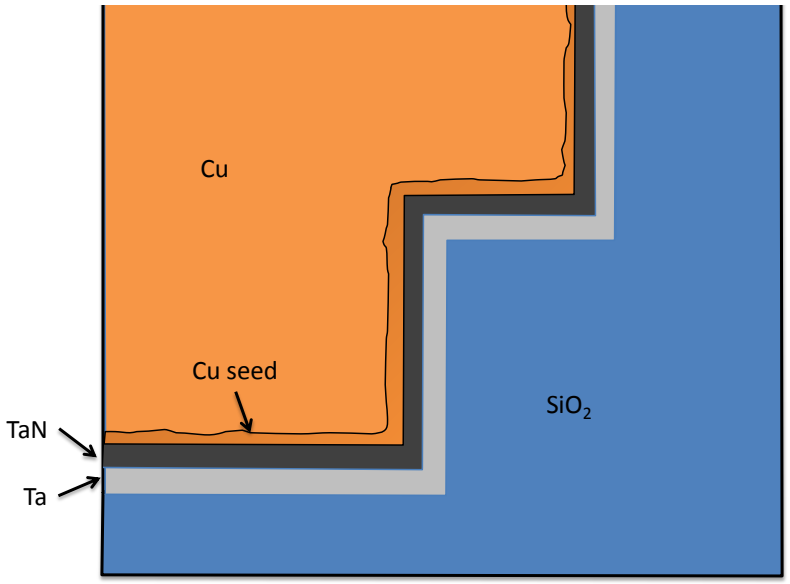

Figure 1.4 Current barrier layer technology using Ta/TaN barriers.[13] The Ta/TaN (~10 nm) layers are incorporated to both stop Cu diffusion into the dielectric and promote Cu wetting.

1.5 Ru-based barrier layers

The noble metal Ru has emerged as a promising candidate for incorporation into future interlayer material systems for back end of line (BEOL) processing, due to its compatibility with conformal deposition techniques such as atomic layer deposition (ALD). Ru also displays more favourable bulk resistivity characteristics (ρ ~7 $\mu\Omega$ cm) than α-Ta (~15-30 $\mu\Omega$ cm) and it is a suitable seed layer for the subsequent electrochemical plating of copper.[14,15] It has been reported, however, that Ru displays poor diffusion barrier properties to Cu at moderate temperatures due to its polycrystalline columnar grain structure which facilitates Cu diffusion through the grains.[16,17] Single-crystal films would provide suitable Cu diffusion barriers while simultaneously displaying superior electrical properties as a result of the reduced grain boundary density, but restrictions regarding materials and manufacturing processes make such an option unlikely. A second potential solution to the Cu diffusion problem in Ru films involves the use of amorphous films, which would also be void of grain boundaries, however the reduced conductivity of such films is undesirable. The concept of 'stuffing' the grain boundaries has also been presented as a possible mechanism to improve the diffusion properties of ultra-thin metal films.[18,19,20] A recent study by Damayanti et. al[19] showed that introducing nitrogen in the Ru film effectively stuffed the grain boundaries and improved the films resistance to Cu diffusion. Similarly, Henderson et al[18]

have used phosphorus to improve thin film properties. As such, the focus of the first two results chapters of this thesis is to investigate the possibility of incorporating the metals manganese and aluminium into Ru thin films as a mechanism of improving the diffusion barrier characteristics of Ru. The third results chapter looks at the thermodynamic stability of Ru/Mn based copper diffusion barrier layers. Finally, the fourth results chapter investigates the formation of Mn-based barrier layers with Ru liners on industrially relevant ultra low dielectric constant (ULK) substrates. It should be noted that Cobalt (Co) has also attracted attention as a replacement liner material.[21]

1.6 References

[1] "Cramming more components onto integrated circuits". Electronics Magazine. p. 4. 2006-11-11.

[2] "Excerpts from A Conversation with Gordon Moore: Moore's Law" (PDF). Intel Corporation. 2005. p. 1. Retrieved 2013-09-12.

[3]http://commons.wikimedia.org/wiki/File:Transistor_Count_and_Moore%27s_Law_-_2011.svg

[4] J. R. Black, "Metallization Failures In Integrated Circuits," RADC Technical Report (1968).

[5] T. Gupta, *Copper Interconnect Technology*, 1st ed. Springer (2009).

[6] Growth and chemical characterisation studies of Mn silicate barrier layers on SiO2 and CDO, Justin Bogan, PhD Thesis, Dublin City University (2011).

[7] M. Liu, "Pore characterization of ultralow-k dielectric thin films using positronium annihilation spectroscopy," PhD Thesis (2008).

[8] K. Buchanan, "The evolution of interconnect technology for silicon integrated circuitry", *GaAsMANTECH Conference* (2002).

[9] (2011, Oct.) Wolfram Alpha. [Online]. http://www.wolframalpha.com/

[10] Phuong, N. M.; Sutou, Y.; Koike, J.; Structural Characterization of a Manganese Oxide Barrier Layer Formed by Chemical Vapor Deposition for Advanced Interconnects Application on SiOC Dielectric Substrates, *J. Phys. Chem. C* ***117***, 160-164 (2013).

[11]Au, Y,; Lin, Y.; Kim, H.; Beh, E,; Liu, Y,; Gordon, R.G.; Selective Chemical Vapor Deposition of Manganese Self-Aligned Capping Layer for Cu Interconnections in Microelectronics *J. Electrochem. Soc*. ***157***, D 341-D 345 (2010).

[12] J. Baumann. et. al., "Investigation of Copper Metallization Induced Failure of Diode Structures with and without Barrier Layer," *Microelectronic Engineering*, vol. **33**, pp. 283-291 (1997).

[13] H. Y. Wong, N. F. Mohd Shukor, and N. Amin, "Prospective development in diffusion barrier layers for copper metallization in LSI," *Microelectronics Journal* , vol. 38, pp. 777-782, Jun. 2007.

[14] D. Josell, D. Wheeler, C. Witt and T. P. Moffat, Electrochem. Solid-State Lett. Volume **6**, Issue 10, Pages C143-C145 (2003).

[15] O. Chyan, T. N. Arunagiri, and T. Ponnuswamy, Journal ElectrochemSoc, **150**, C347-C350 (2003).

[16] T. N. Arunagiri, Y. Zhang, and O. Chyan, M. El-Bouanani and M. J. Kim, K. H. Chen, C. T. Wu and L. C. Chen, Appl. Phys. Lett. **86**, 083104 (2005).

[17] M. Damayanti T. Sritharan, Z. H. Gan,S. G. Mhaisalkar, N. Jiang, and L. Chanb, Journal ElectrochemSoc, **153**, 6, J41-J45 (2006).

[18] Arindom Datta, Ki Tae Nam, Soo-Hyun Kim, and Ki-Bum Kim, J. Appl. Phys. **92**, 1099 (2002).

[19] M. Damayanti (2), T. Sritharan, S. G. Mhaisalkar, and Z. H. Gan, Appl. Phys. Lett. **88**, 044101 (2006).

[20] Lucas B. Henderson, John G. Ekerdt, Thin Solid Films **517**, 1645–164 (2009).

21 F. Inoue, H. Philipsen, M.H. van der Veen, S. Van Huylenbroeck, S. Armini, H. Struyf and T. Tanaka, IEEE International Interconnect Technology Conference, San Jose CA (2014).

Chapter 2

Analysis techniques and theory

2.1 X-Ray Photoelectron Spectroscopy

The dominant technique used in this study was x-ray photoelectron spectroscopy (XPS). The technique offers the capability to determine and analyse the chemical composition of a material to a depth of approximately 5 – 10 nm from the surface. XPS is a highly surface sensitive analytical tool. The operation of XPS involves the irradiation of a target sample with mono-energetic X-rays, resulting in the emission of electrons from the sample in question as described by the photoelectric effect[1] and as shown in Figure 2.1. The kinetic energy of the emitted electrons are indicative of the environment from which they originated, enabling the user to execute an in-depth analysis of the chemical structure of the sample.

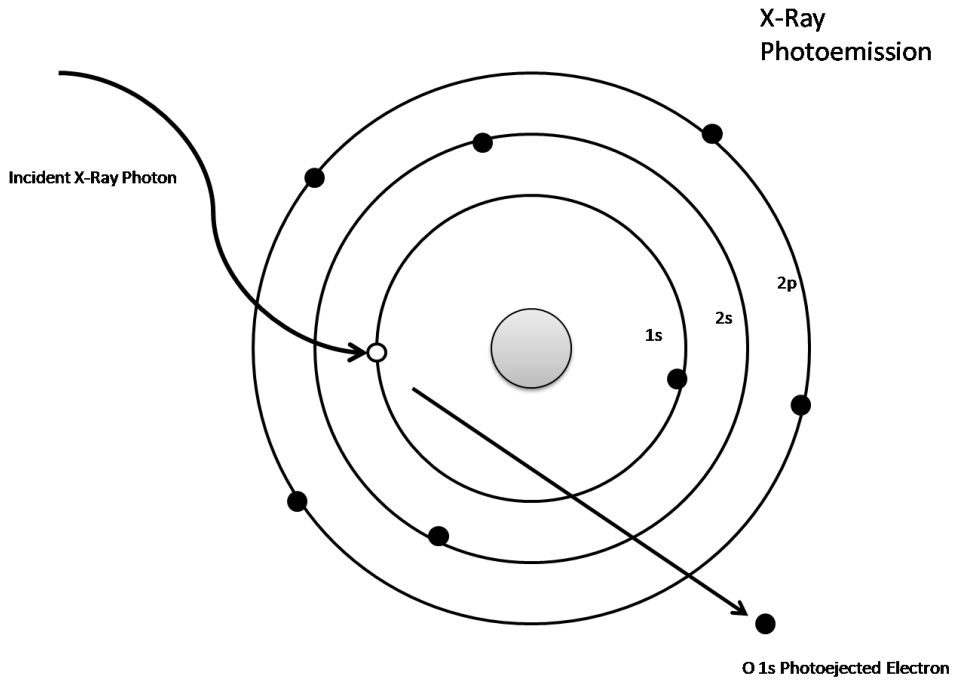

Figure 2.1 Schematic showing photoemission of an electron from the O 1s orbital.

Conventional XPS setup consists of an x-ray source, an electron collection lens and an electron kinetic energy analyser as shown in Figure 2.2. A water cooling system is integrated into the setup as x-ray generation can cause significant heating. Results are processed and displayed on a generic PC with the appropriate acquisition software installed. The sample under analysis is irradiated by x-rays from the source, and electrons are emitted from the surface of the sample which are collected and analysed by the collection lens and the electron analyser, respectively.

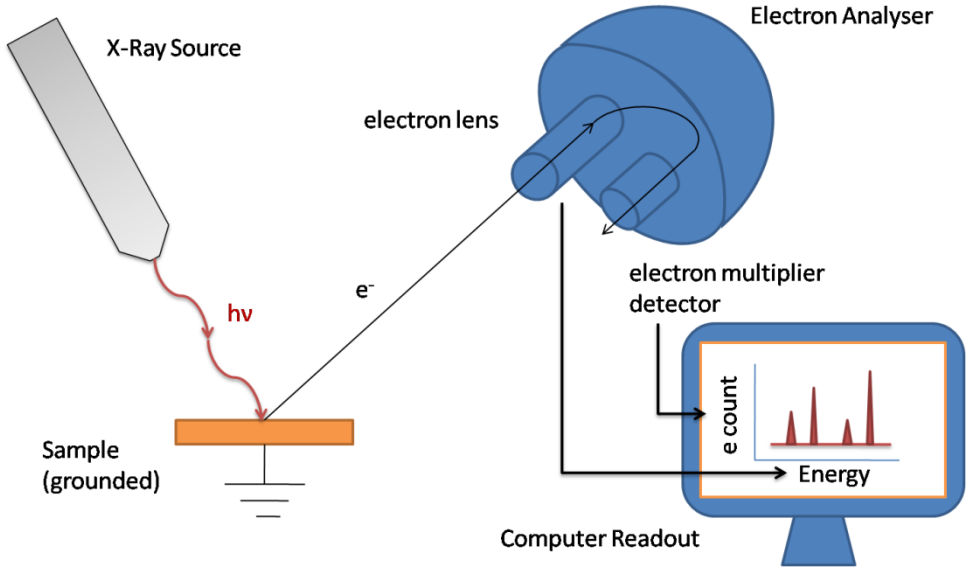

Figure 2.2 A schematic diagram showing the experimental setup for conventional XPS.

The typical XPS setup includes the ability to generate x-rays of two different excitation energies, which can add to the usefulness of the technique, and is made possible by a twin anode x-ray source. The most commonly used anode materials for x-ray generation are either Mg or Al. X-rays are generated by electrons from a hot tungsten filament impinging on the anode material having been accelerated through a strong electric field generated by an applied voltage in the region of 10-15 kV. The excitation energies of the generated x-rays are either 1256.6 eV (Mg K_α) or 1486.6 eV (Al K_α) depending on the choice of anode material. Electrons bound to the atoms in the surface region of the sample are excited by the incoming x-rays, and if excited by sufficiently high energy, they break free of their

parent atoms and are released from the material. The kinetic energy (*KE*) of the photoemitted electrons is described by Einstein's equation;

$$KE = hv - E_b \qquad \text{Equation 2.1}$$

where E_b is the binding energy of the electron in the atom with respect to the Fermi level and hv (plancks constant x frequency) is the energy of the photon from the X-ray source. As both the photon energy and the electron binding energy are well defined, elemental identification of the atom from which the electrons originated can be determined, as every energy level of each element has a known discrete binding energy. A comparison exercise between the measured binding energy and well established published binding energy positions, reveals the atomic origin of the electron.

An energy level diagram for the full photoemission and analysis process is illustrated in Figure 2.3 for a sample and spectrometer which are in electrical contact. From Figure 2.3 it can been deduced that the sum of the electrons initial binding energy measured up to the Fermi level (E_B^F), and its kinetic energy after being emitted (E_{Kin}^1), does not equal the photon energy of the impinging x-rays.

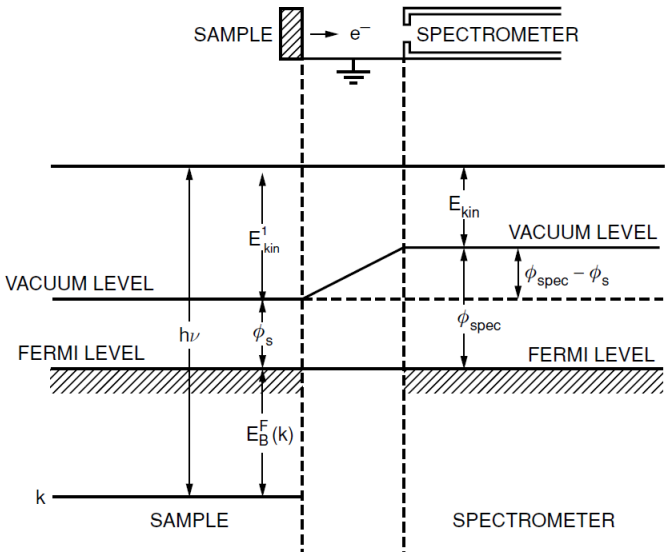

Figure 2.3 Energy level diagram for the photoemission process showing sample and spectrometer in electrical contact.[2]

Equation 2.2 shows that the workfunction of the sample Φ_S, defined as the energy difference between the vacuum level and the Fermi level ($E_{vac} - E_f$), must be considered when defining the kinetic energy of electrons emitted from the sample.

$$h\nu = E_B^F + E_{Kin}^1 + \Phi_s \qquad \text{Equation 2.2}$$

While Equation 2.2 relates to the actual kinetic energy of the emitted electrons, Feldman and Mayer[3] explain how the measured kinetic energy value (E_{kin}) may differ from this. It has been shown that an electron passing from the sample to the spectrometer experiences a potential difference, equal to the difference between the workfunction of the sample Φ_s and that

of the spectrometer Φ_{spec}. The measured kinetic value can therefore be defined by;

$$E_{Kin} = E^{1}_{Kin} + (\Phi_s - \Phi_{spec}) \qquad \text{Equation 2.3}$$

By substituting this into equation 2.2, the following expression emerges;

$$hv = E^{F}_{B} + E_{Kin} + \Phi_{spec} \qquad \text{Equation 2.4}$$

The kinetic energy of electrons emitted from the sample may be changed by atomic collisions and phonon interactions which can occur within the solid before the photo-excited electrons emerge from the surface. The probability of such interactions can be statistically predicted based on the inelastic mean free path (IMFP) of the material, which is defined as the average distance (nm) that an electron travels between successive inelastic collisions. This is represented by the universal mean free path curve shown in Figure 2.4.

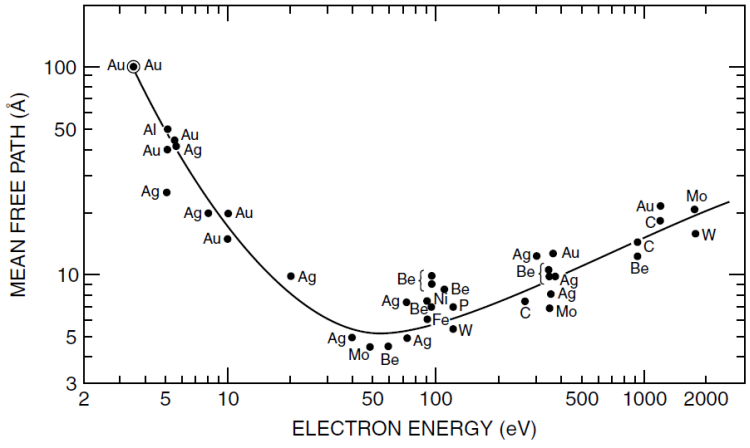

Figure 2.4 Universal mean free path (MFP) curve for electrons in a solid, showing a range of materials and their respective mean free paths for a few selected electron energies.[4]

Only electrons which reach the analyser without suffering inelastic collisions have kinetic energies which can be related back to the original binding energy value. Therefore, in photoemission experiments, useful information may only be obtained from the first 5 – 10 nm of the surface, making the technique highly surface sensitive. Unscattered electrons produce narrow and intense photoemission peaks, such as those shown in the survey scan of ruthenium on a SiO_2 substrate in Figure 2.5. The binding energy of these peaks can be related to the elements present at the surface. Electrons which have lost energy due to inelastic collisions emerge from the sample with a spread of lower kinetic energies, which add to the background of the spectrum. This loss function is strongly dependent on the material in question and a number of models have been developed to account for the shape of the background. The most common function used in this regard is known as the Shirley type background. The shape of an XPS spectrum is also influnced by electrons which have lost energy due to the interaction with other core level electrons, known as shake-up features. Additional contributions to the shape of a spectrum include Satillite and Ghost peaks which arise as a result of the non-monochromated nature of the x-ray source. Finally, secondary electrons such as Auger electrons are a common feature of a typical XPS spectrum.

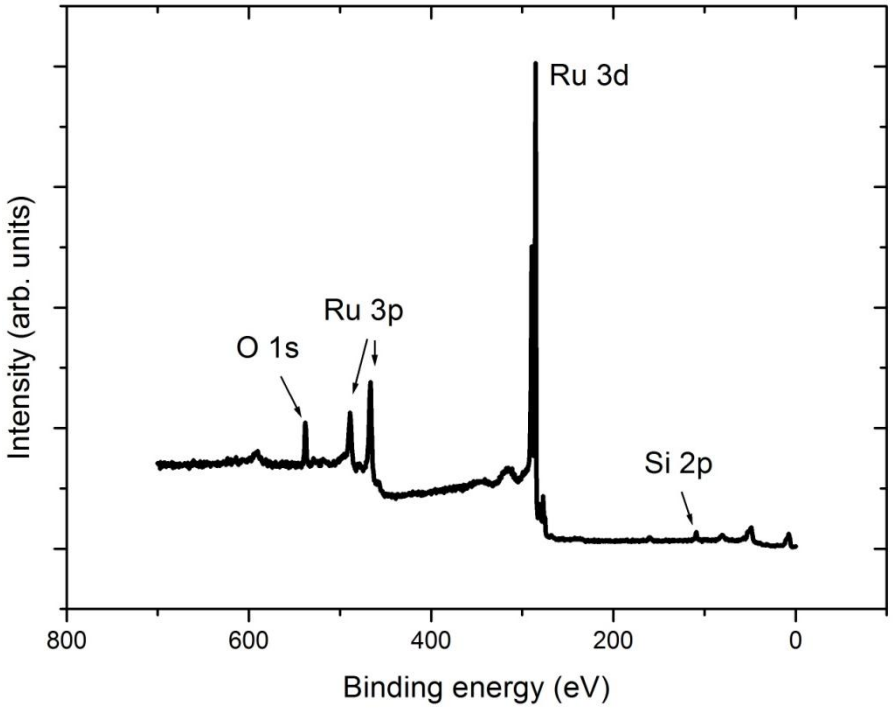

Figure 2.5 Survey scan taken from a 3nm ALD Ru film deposited on a SiO_2 substrate. By analysing the binding energy positions of the photoemission peaks the elements Ru, O and Si can be identified.

XPS measurements of a material allow identification of the presence of elements which are at atomic concentration levels greater that approximately 0.2 – 1%. It is common for elements to be identified and quantified by the strongest spectral feature present in the data. In the case of Ru for example, the strongest peak is the Ru 3d as illustrated in Figure 2.5. Quite often the occurrence of overlapping peaks is encountered where the binding energy of one elemental peak arises at or close to the binding

energy of another - as is the case of the C 1s peak (BE 285 eV) and Ru 3d (BE 284 eV). Under such circumstances, the presence of secondary core level features, such as the Ru 3p, may be used in elemental identification.

Semi-quantitative analysis of the relative concentration of different elements in a material can be achieved by comparing the intensity of the relevant core level peaks. However, there are a number of factors which must be taken into account in order to quantify chemical composition using XPS peak intensities. This is analysed in further detail in reference to Mg 2p and O 1s spectra taken from an MgO thin film deposited in Si (111) shown in Figure 2.6

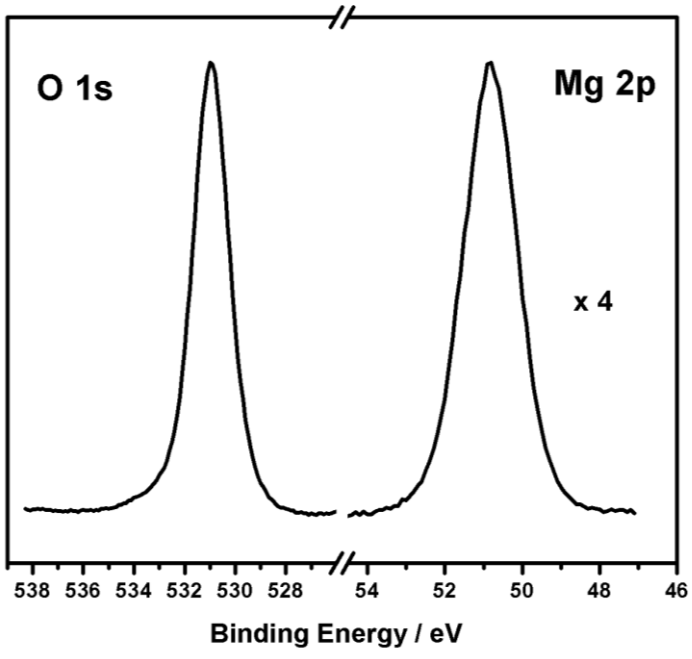

Figure 2.6 O 1s and Mg 2p spectra taken from a 20 nm stoichiometric MgO thin film.

In order to determine stoichiometry using spectra in Figure 2.6 it must be assumed that the MgO film is chemically homogenous, as if the chemical composition perpendicular to the surface is non-uniform within the XPS sampling depth, no definite elemental ratios can be extracted. The relative binding energies of the two peaks also must be taken into account given that the electron IMFP is strongly dependent on kinetic energy. As such, it can be said that the electrons emerging from the Mg 2p peak (BE 50 eV, KE 1200 eV) may emerge from a greater depth than O 1s electrons (BE 531 eV, KE 720 eV). Further factors include the photo-ionisation cross-section of that specific core-level which is the probability that an electron of that core-level will be photoexcited by the incident x-ray.[5] Finally, the transmission function of the analyser which determines the relative sensitivity of the analyser to electrons of different kinetic energies, must be accounted for.

Based on these criteria, relative sensitivity factors (RSF) can be obtained for core level peaks of each element allowing chemical compositions to be analysed using RSF values. Published RSF values are available from XPS reference manuals[6] and allow semi-quantitative analysis of chemical composition to be achieved. In reference to the spectra in Figure 2.6, the published RSF values of O 1s and Mg 2p are 0.711 and 0.129 respectively.[6] Therefore, for stoichiometric MgO, the integrated area of the O 1s peak should be 5.5 times greater than that of the Mg 2p. This analysis is at best semi-quantitative and the use of reference materials is common for more

accurate quantification studies. In this study, quantitative analysis has been performed in an attempt to directly compare various samples, rather than for the purpose of extracting absolute values.

The ability of XPS to distinguish between different chemical environments of the same element is an extremely powerful characteristic of the technique. This is made possible as the binding energy of an electron within an atom depends on the immediate bonding environment of that atom. The charge density around an atom is greatly influenced by changes in the chemical bonding environment, which can subsequently manifest as a 'chemical shift' in the binding energy positions of electrons in XPS spectra. This process is outlined in Figure 2.7 using the silicon/silicon dioxide system as a reference.

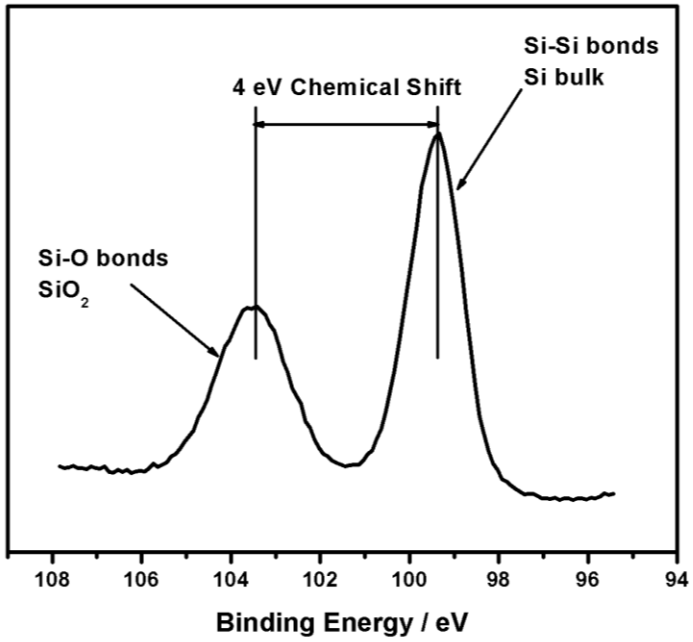

Figure 2.7 Si 2p spectrum showing a 4 eV chemical shift between component peaks which indicates the presence of Si and SiO_2.

The Si 2p spectrum was taken from a 4 nm SiO_2 thin film thermally grown on a Si(111) substrate. It can be seen that electrons emerging from the Si substrate appear at a binding energy position of 99.3 eV, while electrons arising from the SiO_2 thin film appear at the higher binding energy position of 103.3 eV. Both of these peaks are representative of the same Si 2p core level electrons chemically shifted due to the difference in the bonding environment from which they originated. The Si-Si bonding system in the bulk creates an environment where the valence electrons can be shared equally among each Si atom in the structure. Comparatively, the SiO_2

structure contains oxygen resulting in the transfer of electron density as a consequence of the greater electronegativity of the O atoms. The result of this is that Si-O bonds are more ionic and so excited Si 2p electrons arising from the SiO_2 are ejected from the more positively charged silicon atoms than those emerging from the Si bulk. The effect of this positive charge manifests as a reduction in the kinetic energy of the emitted electrons, or an increase in the binding energy of the SiO_2 peak. In summary, the relative electronegativity values of elements within a sample can be used to identify chemical composition. Chemical shift scan occur on both the higher binding energy (HBE) side and the lower binding energy (LBE) side of spectral components, revealing valuable chemical information.

XPS measurements may also be used to approximate the thickness of thin films by comparing the intensity of core level peaks taken from the film and the substrate. The thickness of the overlayer can be estimated by evaluating the suppression of the substrate peak after the growth of a thin overlayer. Thickness calculations may be simplified in a situation where the same element is present in distinguishably different chemical environments, e.g.an SiO_2 layer on a silicon substrate.

For a sample of material *A* which forms a thin uniform layer of thickness *d* on a substrate of material *S*, the following equation can be written for the

relative intensity of the substrate (I_S) and overlayer (I_A) XPS signals (assuming exponential attenuation of the overlayer).[7,8]

$$\frac{I_A}{I_S} = \frac{I_A^{\infty}\left\{1-exp\left[\frac{-d}{\lambda_{A,A}(\cos\theta)}\right]\right\}}{I_S^{\infty} exp\left[\frac{-d}{\lambda_{S,A}(\cos\theta)}\right]} \qquad \text{Equation 2.5}$$

This equation can be used to determine the thickness of deposited films. The emission angle of the excited electrons, θ, in equation 2.5 is measured with respect to the surface normal. Factors I^{∞}_A and I^{∞}_S are peak intensities taken from samples of materials A and B of effectively infinite thickness. The parameters $\lambda_{A,A}$ and $\lambda_{S,A}$ are the effective attenuation lengths of electrons in the overlayer emerging from the overlayer and the substrate, respectively.[9] The effective attenuation length (EAL) is known to differ from the inelastic mean free path (IMFP) due to elastic-scattering which causes the photoelectrons signal to decay in a non-exponential manner.[10] This variation from the IMFP value is dependent on the composition of the sample but, in general, changes in physical properties such as an increased density will result in a reduction of the EAL. In the case of SiO_2 on Si, where the kinetic energy of the substrate and overlayer signals differ by approximately 4 eV, the values $\lambda_{A,A}$ and $\lambda_{S,A}$ are approximately equal and can be replaced by a single term λ.[9] Making d the subject of equation 2.6;

$$d = \lambda \cos\theta \, ln\left[1 + \frac{\left(\frac{I_A}{I_A^{\infty}}\right)}{\left(\frac{I_S}{I_S^{\infty}}\right)}\right] \qquad \text{Equation 2.6}$$

The ratio $\frac{I_S^\infty}{I_A^\infty}$ can be referred to as *K*,[9,11,12] the ratio of the infinite intensities, leaving;

$$d = \lambda \cos\theta \,.\, ln\left[1 + K\left(\frac{I_A}{I_S}\right)\right] \qquad \text{Equation 2.7}$$

As stated previously, equation 2.7 relates only to situations where the kinetic energy of the substrate and overlayer peaks are comparable. In this study equation 2.7 was used to calculate the thickness of Si oxide overlayers on Si, with the parameter *K* being found experimentally using SiO_2 and Si samples of effectively infinite thickness. A value for λ can be found in the literature.[9] Thickness calculations based on this method can be achieved using software such as the NIST Electron EAL Database.[13]

The non-destructive depth profiling of a samples surface can be accomplished within the sampling depth of the equipment using angular resolved XPS (ARXPS). Previous discussions relating to the emission of photoelectrons assume that they escape using the shortest path, which is perpendicular to the sample surface. Therefore, the maximum sampling depth is achieved by aligning the sample so that the electrons which emerge normal to the surface are detected by the analyser. However, electrons emerging from shallower angles with respect to the surface may also be analysed by rotating the sample relative to the analyser. This is graphically represented in Figure 2.8 for a thin SiO_2 layer on Si. It can be seen from the diagram that electrons emerging perpendicular to the surface have the same

sampling depth as those emerging at the angle θ, however, the perpendicular depth d' into the sample is considerably less than d. As such, the core level spectra taken at angle θ are more surface sensitive than those taken at normal emission. This is further evidenced by the Si 2p spectra in Figure 2.8 which are taken from a SiO_2 surface (5.4 nm) at emission angles equal to 0° (normal emission) and 60°. It can be clearly seen that the spectrum taken at 60° shows an increased intensity from the Si oxide overlayer.

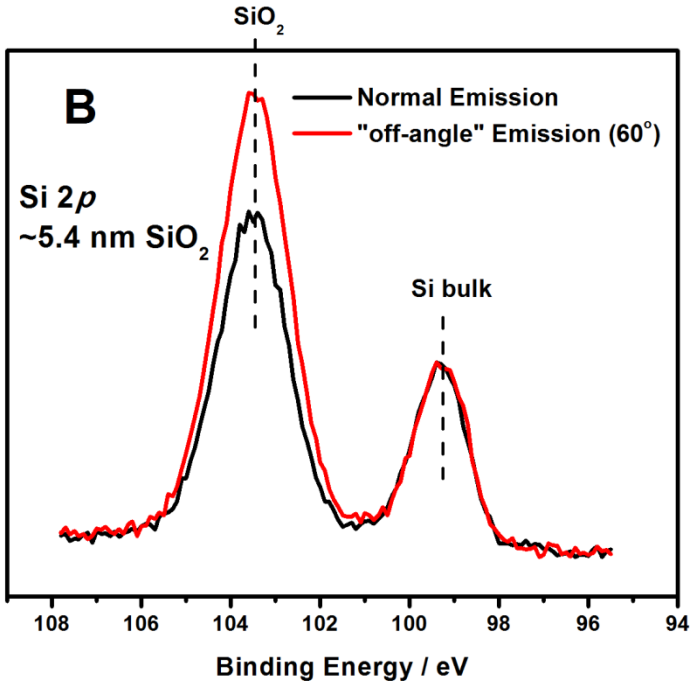

Figure 2.8 Si 2p spectra taken from a 5.4 nm SiO_2 layer on silicon showing increased surface sensitivity using ARXPS.

2.2 Transmission Electron Microscopy

Transmission electron microscopy (TEM) is a microscopy technique whereby a beam of high-energy electrons is transmitted through an ultra-thin specimen. An image is formed from the interaction of the electrons with the sample which is magnified and focused onto an imaging device such as a CCD camera. The focusing optics in a TEM system is similar to that of an optical instrument as shown in Figure 2.9.

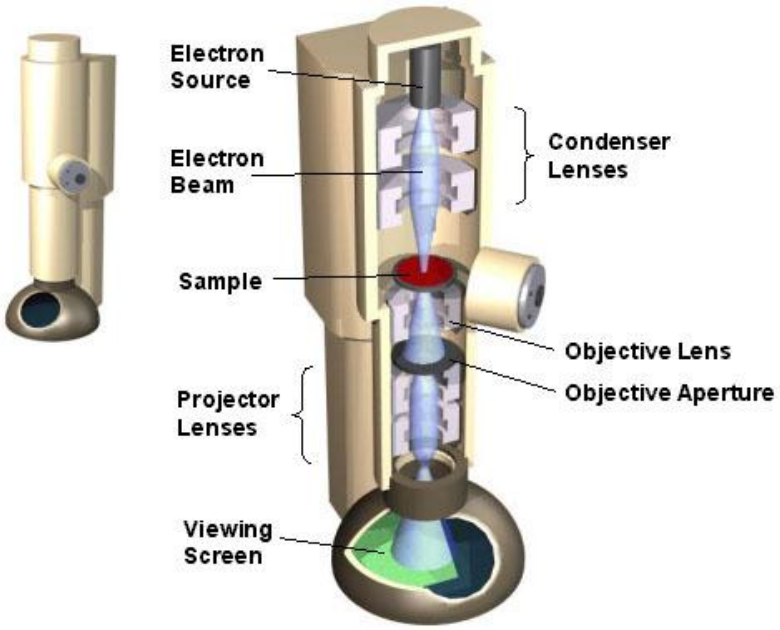

Figure 2.9 Schematic of TEM.[14]

Electrons are emitted from either a tungsten filament, or field emission gun and accelerated using high voltage (typically 80 kV – 200 kV) down the beam column, where the condenser lenses converge the electrons onto the

specimen and control beam intensity and density. After the interaction with the sample the electrons pass through the objective lens, which focuses the image. The intermediate lens is used to change between imaging modes and the projector lens provides final magnification before the electrons are detected by the combination of a fluorescent screen, photographic film and CCD camera. High vacuum is required within the system as the electron gun and all the electromagnetic lens focusing rely on a large mean free path.

Proper sample preparation is of vital importance to provide useful images. TEM samples are required to be at most hundreds of nanometers thick, as samples need to have thicknesses comparable to the mean free paths of the electron used. These thicknesses are achieved by a combination of mechanical grinding, ion milling and focused ion beam etching.

Two modes of operation can be selected depending on the configuration of the lenses. If the focusing is set similarly to an optical microscope to form an image of the sample, the microscope is said to be in contrast mode. Image contrast in TEM images can be obtained based on both the particle and wave properties of the electron. Electrons passing atoms of higher atomic number or thicker regions within the sample may not reach the detector due to absorption events. This will result in dark regions within the TEM image, allowing investigation of the structure and atomic composition of the sample. Within this mode images may be formed from the primary

undeviated beam (bright-field) or from a diffracted beam satisfying the Bragg condition (dark-field).

The second mode of operation is achieved by using the sample as a diffraction grating focussing the beam to form a diffraction pattern. This is known as diffraction contrast, which uses the Bragg scattering of electrons from crystalline regions within the sample. Scattering changes the angular distribution of the electrons, allowing them to be detected separately from unscattered electrons. As such, crystalline regions may be identified as bright regions within the image[15] and can be used to provide information regarding crystal structure, lattice parameter and structural defects.

2.3 Energy dispersive x-ray spectroscopy

Energy dispersive x-ray spectroscopy (EDX) is a complementary analysis technique which can be incorporated into a TEM. Essentially it can be seen as a close relative of Auger spectroscopy in that the incident TEM electron beam may excite an electron in an inner shell, ejecting it from the shell creating an electron hole as schematically illustrated in Figure 2.10. An electron from an outer, higher-energy shell then fills the hole, and the difference in energy between the high energy shell and the lower energy shell may be released in the form of an X-ray. The energy of each X-ray photon is characteristic of the element which produced it. The EDX system collects the X-rays and plots them as a function of energy, and automatically

identifies and labels the elements responsible for the peaks in the energy distribution. The EDX data are typically compared with either known or computer generated standards to produce a full quantitative analysis showing the sample composition.

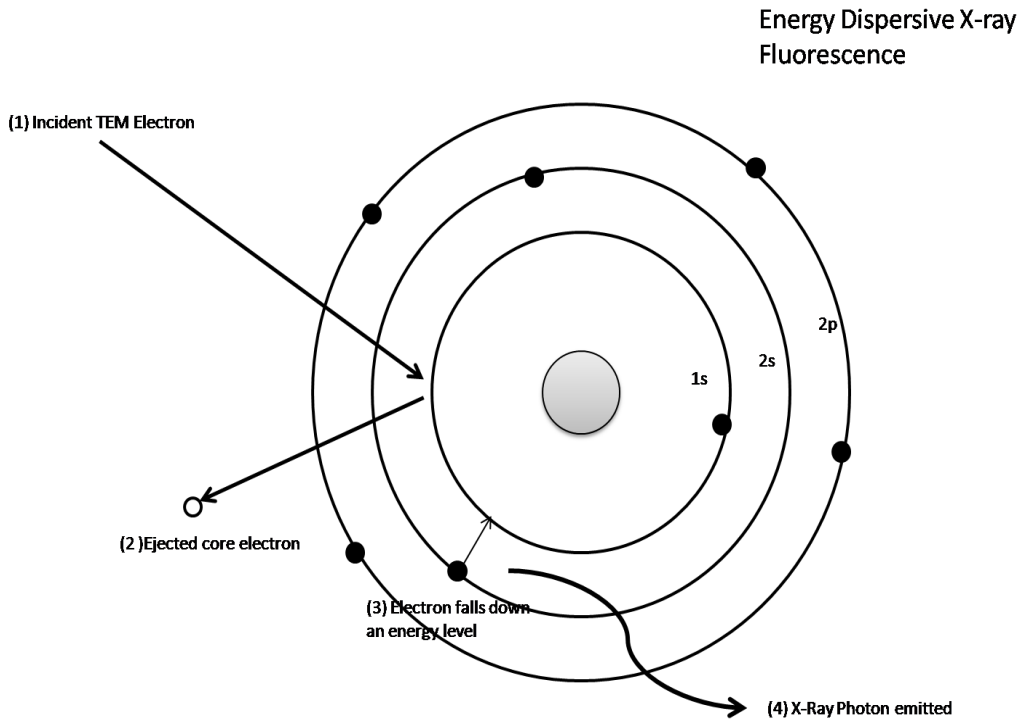

Figure 2.10 Basic concept of EDX.[16]

2.4 Electron energy loss spectroscopy

Electron energy loss spectroscopy (EELS) is a further useful technique which can be integrated into TEM. After interaction with the sample, some of the incident beam electrons will have lost a certain amount of energy due to inelastic interactions with the sample. These inelastic events include

phonon vibrations, plasmon excitations and inner shell ionizations. EELS is similar to EDX in that it also provides information on atomic composition and chemical bonding. However, unlike EDX, EELS works well at low atomic numbers and provides better spatial resolution when compared with EDX. The amount of energy loss is measured with an electron spectrometer similar to the energy analyser used in XPS and a plot of energy loss vs. relative intensity is plotted as shown in Figure 2.11.

The zero loss peak consists of elastic forward-scattered electrons which have lost no energy. The plasmon resonance peak is due to the collective response to the electron beam by all valence electrons. The ratio of plasmon peak intensity to zero-loss peak intensity may estimate the sample thickness. Of most interest is the region of high energy loss which contains core loss peaks. The peaks in this region are characteristic for each element and can provide chemical information. The fine structure of the peaks also contains information about the electronic structure (e.g. O peak in MnO is different than in NiO).

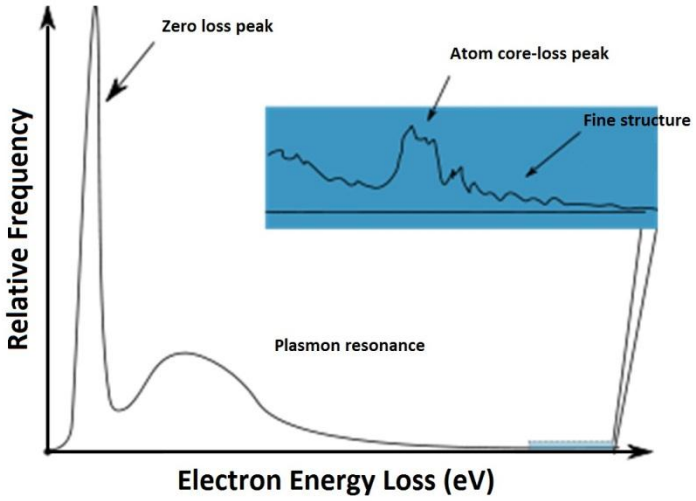

Figure 2.11 Typical EELS spectrum showing low loss and core loss regions.[16]

2.5 Atomic force microscopy

Atomic force microscopy (AFM) is an imaging technique used to obtain topographical information from the surface of a sample at near atomic resolution.[17] The ability of AFM to probe surfaces that are not conducting in nature gives it a distinct advantage over other similar and more sensitive techniques such as scanning tunnelling microscopy (STM). Another benefit of AFM is that it does not require an evacuated environment in which to operate, making it an extremely quick and accessible technique. The operation of AFM involves bringing an atomically sharp tip within close proximity of a surface and measuring the force that the tip experiences as it scans across a defined area. The tip is attached to the end of a cantilever. The basis of operation emerged from the discovery that inter-atomic forces

exist between two materials that are in close proximity of each other. Such forces can include Van der Waals, electrostatic or magnetic, the magnitude of which the AFM is designed to determine.[18]

The AFM can be operated in three modes: tapping mode, contact mode and non-contact mode. In contact mode the tip is scanned across a surface and any deflection in the cantilever is recorded. The force, and hence cantilever deflection, can be described by Hookes law; $F = - kx$ where k is the spring constant of the cantilever and x is the deflection.

In preparation for AFM operation, the tip must be appropriately positioned and engaged. This is accomplished by initially manoeuvring the tip to within approximately 1 mm of the surface using an optical microscope. The microscope is set up to focus on surface features at an image distance of 1 mm. Piezoelectric motors are then used reduce the tip-sample distance in increments of 10 μm until the tip is engaged. The imaging of the surface is then initiated by moving the sample in a scanning fashion underneath the tip.

The cantilever is deflected by inter-atomic forces as the sample surface is scanned with respect to the tip. The small deflections are detected using laser light which is reflected from the back of the cantilever and onto a split

photodetector, as illustrated in Figure 2.12. An image of the surface topology is generated from the movement in the deflected tip as detected by the photodetector.

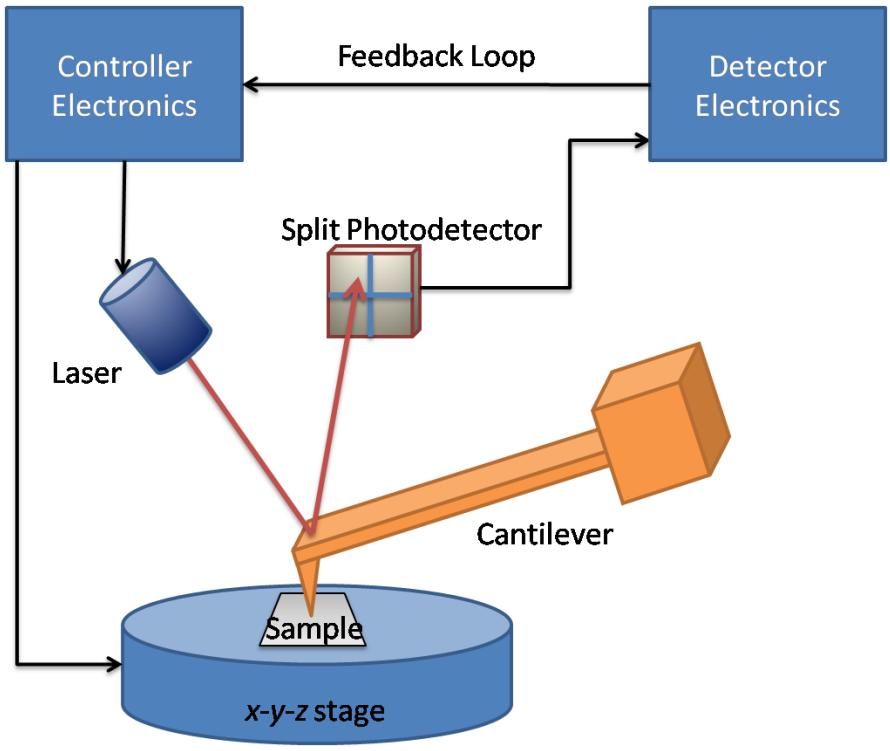

Figure 2.12 Operational diagram for AFM which shows how tip deflections are measured using laser light reflected from the back surface of the tip.[16, 18]

Tapping mode operation involves scanning the tip and 'tapping' the surface in the process. The tip is attached to the end of an oscillating cantilever, the frequency of which is kept constant by altering the position of the tip relative to the surface. The amplitude of the oscillating cantilever is typically between 20 nm and 100 nm, which is engineered to operate at or near its resonance frequency.[18] In tapping mode the tip spends much less

time 'in contact' with the surface resulting in less damage due to surface contamination. Finally, in non-contact mode, the tip does not come in contact with the surface at all. This is achieved by oscillating the cantilever above the surface, usually at tip-sample distances of between 1 nm and 10 nm. This mode is typically used in soft biological samples to prevent both sample and tip damage.

A Dimension 3100 SPM atomic force microscope was used in this study which included an acoustic and vibration isolation hood on an anti-vibration table. All images presented in this study were acquired using the AFM in tapping mode. Information such as surface roughness, feature height and root mean square (RMS) surface roughness were extracted using free software called WSxM.[19] A minimum of 8 sites across the sample surface were used to calculate RMS surface roughness values.

2.6 Secondary ion mass spectroscopy

Secondary ion mass spectroscopy (SIMS) is a highly sensitive technique used to analyse the composition of solid surfaces and thin films by sputtering the surface of a sample with a focused ion beam such as Ar^+. Secondary ions are ejected from the target as a result of the sputtering process which can then be collected and analysed using a mass spectrometer. SIMS is considered to be the most sensitive analysis

technique, with elemental detection limits in the region of parts per million. The SIMS data acquired in this report was recorded on an IONTOF, TOF SIMS 300 in Intel's Laboratory in Leixlip, Co. Kildare.

References

[1] D.P. Woodruff, T.A. Delchar, modern techniques of surface science, Cambridge Solid State Series (1986)

[2] Fundamentals of Nanoscale Film Analysis, Springer US ISBN 978-0-387-29260-1(Print) 978-0-387-29261-8 (Online)

[3] L.C. Feldman, J.W. Mayer, Fundementals of surface and thin film analysis, Elsevier Science Publishing Co., Inc (1986)

[4] G. Somerjai, Chemistry in Two Dimensions: Surfaces (Cornell University Press, Ithaca, NY, 1981)

[5] G. Alvarez, H.J. Silverstone, Phys. Rev. A, **40,** 3690 (1989)

[6] C.D. Wagner, L.E. Davis, M.V. Zeller, J.A Taylor, R.M. Raymond and L.H. Gale, Surf. Interface Anal. **3,** 211 (1981)

[7] M.P. Seah and S.J. Spencer, Surf. Interface Anal. **33,** 640 (2002)

[8] D. Briggs, M.P. Seah, Practical Surface Analysis: Volume 1, Auger and X-ray Photoelectron Spectroscopy, Wiley, Chichester, 1990

[9] R.G. Vitchev, J.J. Pireaux, T. Conard, H. Bender, J. Wolstenholme, Chr. Defranoux, Appl. Surf. Sci. **235,** 21-25 (2004)

[10] A. Jablonski, C.J. Powell, Surface Science Reports **47,** 33 (2002)

[11] F.J. Himpsel, F.R. McFreely, A. Taleb-Ibrahimi, J.A. Yarmoff and G. Hollinger, Phys. Rev. B **38,** 6084 (1988)

[12] R.G Vitchev, Chr.Defranoux, J. Wolstenholme, T. Conard, H. Bender, J.J. Pireaux, Journal of Electron Spectroscopy and Related Phenomena **149,** 37-44 (2005)

[13] C.J. Powell, A. Jablonski, W.S.M Werner, W. Smekal. Appl. Surf. Sci., **239,** 470 (2005)

[14]http://barrett-group.mcgill.ca/tutorials/nanotechnology/nano02.htm

[15] D.B. Williams and C.B. Carter, Transmission Electron Microsscopy Volume 1. Plenum Publishing Corporation.

[16] Growth and chemical characterisation studies of Mn silicate barrier layers on SiO_2 and CDO, Ph.d. thesis (2011), Justin Bogan, Dublin City University.

[17] J.C. Vickerman, Surface Analysis: The Principle Techniques, J.C. Vickerman, Ed. Wiley, 1997.

[18] V.M.G Digital Instruments, Nanoscope scanning probe microscope training manual 1999.

[19] I. Horcas et. al. Rev. Sci. Instrum, **78**, 013705 (2007)

Chapter 3

Chemical and structural investigations of the incorporation of metallic and partially oxidised Mn into Ru thin films for use as Cu diffusion barrier layers

3.1 Introduction

As stated in Chapter 1, the concept of 'stuffing' the grain boundaries of Ru thin films has been proposed as a potential mechanism to improve the Cu diffusion barrier properties of Ru liner layers. Given that Mn has been shown to form effective Cu diffusion barrier layers on SiO_2 surfaces,[1,2] it is suggested that it may be a suitable candidate for 'stuffing' the grain boundaries of Ru films.[3] Therefore the focus of this chapter is to investigate the chemical interactions of deposited Mn on 3 nm ALD Ru thin films. The stated film thickness of 3 nm was confirmed by TEM data which will be shown in section 3.3. It will also be shown in section 3.3 that the thermal annealing of ~1 nm of e-beam deposited metal Mn on a 3 nm Ru film results in the diffusion of Mn through the Ru liner and the subsequent interaction of Mn with the underlying SiO_2 dielectric substrate. A consequence of the chemical interaction of Mn with SiO_2 in the presence of a Ru thin film, is

the release of Si from the substrate, which will be investigated further in section 3.4.

3.2 Experimental details

The X-ray photoelectron spectroscopy (XPS) analysis was carried out using a VG Microtech electron spectrometer at a base pressure of ~1×10^{-9} mbar. The photoelectrons were excited with a conventional Mg Kα ($h\nu$ = 1253.6 eV) x-ray source and an electron energy analyser operating at a 20 eV pass energy, yielding an overall energy resolution of 1.2 eV. There was also an Al anode available however the Mg source was used for superior resolution. A thermal annealing study up to 500 ^{o}C was carried out in vacuum at a pressure of ~5×10^{-9} mbar, with samples kept at the target temperature for 60 minutes. Hydrochloric acid (HCl) etched Mn chips, with a purity of ~99.9 %, were used as a source material for the deposition of metallic Mn thin films, using an Oxford Applied Research EGC04 mini electron-beam evaporator, at a chamber pressure of ~5×10^{-9} mbar. The XPS core level spectra were curve fitted using Voigt profiles composed of Gaussian and Lorentzian line shapes in a 3:1 ratio with a Shirley-type background. The FWHM of the Si 2p bulk peak was 0.9 eV, with SiO_2 and Mn silicate component peaks in the range 2.0 eV to 2.1 eV. The FWHM of the O 1s SiO_2 component was 1.2 eV with Mn-silicate and Mn-oxide peaks in the range of 1.1 eV to 1.2 eV. It should be noted that curve fitting of the Mn 2p

spectrum could not be performed given that XPS ghost peaks[4] emanating from the Mn $2p_{1/2}$ are present within the peak profile of the Mn $2p_{3/2}$ component. The spin orbit splitting of the Mn 2p peak is ~ 11 eV, and the $K\alpha_3$ and $K\alpha_4$ x-ray emission lines are seperated from the main $K\alpha_{1,2}$ peak by 8.5 eV and 10.1 eV respectively. The combined relative intensity of the $K\alpha_{3,4}$ peak compared to that of $K\alpha_{1,2}$ is ~14.2%.[4] As such, only non-curve fitted Mn 2p spectra are included in this chapter. In agreement with previous works[5,6] the Mn 2p spectra shown in this study are primarily used to identify the presence of metallic Mn and oxidized Mn species on the sample surface, with O 1s and Si 2p spectra used to identify the presence of differing oxidized Mn species such as Mn-silicate and Mn-oxide. High resolution transmission electron microscopy (HRTEM) and electron energy-loss spectroscopy (EELS) in scanning-TEM (STEM) mode were carried out in a JEOL 3000 FEGTEM operating at 300 kV with a nominal probe size below 1 nm in the Materials Department in Oxford University. TEM and Energy-dispersive X-ray spectroscopy (EDX) measurements were made on a Tecnai G20 – LaB_6 200 KV with an EDAX system. Secondary ion mass spectroscopy (SIMS) data was recorded on an IONTOF, TOF SIMS 300 in the Intel Laboratory in Leixlip, Co Kildare.

3.3 The diffusion of Mn through Ru thin films and the subsequent formation of Mn-silicate at the underlying dielectric

Prior to XPS analysis the as received 3 nm ALD Ru film was analysed using atomic force microscopy (AFM) and scanning electron microscopy (SEM). AFM and SEM analysis indicated that the Ru film was flat and continuous with an average RMS surface roughness measurement of ~0.2 nm. Following the completion of AFM and SEM analysis, the Ru sample was then loaded into the UHV system and analysed using XPS. The O 1s and Ru 3d spectra taken from the as-received surface showed the presence of a surface localized Ru oxide species related to air exposure. A degassing procedure of thermal annealing at 300 °C for 4 hours was then performed on the surface, with O 1s and Si 2p spectra taken following degassing shown in Figure 3.1. The O 1s spectrum taken from the degassed surface shows a single component peak attributed to oxygen in the SiO_2 substrate, with no evidence for the presence of Ru oxide to within the detection limit of conventional XPS.

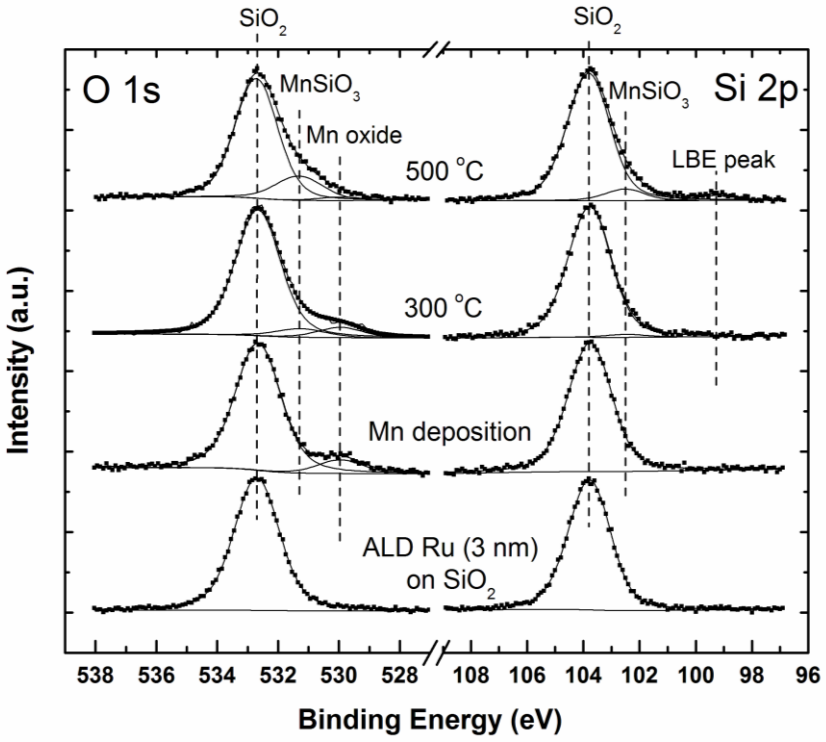

Figure 3.1 O 1s and Si 2p spectra showing the growth of $MnSiO_3$ as a function of thermal anneal. (BE positions in O 1s - SiO_2 = 532.7 eV, $MnSiO_3$ = 531.3 eV, Mn-oxide = 530 eV : BE positions in Si 2p – SiO_2 = 103.8 eV, $MnSiO_3$ = 102.5 eV). All peak fitting parameters included in Appendix A.

Approximately ~1 nm of metal Mn was deposited by in-situ e-beam evaporation on the 3 nm Ru film and the sample was subsequently thermally annealed up to 500 ^{o}C in a UHV environment of base partial pressure ~$1x10^{-9}$ mbar and the associated XPS core spectra are shown in Figure 3.1. A small amount of Mn oxide was detected after the Mn deposition which was attributed to the presence of residual gaseous oxygen in the UHV chamber. It has been reported that Mn readily oxidises with oxygen

exposures as low as 10 Langmuirs.[7] During the annealing cycle, there is evidence for the growth of an additional component peak on the lower binding energy side of both the O 1s and Si 2p spectra. The relative binding energy positions of both these additional peaks are identical to those attributed to $MnSiO_3$ in a similar study involving the thermal annealing of metal Mn on SiO_2[1,5] in the absence of Ru. It is important to note that $MnSiO_3$ has been reported to be an effective barrier to Cu diffusion[2] and as such the formation of $MnSiO_3$ seen in this study may improve the diffusion barrier properties of the Ru/Mn layer. Figure 3.2 shows the growth of an additional peak on the higher binding energy side of the Mn 2p spectra, labelled 'oxidized Mn', which is in agreement with the formation of a species involving Mn. This component peak overlaps with a ghost peak associated with the higher binding energy metal Mn peak, making it very difficult to curve fit. As a result, it is very difficult to distinguish between Mn that is in an oxidized state and Mn that is in a silicate state. However, O 1s spectra show no evidence for the growth of a Mn-oxide component peak, which is known to form between ~529.0 eV & 530.0 eV.[1,5,8] Furthermore, the concurrent growth of component peaks in the O 1s, Si 2p and Mn 2p core levels, suggests the formation of a chemical species containing all three elements. The formation of $MnSiO_3$ implies the diffusion of Mn through the 3 nm Ru film to the SiO_2/Ru interface, where the chemical interaction occurs. Additionally, there was a noticeable reduction in the relative

intensity of the Mn 2p signal with respect to the Ru 3d as a function of annealing which is consistent with the diffusion of Mn into the Ru film. It should again be noted (P 45) that AFM and SEM measurements suggest that the 3 nm Ru film was continuous on the SiO_2 surface. Therefore, it is suggested that the $MnSiO_3$ growth is due to the diffusion of Mn through the Ru film, and not due to the interaction of Mn with "uncovered" areas of the SiO_2 substrate. The 3 nm ALD Ru film was also annealed in the absence of Mn where no noticeable changes in the Si 2p or Ru 3d were recorded.

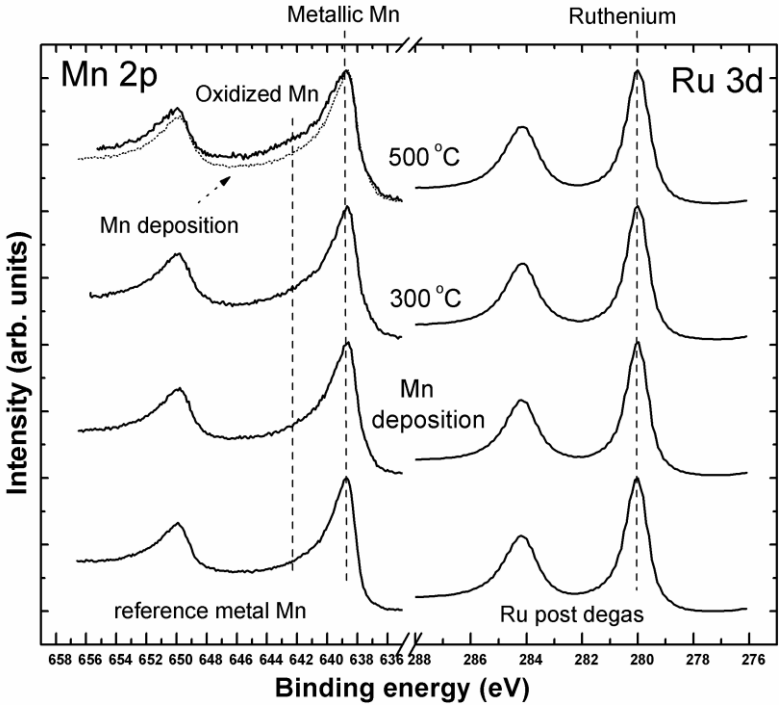

Figure 3.2 Mn 2p spectra showing the growth of a component peak referred to as 'oxidized Mn' as a function of thermal anneal. The Mn 2p 'Mn deposition' spectrum is also overlaid on the 500 ^{o}C spectrum for comparison. Ru 3d spectra (290 eV – 275 eV) show no change during the experiment. (BE positions in Mn 2p – Metallic Mn = 538.8 eV, Oxidized Mn =

642.4 eV: BE positions in Ru 3d = 280 eV). All peak fitting parameters included in Appendix A.

There is some evidence in Figure 3.1 for the growth of a peak on the lower binding energy (LBE) side of the Si 2p spectra at ~99.3 eV following higher annealing temperatures. No corresponding peak was reported by Casey et al[1] when Mn was deposited on SiO_2 in the absence of Ru, suggesting that the presence of the overlying Ru film may play a role in the appearance of this additional peak. The growth of a Ru-silicide species could not be ruled out as a potential explanation for this additional peak, and will be investigated further in section 4.5. However, in this study, the Ru 3d spectra in Figure 3.2 remained unchanged as a function of annealing and as such there is no evidence for the chemical interaction between the Ru and Si during the experiment. It is possible that the limited amount of free Si produced in this study is not sufficient to impact the Ru 3d peak emanating from the dominating and abundant Ru metal signal. Moreover, there is no evidence for any chemical interaction of Ru with the underlying SiO_2 substrate, which has been confirmed by a parallel control experiment involving the thermal annealing of the 3nm ALD Ru film in the absence of Mn up to 500 ^{o}C. However, given that the samples were received with the Ru layer already deposited, any potential chemical interaction of the deposited Ru with the substrate could not be determined. Another potential explanation for the additional Si peak is the growth of Mn-silicide species.

Casey et al[1] have previously observed the formation of extremely low levels of Mn-silicide growth following the interaction of Mn with SiO_2. However, the binding energy position of this Mn-silicide peak does not coincide with the LBE peak seen in this experiment. Whatever the species of the peak at ~99 eV, it appears to be related to the presence of residual Si resulting from the conversion of SiO_2 into $MnSiO_3$ at the Ru/SiO_2 interface. One possible explanation for this peak is that it is related to the presence of residual silicon which has diffused up from the Ru/SiO_2 interface following the conversion of SiO_2 into $MnSiO_3$ at the Ru/SiO_2interface, however, this has not been conclusively shown in this section.

Figure 3.3 shows a high resolution transmission electron microscopy (TEM) image of the Ru layer which had been annealed to 500 ^{o}C, where grains of differing orientations can be seen indicating its polycrystalline structure. It should be noted that it was not possible to accurately calibrate the thickness of the Ru layer as the bulk Si lattice was not present within the TEM image, however, the measurements suggest that it is close to the target 3 nm thickness and displays good uniformity.

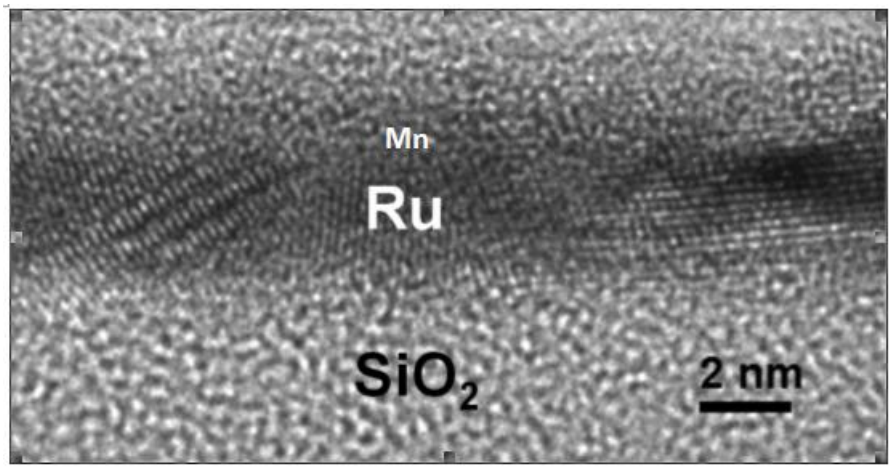

Figure 3.3 High resolution TEM image of the interfacial Ru layer displaying its polycrystalline structure.

Figure 3.4(a) shows a high-angle annular dark field (HAADF) STEM image of the structure. Given that this technique is sensitive to the atomic number of the different elements or species present in the sample, the Ru layer appears brighter. There is no indication of Ru or Mn diffusion into the underlying dielectric. There is no visual evidence for a second layer at the Ru/SiO_2 interface which could be attributed to that of $MnSiO_3$ in either the HRTEM or the HAADF-STEM micrographs. However, the intensity profile of the Mn_L edge extracted signal obtained from the EELS line scan across the Ru layer shown in Figure 3.4(b) indicate that the Mn is non-uniformly distributed. There appears to be a build-up of Mn at both the Ru surface and the Ru/SiO_2 interface with reduced intensity within the Ru film itself. It is worth noting that the uniformity of the Mn signal intensity along the Ru/SiO_2 interface is not constant, some areas being almost void of any Mn

signal, which may be evidence for the localized diffusion or ‘stuffing’ of Mn in the grain boundaries of the Ru film.

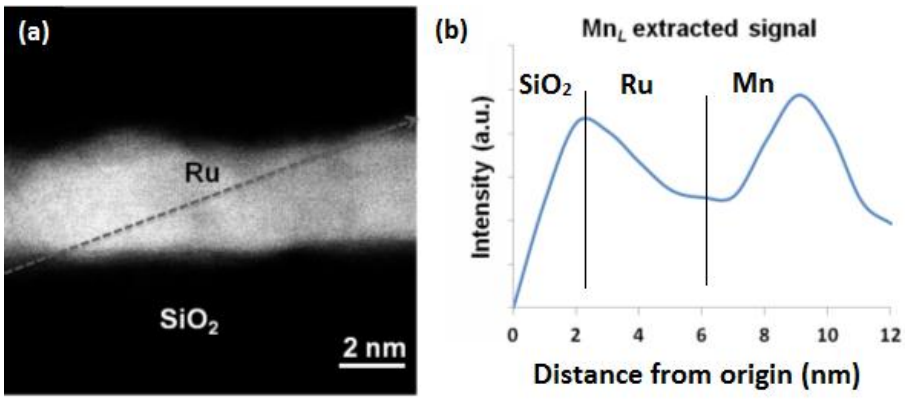

Figure 3.4(a) STEM-HAADF micrograph of the Mn-Ru/SiO_2 layers. **(b)** Mn composition profile obtained from the EELS line profile indicated by the dashed line in (a), showing the presence of Mn at the Ru / SiO_2 interface, and at the Ru surface. There is a much reduced Mn signal intensity in the Ru film itself suggesting that the Mn migrated through the film where it interacted with the SiO_2 substrate.

3.4 Investigation of the release of Si from SiO_2 during the formation of Mn/Ru barrier layers

It has been shown in section 3.3 that the deposition of metal Mn on Ru thin films results in the diffusion of Mn through the film and the subsequent formation of Mn-silicate at the Ru/SiO_2 interface.[9] However, the presence of an additional Si peak, as observed by the emergence of an XPS component on the lower binding energy (LBE) side of the Si 2p spectrum, at a BE position of ~99 eV, remained largely unaccounted for. Importantly, it has been reported by Frederick et. Al[10] and Wu et. Al[11] that the upward diffusion of un-bonded Si from the dielectric substrate during barrier layer growth leads to an increase in interconnect line resistance and degradation of device performance. It is therefore essential that the mobility and location of the Si reported in section 3.3[9], is studied in further detail in order to understand its origins and its impact on barrier formation. The focus of this section is to determine the chemical state of this Si species and investigate whether it remains confined within the barrier layer region or, conversely, if it has diffused away from the interface towards the Cu interconnect. The growth characteristics of Mn-silicate barriers layers on SiO_2 surfaces in the absence of Ru have previously been investigated in some detail using XPS. Casey et al[5] have shown that the growth of Mn-silicate can be enhanced by the deposition of partially oxidized Mn, however, no evidence for a similar LBE Si 2p component peak was reported in that study. Therefore, in this

section, a partially oxidized Mn film was deposited onto the Ru/SiO_2 surface in order to investigate whether the presence of additional oxygen promotes the growth of Mn silicate at the Ru/SiO_2 interface and to determine if this results in a concurrent increase in the growth of the Si peak identified in section 3.3.[5]

A thin (~2 nm) Mn-MnO_x film was deposited onto the 3 nm Ru surface. The Mn 2p spectrum taken from the Mn film following deposition is shown in Figure 3.6. This spectrum shows evidence for both metallic Mn and oxidized Mn, which is consistent with the emergence of a Mn oxide component peak at 530 eV within the O 1s spectrum in Figure 3.5. This is in agreement with the work of Lescop et. al.[7] who have shown that Mn-oxide formation can occur following oxygen exposure as low as 10 Langmuirs. The oxygen exposure during deposition of the Mn film in this experiment was ~ 30 Langmuirs. The sample was subsequently annealed up to 500 ^oC in UHV at a base pressure of ~$1x10^{-9}$ mbar and the associated XPS core level spectra were recorded. Figure 3.5 shows a reduction in the O 1s Mn-oxide component peak[9] following thermal annealing along with a corresponding growth of an additional component at a binding energy position of 531.3 eV. This is accompanied by the appearance of an additional peak in the Si 2p spectrum, at a binding energy separation of 1.4 eV from the SiO_2 bulk

peak, consistent with the conversion of Mn and Mn-oxide into Mn-silicate in agreement with previous studies and section 3.3.[5,6]

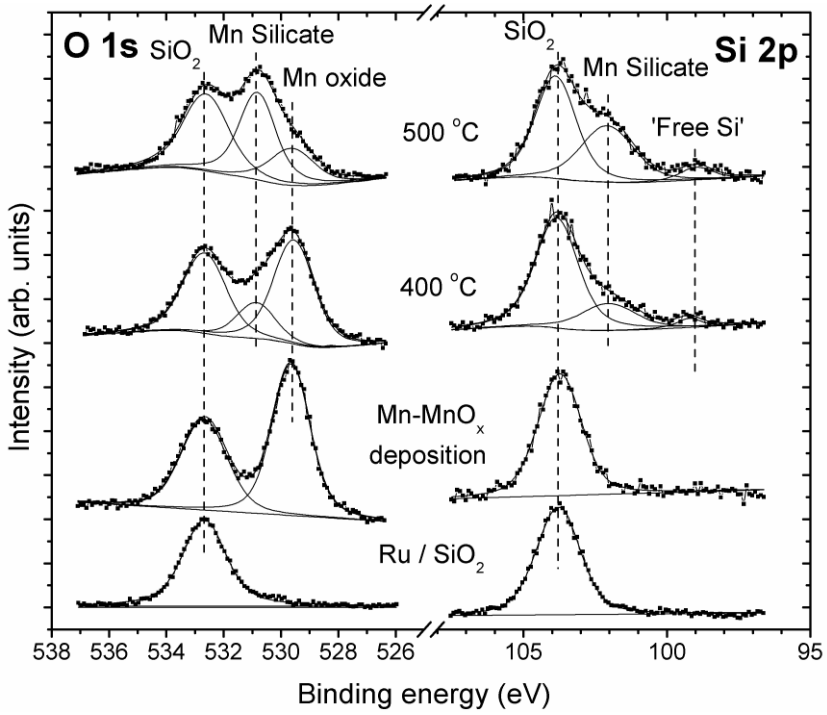

Figure 3.5 O 1s and Si 2p spectra taken from the Ru/SiO_2 surface following $Mn\text{-}MnO_x$ deposition and subsequent UHV thermal annealing treatments**.** (BE positions in O 1s - SiO_2 = 532.7 eV, $MnSiO_3$ = 531.3 eV, Mn-oxide = 530 eV : BE positions in Si 2p – SiO_2 = 103.8 eV, $MnSiO_3$ = 102.5 eV). All peak fitting parameters included in Appendix A.

In section 3.3 of this chapter the formation of Mn-silicate at the Ru/SiO_2 interface following the diffusion of metallic Mn through the Ru grain structure was investigated. However, two aspects of the results shown in Figure 3.5 cannot be fully explained based on the information currently available within the literature. Firstly, the results show evidence for

considerably higher levels of Mn silicate growth than previously reported following the metallic Mn deposition.[9] Casey et al[5] have previously shown that the formation of Mn silicate is self-limited by the presence of additional oxygen species beyond that present within the SiO_2 film and as such increased silicate formation following the deposition of partially oxidized Mn is in agreement with expected results. However, the mechanism of Mn silicate growth in the $MnO_x/Ru/SiO_2$ system requires further analysis. Secondly, Si 2p spectra in Figure 3.5 show the emergence of a component peak at BE position of ~99 eV following thermal annealing, in agreement with the results in section 3.3 of this when metallic Mn was deposited.[9] This peak is attributed to the presence of released Si. Cerofolini et al.[12] reported the binding energy positions of the Si $2p_{1/2}$ and $2p_{3/2}$ lines for various species of Si-Si and Si-H bonds. Therefore, it is important to determine if the increased levels of Mn silicate formation seen in Figure 3.5 are due to the diffusion of both Mn and oxygen through the Ru film, or alternatively, if the Mn silicate growth is increased due to the upward diffusion of Si allowing it to react with the deposited MnO_x layer. Ru 3d spectra acquired following MnO_x deposition and subsequent thermal annealing are shown in Figure 3.6. It can be seen that there is no noticeable change in the profile of the Ru 3d peaks during the course of the experiment and therefore it can be stated that the chemical state of the Ru layer was not altered to within the detection limit of XPS.

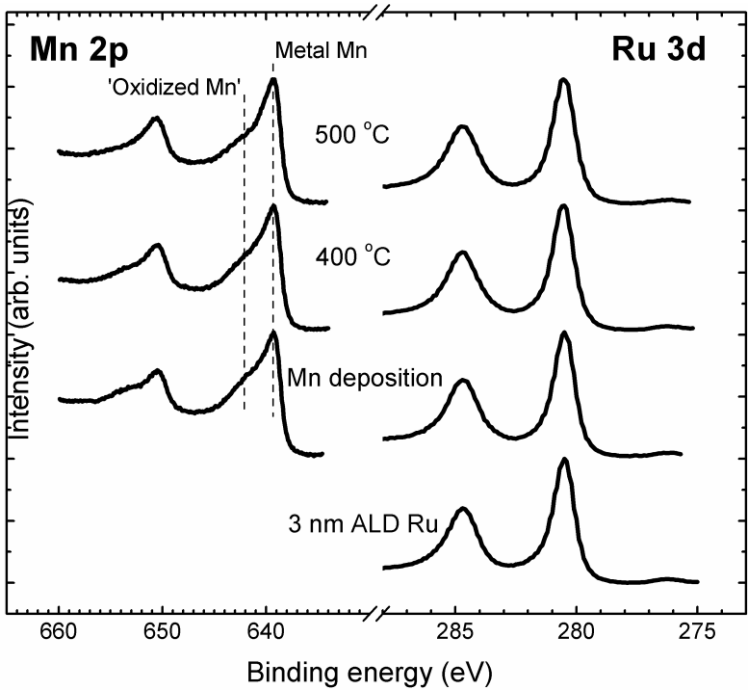

Figure 3.6 Mn 2p and Ru 3d spectra corresponding to Figure 3.5. Mn 2p spectra showing no significant change after thermal anneal due to the conversion of Mn oxide to Mn-silicate, both of which have similar BE positions. Ru 3d spectra (290 eV – 275 eV) show no change in profile during the experiment. (BE positions in Mn 2p – Metallic Mn = 538.8 eV, Oxidized Mn = 642.4 eV: BE positions in Ru 3d = 280 eV). All peak fitting parameters included in Appendix A.

Figure 3.7(a) shows TEM analysis of the Mn-MnO_x/Ru system, together with a copper capping layer deposited prior to removal from the UHV system in order to prevent atmospheric contamination. The Ru layer can be clearly identified with a measured thickness of ~3.6 nm while the deposited Mn-MnO_x layer has a thickness of ~2.8 nm. EDX analysis was then performed in order to determine the relative position of the released Si species within the Mn/Ru/SiO_2 structure and these results are shown in

Figure 3.7(b). This analysis shows evidence for the presence of both Si and Mn within the Ru layer, which is consistent with the upward diffusion of Si released from the substrate during the formation of Mn-silicate at the Ru/SiO_2 interface. This analysis is in agreement with the appearance of the LBE Si 2p peak shown in Figure 3.5 and that reported in section 3.3. While EDX analysis offers strong evidence for Si diffusion, it is not conclusive, as the spatial resolution of the technique may not be sufficient to adequately analyze the chemical composition of the ultra-thin 3.6 nm Ru film. Consequently, SIMS analysis of the same sample was performed in order to provide more conclusive evidence of silicon diffusion.

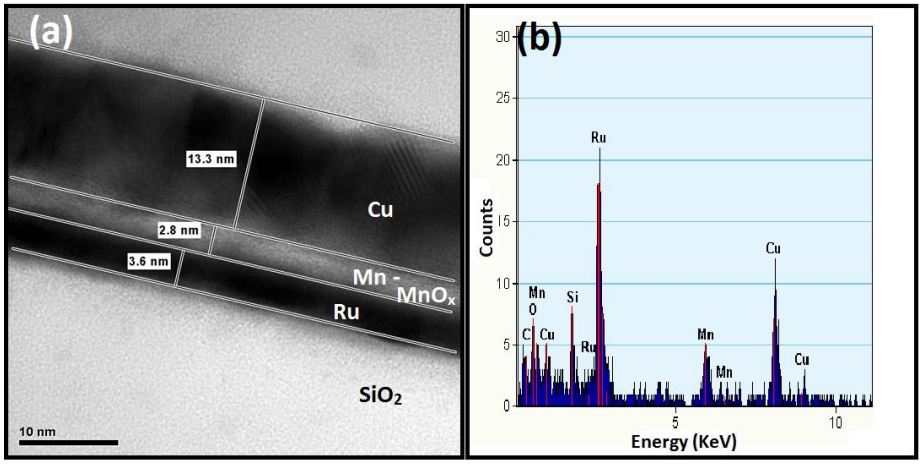

Figure 3.7(a) High resolution TEM image of the interfacial Ru layer and overlying Mn-MnO_xlayer on the SiO_2 substrate with the protective Cu capping layer. **(b)** Corresponding EDX analysis showing the presence of a Si signal in the Ru layer.

The SIMS profile, shown in Figure 3.8 clearly displays evidence of a Si signal within the Ru film. Furthermore, the presence of Si within the overlying Mn/Mn-oxide deposited layer is further apparent. Both of these experimental observations suggest that some of the Si released from the SiO_2 dielectric substrate following the interaction with Mn has diffused through the Ru film to the surface of the ALD deposited layer. It should be noted that a control sample (not shown) consisting of the same Ru ALD layer on SiO_2 without the presence of Mn was annealed to 500 ^oC and no Si signal was observed in or above the Ru layer in the SIMS profile. The presence of Si in the Mn-MnO_x deposited layer suggests that the significantly increased silicate growth seen in the Si 2p and O 1s XPS spectra in this study results from Mn–silicate forming either in or on top of the Ru film, as well as at the SiO_2/Ru interface. It should be noted that previous studies investigating the growth of Mn silicate barrier layers on SiO_2 surfaces in the absence of Ru showed no evidence for the release of Si.[1] As such, the mechanism by which Si is released from the Mn/Ru/SiO_2 interface is not clear. It should be noted that there is a small error 'blip' present in the SIMS profile at ~280 seconds.

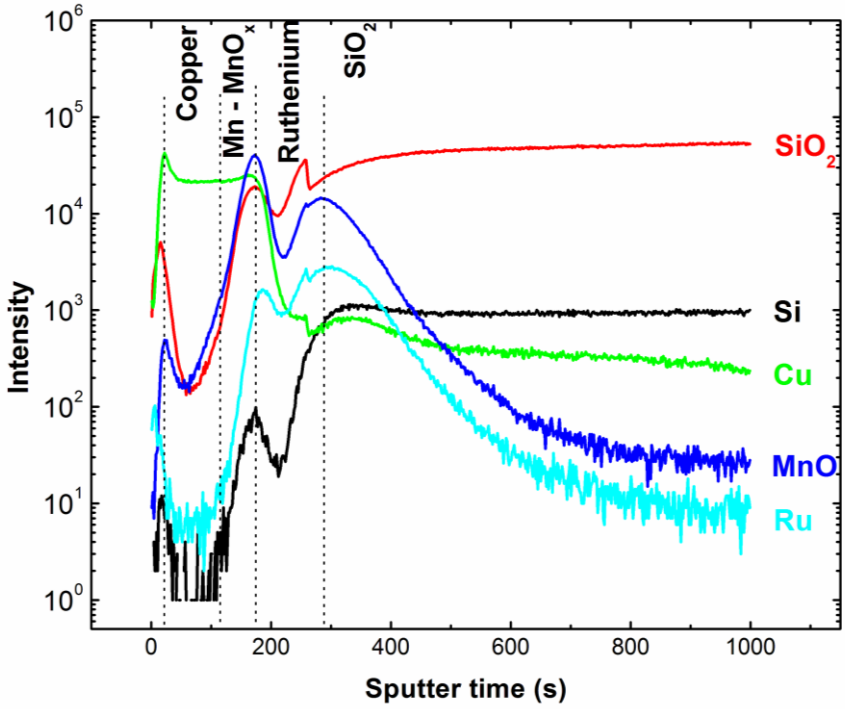

Figure 3.8 SIMS analysis taken from the Mn-MnO_x/Ru/SiO_2 structure following the completion of XPS analysis. SIMS profile shows the presence of a Si signal at the surface of the Ru film indicating the upward diffusion following Mn-silicate growth at the Ru/SiO_2 interface.

These results therefore suggest a possible reaction mechanism for the appearance of increased Mn-silicate formation when the Mn overlayer is partially oxidised. When metal Mn is deposited on a Ru thin film in UHV, Si is released from the substrate upon silicate formation at the Ru/SiO_2 interface. However, in the case of a metallic Mn deposition, the extent of Mn-silicate growth is self-limited by the absence of oxygen as a chemical

reactant to form more Mn–silicate with the released Si in the Ru film. As shown here, the presence of partially oxidized Mn on the Ru surface provides a source of oxygen to facilitate further silicate growth. Therefore, it cannot be assumed that an increased silicate signal is related to the barrier layer formation beneath the Ru film. In follow up experiments the Mn-silicate signal was further increased by annealing the sample at 500 ^{o}C in an oxygen partial pressure of ~1x10^{-8} mbar, indicating the importance of the supply of additional oxygen as a reactant to facilitate further Mn-silicate growth. However, this additional silicate growth is at the surface of the Ru layer, rather than at the Ru/SiO_2 interface. Previous studies by Frederick et al.[10] and Wu et al.[7] have also reported the release of Si from the SiO_2 substrate during the formation of Cu diffusion barrier layers. These studies reported the diffusion of un-bonded Si into the Cu interconnect causing an increase in interconnect resistivity and degradation in device performance. As such, the release and upward diffusion of Si from the SiO_2 surface during $MnSiO_3$ growth may have a significant impact on the effectiveness of Mn/Ru based Cu diffusion barrier layers.

3.5 **Conclusions**

In summary, it has been shown that Mn can be diffused through a 3 nm ALD Ru thin film following thermal annealing at temperatures lower than 500 °C. It has also been shown using XPS analysis that diffused Mn interacts with the underlying SiO_2 dielectric substrate to form the Mn-silicate species $MnSiO_3$ which is known to be a barrier to Cu diffusion.[2] The EELS profile of the Mn elemental distribution across the Ru layer supports this finding, suggesting that Mn may be a suitable metal to 'stuff' the grain boundaries of Ru films thereby improving the integrity of the film as a barrier to Cu diffusion. It has also been shown that a thin deposited layer of partially oxidized Mn on a 3 nm ALD Ru film results in the diffusion of Mn through the Ru film and the subsequent formation of Mn-silicate at the Ru/SiO_2 interface upon anneal. EDX and SIMS analysis indicate that Si is released from the SiO_2 interface during the formation of interfacial silicate, and the free Si diffuses upward through the Ru film. XPS analysis indicates the growth of a substantial quantity of Mn-silicate formed at both the Ru / SiO_2 interface and within the Mn/MnO_x deposited layer as a result of this upward Si diffusion. These results have implications for the integration of Ru/Mn layers into future interconnects in that the release of silicon from the underlying dielectric layer as a result of silicate formation could have detrimental consequences in terms of subsequent copper plating and operational longevity.

3.6 References

[1]Patrick Casey, Justin Bogan, Barry Brennan, and Greg Hughes, Appl. Phys. Lett. **98**, 113508 (2011).

[2]J. Koike, M. Haneda, J. Iijima, Y. Otsuka, H. Sako, and K. Neishi, J. Appl. Phys. 102, 043527 (2007).

[3]H.Wojcik, R. Kaltofen, C. Krien, U. Merkel, C.Wenzel, J.W.Bartha, M. Friedemann, B. Adolphi, R.Liske, V. Neumann and M. Geidel, Interconnect Technology Conference and 2011 Materials for Advanced Metallization (IITC/MAM), 2011 IEEE International, pp.1-3, 8-12 (May 2011).

[4]M. O. Krause and J. G. Ferreira, J. Phys. B: At. Mol. Phys. **8**, 12 (1975).

[5]P. Casey, J. Bogan, J. G. Lozano, P. D. Nellist, and G. Hughes, J. Appl. Phys. **110**, 054507 (2011).

[6]P. Casey. J. Bogan, J. Lozano, P. Nellist, G. Hughes et al, J. Appl. Phys. **110,** 124512 (2011).

[7]B. Lescop, Appl. Surf. Sci. **252,** 2276–2280 (2006).

[8]A. A. Audi, P. M. A. Sherwood, Surf. Interface Anal. **33**, 274 (2002).

[9]A.P. McCoy, P. Casey, J. Bogan, J.G. Lozano, P.D. Nellist, and G. Hughes, Appl. Phys. Lett. **101**, 231603 (2012).

[10] M.J. Frederick, R. Goswami, and G. Ramanath, J. Appl. Phys. **93**, 5966 – 5972 (2003).

[11] Wen-Fa Wu, Kou-Chiang Tsai, Chuen-Guang Chao, Jen-Chung Chen, Keng-Liang Ou, J. Electron. Mater. **34**, 1150 – 1156 (2005).

[12] G. F. Cerofolini, C. Galati and L. Renna Surf. Interface Anal.; **35**, 068-973 (2003).

Chapter 4

The addition of Al to Ru liner layers for use as Cu diffusion barriers

4.1 Introduction

Aluminium has been investigated as a potential self-forming barrier layer material, mainly because it has been used for IC metallization in the past. Perng et. al.[1] showed that adding small amounts of Al to bulk Cu is an effective way to produce a self-forming AlO_x Cu diffusion layer on porous low-κ films. Given that aluminium segregates to the interfaces of copper films,[2] a focus of this chapter is to determine if a similar effect is observed in ruthenium liner layers. The addition and segregation of Al in Ru layers is of interest as it may improve the diffusion barrier properties of the Ru film by forming an AlO_x layer upon its interaction with the underlying dielectric. Given that a small concentration of Al in Ru films is unlikely to impact upon the excellent Cu plating attributes of the Ru liner, the Al-Ru system may be a viable option to act as a liner and exhibit Cu diffusion barrier characteristic.

4.2 Experimental details

Thermally grown SiO_2 layers on Si(111), with a measured thickness of 5.4 nm, were grown using the Semitool dry oxidation process in a Thermoco 9002 series furnace at 850 °C. The SiO_2 surfaces were prepared using a standard degreasing procedure of successive dips in acetone, methanol and isopropyl alcohol (IPA) before being loaded into a UHV deposition and analysis system. SiO_2 samples were then degassed at ~200 °C for 4 hours, with the UHV chamber reaching a maximum pressure of 5×10^{-9} mbar during degassing. The 3 nm Ru thin films were degassed in UHV at 300 ^{o}C for 3 hours, resulting in the removal of surface oxide as determined by XPS.[3] The XPS analysis was carried out using the XPS setup described in section 3.2. A high temperature annealing study up to 600 ^{o}C was carried out in ultra-high-vacuum (UHV) at a pressure of $\sim 5 \times 10^{-9}$ mbar, with samples kept at the target temperature for 60 minutes. Ultra-thin Al layers were deposited in-situ using thermal evaporation from a W filament, at a base pressure of $\sim 5.0 \times 10^{-8}$ mbar. The XPS core level spectra were curve fitted as described in section 3.2.[4] The Al metal peak was curve fitted using a Doniac-Sunjic line shape in order to allow for the asymmetric nature of the metal peak. The FWHM and asymmetry parameters were obtained from an Al reference sample which showed no evidence of O or C contamination to within the detection limit of XPS.

4.3 Investigation of the interaction of Al on SiO_2

Approximately 2 nm of Al was deposited onto a 5.4 nm thermally grown SiO_2 layer in the absence of Ru and the Al/SiO_2 system was subsequently thermally annealed up to 600 ^oC. The focus of this experiment was to develop an understanding of the inherent chemical interactions at the Al/SiO_2 interface in the absence of Ru, so that the impact of the Ru liner may be accurately determined in section 4.4. Figure 4.1 shows the progression of the O 1s and Al 2p core level peaks through the experimental cycle. It is evident from the curve fitted Al 2p spectrum that the Al was in a primarily metallic state (~80%) upon deposition, as evidenced by the presence of a component peak at ~72.7 eV.[5] An additional component peak at a BE position of ~75 eV is also present which has been identified as Al_2O_3 in agreement with previous studies,[6] attributed to oxidation of the Al film due to the presence of residual O within the UHV chamber during deposition. In agreement with this, there is also evidence for a small component peak on the LBE side of the SiO_2 O 1s peak attributed to the presence of this limited amount of Al_2O_3. It is clear from the Al 2p peak in Figure 4.1 that the area of the Al_2O_3 component grows with thermal anneal, suggesting the conversion of Al metal to Al_2O_3. The area of the Al_2O_3 component at a binding energy position of 531.8 eV in the O 1s peak profile also grows with respect to that of SiO_2.

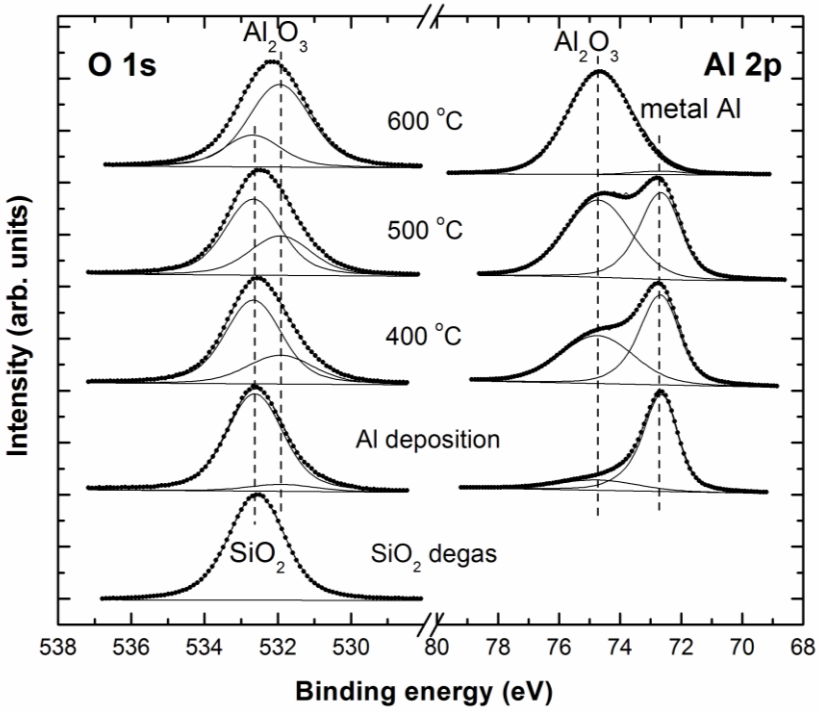

Figure 4.1 O 1s and Al 2p spectra taken from the Al/SiO_2 surface following Al deposition and subsequent UHV thermal annealing treatments**.** (BE positions in O 1s - SiO_2 = 532.7 eV, Al_2O_3 = 531.8 eV: BE positions in Al 2p – metal Al = 72.7 eV, Al_2O_3 = 75.3 eV). All peak fitting parameters included in Appendix A.

While it is possible that the conversion of Al metal to Al_2O_3 is partially due to the presence of residual chamber O during thermal anneal, the reduction in the intensity of the Si 2p signal in SiO_2 shown in Figure 4.2 strongly indicates that the Al layer was converted to Al_2O_3 due to the reduction of the SiO_2 following thermal annealing. This is in agreement with Bauer et. al.[7] who reported the self-limiting conversion of SiO_2 to Al_2O_3 under similar

experimental conditions. Al_2O_3 is thermodynamically more stable than SiO_2 with Gibbs free energies of -1582.3 kJ/mol and -856.4 kJ/mol, respectively,[8] supporting the results outlined. The Si 2p spectra in Figure 4.2 also shows the growth of the Si component peak at a BE position of ~99 eV with respect to the SiO_2 bulk, concurrent with the growth of Al_2O_3. This is as a result of the reduction of SiO_2 during the formation of Al_2O_3, leaving Si at the interface at a BE indistinguishable from the Si substrate signal. The presence of a Si peak at ~99 eV prior to Al deposition is due to the fact that the sampling depth of the XPS exceeds the thickness of the 5 nm SiO_2 film. At this point it is important to note that the release of Si during the formation of Cu diffusion barrier layers is undesirable as it can potentially migrate into the adjacent copper wiring leading to an increase in interconnect line resistance and the consequent degradation of device performance as outlined in chapter 3.[9,10]

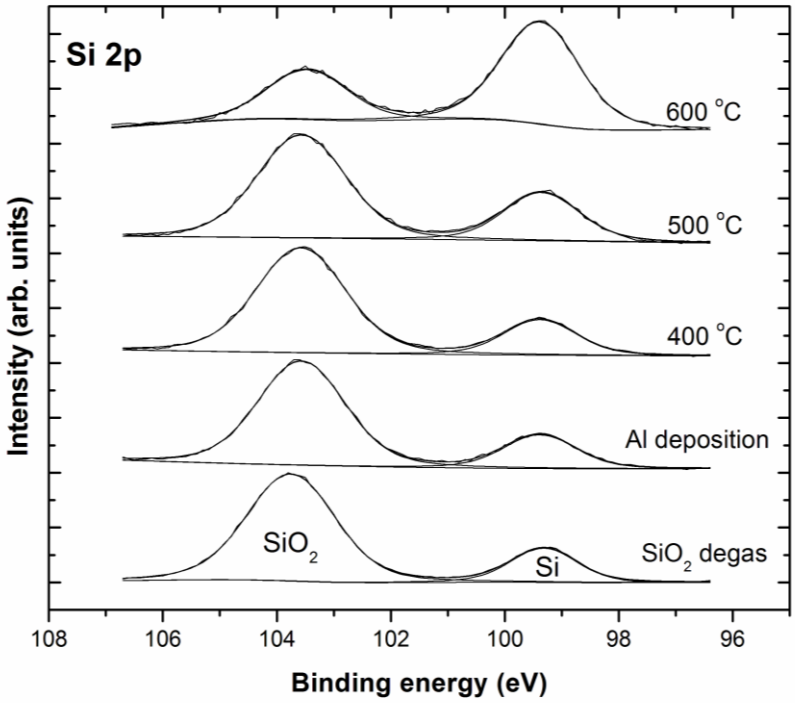

Figure 4.2 Si 2p spectra taken from the SiO_2 surface following Al deposition and subsequent UHV thermal annealing treatments showing the reduction of the oxide and the presence of unbonded silicon. All peak fitting parameters included in Appendix A.

4.4 Investigation of the addition of Al into Ru thin films

Atomic force microscopy (AFM) and scanning electron microscopy (SEM) analysis taken from the 3 nm ALD Ru film deposited on SiO_2 (data not shown) suggested the layer was "flat" and continuous, with an average surface roughness of ~0.2 nm as stated in chapter 3. Upon entry into the UHV system, a small surface oxide peak was detected using XPS analysis which was subsequently removed following a degassing procedure described in section 3.3.[3] The removal of surface oxide produced a clean metallic Ru film with a single O 1s component peak attributed to the SiO_2 dielectric substrate beneath the Ru liner layer, as shown in Figure 4.3. Approximately 1 nm of Al was then deposited on the Ru thin film. The deposited Al film was largely metallic (~72%) with a small oxide peak attributed to the presence of residual chamber oxygen during deposition. The chamber pressure during deposition was ~3 x 10^{-8} mbar. Figure 4.3 shows the concurrent growth of the Al_2O_3 components of both the Al 2p and O 1s spectra with thermal anneal, at the same binding energy (BE) positions as reported in the Al/SiO_2 system in section 4.3. It is again possible that some of the Al-oxide growth seen in Figure 4.3 was due to residual oxygen in the UHV chamber during the annealing cycle. However, the emergence of a Si (~99 eV) component peak at 400 ^oC as seen in Figure 4.4, strongly suggests that the Al reduced the SiO_2 substrate and released Si. Given that AFM and SEM studies confirm the continuity of the ~3 nm Ru film on the

SiO_2 surface, it can be stated that in order for the Al to interact with the substrate, the Al must first have diffused though the Ru liner. This is in agreement with the previous studies which have shown that Mn and Cu diffuse through the grain boundaries of Ru liners.[3,11,12] However, the diffusion mechanism of Mn in Ru films is not well understood as a study involving a deposited Mn/Ru composite failed to provide evidence for Mn diffusion.[13] It is suggested that the presence of Mn in this alloying form may restrict the growth of grain boundaries and eliminate diffusion paths. Further studies are required in this regard. It should be noted that structural imaging techniques such as TEM were not used as part of this investigation, and as such, the diffusion mechanism of Al through ultra-thin Ru layers was not conclusively determined in this study. It has also been shown in section 3.4 that Si released beneath Ru films in this manner is likely to diffuse up through the Ru layer,[14] potentially impacting upon the conductivity of the liner and thus affecting both the subsequent copper interconnect deposition and the conductivity of the entire liner/interconnect structure. The limited nature of the conversion of metal Al to Al_2O_3 in this instance should be noted, suggesting that only a limited quantity of the metal diffuses through the Ru liner to the Ru/SiO_2 interface. This is in contrast to the Al/SiO_2 system where all the Al metal was converted to Al_2O_3 in the absence of the Ru liner acting to separate the Al and the SiO_2 layers.

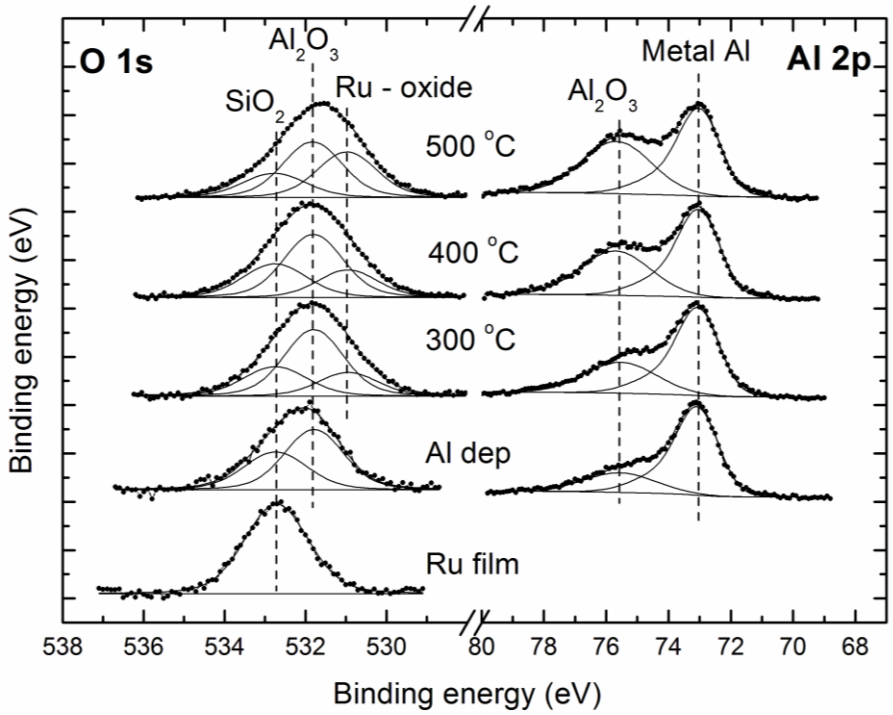

FIG. 4.3 O 1s and Al 2p spectra taken from the Al/3nm Ru/SiO_2 structure following Al deposition and subsequent UHV thermal annealing treatments. (BE positions in O 1s - SiO_2 = 532.7 eV, Al_2O_3 = 531.9 eV, Ru – oxide = 530.9 eV: BE positions in Al 2p – metal Al = 73.1 eV, Al_2O_3 = 75.3 eV). All peak fitting parameters included in Appendix A.

There is an additional component peak on the lower binding energy (LBE) side of the O 1s when compared to the Al/SiO_2 system suggesting that the presence of the Ru film has an impact on the chemical interactions which occur at the Ru/SiO_2 interface. Additionally, Figure 4.4 shows the concurrent growth of a peak on the HBE side of the Ru $3d_{5/2}$ spectrum providing evidence for the chemical interaction of Ru with the interfacial structure. This is in contrast to the Mn/Ru system where the chemical state

of the Ru liner remained unchanged during the formation of Mn-silicate at the Ru/SiO_2 interface as shown in Chapter 3.[3] In a separate experiment, Ru was deposited by e-beam evaporation on a fully formed Al_2O_3 film and the sample was subsequently annealed up to 500 ^oC in UHV. In this case, there was no indication of any chemical interaction between the Ru and the underlying Al_2O_3 film. It has been reported that Al_2O_3 is thermodynamically more stable than Ru oxide.[15] As such, the evidence suggests that the additional component peaks seen in both the O 1s and Ru $3d_{5/2}$ are unlikely to be due to the interaction of Ru with Al_2O_3, but rather the formation of a Ru-oxide phase resulting in the partial oxidation of the Ru film, however this requires further investigation. The interaction of Ru metal with O in this manner may reduce the conductivity of the Ru liner and increase the overall line resistance. There is also some evidence for peak broadening on the LBE side of Ru $3d_{5/2}$ suggesting the interaction of Ru with a more electropositive element such as Si or Al. Given the Al 2p peak fits well with identical peak fitting parameters as those used in the Al/SiO_2 system in the absence of Ru (Figure 4.1), the broadening of the Ru $3d_{5/2}$ is unlikely to be due to a Ru-Al interaction.

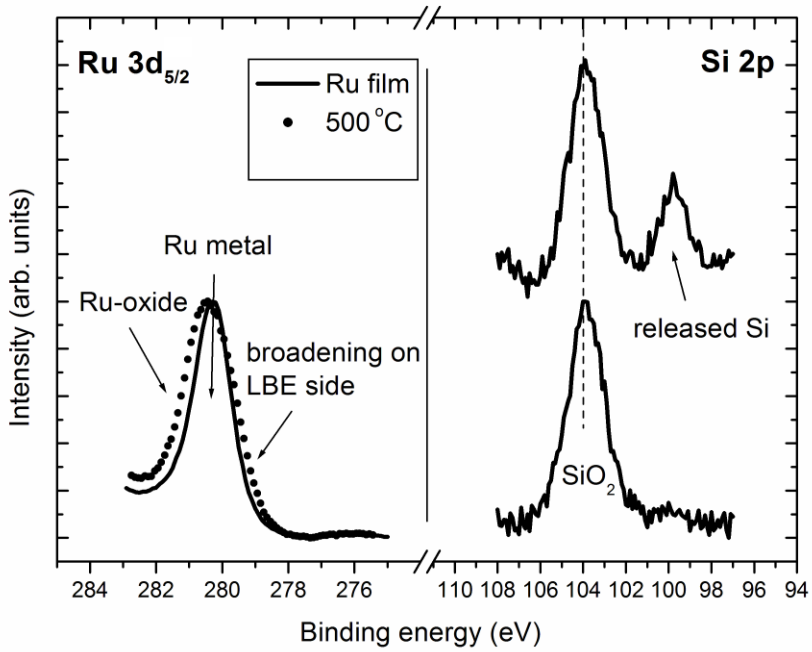

Figure 4.4 Ru $3d_{5/2}$ and Si 2p spectra taken from the Al/3 nm Ru/SiO_2 structure. The Ru $3d_{5/2}$ shows the growth of an additional HBE component due to the interaction of Ru-O following thermal anneal. There is also evidence for peak broadening on the LBE side of the Ru $3d_{5/2}$ which will be discussed in section 4.5. The Si 2p spectra show the emergence of released Si following a 400 ^{o}C thermal anneal.

4.5 Investigation of silicon on 3 nm Ru thin films

These investigations have shown that the formation of Al-based barrier layers on SiO_2 results in the release of free Si. There is also some evidence for the interaction of Ru with a more electropositive element such as Si in Figure 4.4. As such it is important to determine the potential impact free Si could have on the liner/barrier layer structure. It has been reported that

mobile Si in Cu lines results in device degradation and a reduction in line performance.[9,10] However, little work has been performed on the chemical interaction of Si with Ru liner layers. Although Ru and Si were both present in the system described in chapter 3,[3] there was no evidence for the interaction of Ru with Si. This could be explained by the fact that Si was consumed in the Mn/SiO_2 system in the formation of Mn-silicate resulting in a minimal amount of released Si. Comparatively, the quantity of Si released in the Al/SiO_2 system is substantial as the formation of Al_2O_3 at the interface does not consume Si making the XPS detection of any potential Si-Ru interaction more likely. It should also be noted that the energy of the photoelectrons which emerge from Si in the Ru-Si complex outlined in this study are very close to the binding energy position of the first Si sub oxide state. As such, unambiguously determining the presence of small quantities of Ru-silicide is difficult. In order to determine if any such interaction does occur upon the incorporation of Si into the Ru layer, approximately ~2 nm of Si was e-beam deposited directly on a 3 nm ALD Ru thin film in order to provide sufficient Si at the Ru surface to observe any chemical interaction thereby simulating the incorporation of abundant released Si from the substrate in the Ru liner. Figure 4.5 shows the Si peak in the Si 2p spectrum at a BE position of ~99 eV upon Si deposition, identical to the BE position of the released Si peak from the SiO_2 dielectric for annealed Al layers in the absence of Ru as observed in Figure 4.2. While the deposited Si film is

predominantly unoxidized, there are small concentrations of higher oxidation states present. The Si/Ru structure was then subject to thermal annealing at 400 ^{o}C resulting in the concurrent growth of additional component peaks on the HBE of the Si 2p (shifted by 0.3 eV) and the LBE side of the Ru 3d (shifted by 0.4 eV) suggesting a chemical interaction between Ru and the deposited Si consistent with the formation of Ru-silicide (Ru_2Si_3),[16] based on the electronegativity difference between Si (1.9) and Ru (2.2).

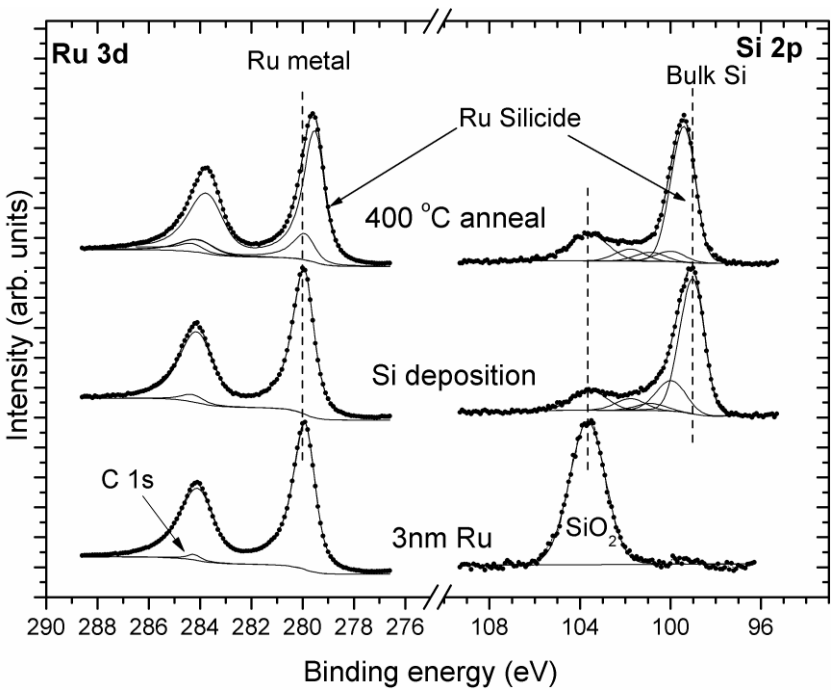

Figure 4.5 Ru $3d_{5/2}$ and Si 2p spectra taken from deposited Si on a 3 nm ALD Ru film. The spectra show the growth of Ru-silicide with thermal anneal. (BE positions in Ru $3d_{5/2}$ – R metal = 280.0 eV, Ru silicide = 279.6 eV. BE positions in Si 2p – SiO2 = 103.7 eV, bulk Si = 99.3 eV, Ru silicide = 99.6 eV). All peak fitting parameters included in Appendix A.

It should be noted that all of the Si in Figure 4.5 has been converted to Ru-silicide, along with a substantial quantity (~80%) of the Ru film indicating the ease of formation at this temperature. Peak fitting analysis of the Ru 3d spectra reveal a BE separation between the Ru-silicide peak and the Ru metal of ~0.4 eV. The Ru 3p spectra (not shown) also displayed a Ru-silicide peak on the LBE side of the metal with a BE separation of ~0.4 eV to the bulk. This experiment shows that Ru-silicide readily forms where the two species are present in their elemental form and in sufficient quantities. Therefore the diffusion of Al through the deposited Ru layer and its subsequent interaction with the underlying dielectric thereby releasing silicon, could result in the formation of a Ru-silicide interlayer which has previously been proposed as a possible diffusion barrier layer.[16] This material system warrants further study in terms of assessing its potential application as a diffusion barrier layer between the dielectric and subsequently deposited Cu.

4.6 Conclusions

In summary, it has been shown that Al deposited on a 5.4 nm SiO_2 film results in the formation of Al_2O_3 during thermal anneal which is accompanied by the release of Si from the dielectric surface. In a separate experiment Al was deposited on a 3nm ALD Ru film and annealed to 500 °C. It was shown that thermal annealing results in the diffusion of Al through the liner layer and the subsequent chemical interaction with the underlying SiO_2 dielectric substrate to form Al_2O_3, Ru-silicide and Ru-oxide at the Ru/SiO_2 interface. XPS analysis of the Si 2p also indicates the concurrent release of Si from the SiO_2 dielectric layer. The chemical interaction of Si with Ru has also been shown which may have possible diffusion barrier layer applications.

4.7 References

[1]Dung-ChingPerng, Jia-Bin Yeh, Kuo-Chung Hsu,Shuo-Wen Tsai,Thin Solid Films **518**, 1648–1652 (2010).

[2]K. Maekawa, K. Mori, N. Suzumura, K. Honda, Y. Hirose, K. Asai, A. Uedono, M.Kojima, Microelectron. Eng. **85,** 2137 (2008).

[3]A. P. McCoy, P. Casey, J. Bogan, J. G. Lozano, P. D. Nellist, and G. Hughes, Appl. Phys. Lett. **101**, 231603 (2012).

[4]P. Casey, J. Bogan, B. Brennan, and G. Hughes, Appl. Phys. Lett. **98**, 113508 (2011).

[5]Yong-Chun Kim, Hyung-Ho Park, John S. Chun, Won-Jong Lee, Thin Solid Films **237**, 57-65 (1994).

[6]T. J. Sarapatka, J. Phys. Chem **97**, 11274-11277 (1993).

[7]R. S. Bauer, R. Z. Bachrach, and L. J. Brillson, Appl. Phys. Lett. **37**, 1006 (1980).

[8]Lange's handbook of chemistry, 70th anniversary edition.

[9]M.J. Frederick, R. Goswami, and G. Ramanath, J. Appl. Phys. **93**, 5966 – 5972 (2003).

[10]Wen-Fa Wu, Kou-Chiang Tsai, Chuen-Guang Chao, Jen-Chung Chen, Keng-Liang Ou, J. Electron. Mater. **34**, 1150 – 1156 (2005).

[11]T. N. Arunagiri, Y. Zhang, and O. Chyan, M. El-Bouanani and M. J. Kim, K. H. Chen, C. T. Wu and L. C. Chen, Appl. Phys. Lett. **86**, 083104 (2005).

[12]M. Damayanti T. Sritharan, Z. H. Gan,S. G. Mhaisalkar, N. Jiang, and L. Chanb, J. Electrochem. Soc. **153**, J41 – J45 (2006).

[13]H. Wojcik, R. Kaltofen, C. Krien, U. Merkel, C. Wenzel, J. W. Bartha, M. Friedemann, B. Adolphi, R. Liske, V. Neumann, and M. Geidel, in IEEE International Interconnect Technology Conference and 2011 Materials for Advanced Metallization (IITC/MAM), 8–12 May 2011 (2011), pp. 1–3.

[14]A. P. McCoy, P. Casey, J. Bogan, C. Byrne, and G. Hughes, Appl. Phys. Lett. **102**, 201603 (2013).

[15]C. Mallikaa and O. M. Sreedharana, Journal of the Less Common Metals, **162**, 51 (1990).

[16]L. Pasquali, N. Mahne, M. Montecchi, V. Mattarello and S. Nannarone, J. Appl. Phys. **105**, 044304 (2009)

[17]Brian A. Vaarstra et al. Ruthenium silicide diffusion barrier layers and methods of forming same, patent number: 6197628, filing date Aug 27, 1998.

Chapter 5

In-situ investigations into the mechanism of O catalysis on Ru/Mn surfaces and the thermodynamic stability of Ru/Mn based Cu diffusion barrier layers

5.1 Introduction

Numerous studies[1,2,3] have shown that alloying of transition metals increases the catalytic activity of metal surfaces towards oxygen, which can be measured experimentally as changes to various catalytic descriptors. These descriptors include adsorption energy which is a limiting factor for O_2 dissociation, and the thermodynamic stability of intermediate chemical species adsorbed on the surface following O_2 dissociation, which is a limiting factor for the formation of reaction products.[3] However, the mechanism behind these changes have not been understood within the literature. The theoretical model used most extensively to explain this effect is known as the d-band theory, which correlates the catalytic activity of transition metals with changes in the energy of the d-band centre.[2,3] However, numerous other studies have shown results inconsistent with d-band model predictions,[4,5] including a recent photoemission spectroscopy

study by Hofmann et al[6] which found no correlation between the d-band centre and catalytic activity descriptors.

It has been suggested that one of the major challenges to improving the fundamental understanding of this O reactivity mechanism is the difficulty in adsorbing significant amounts of dissociated O on catalytic surfaces within controlled ultra high vacuum (UHV) conditions.[7] However, Lescop[8] has shown that O can be dissociatively chemisorbed on Mn surfaces in the form of Mn monoxide (MnO) following UHV O_2 exposure levels as low as 30 Langmuirs. As such, this low barrier to O_2 dissociation allows oxygen dissociation to be achieved on Mn surfaces within a fully controlled UHV environment. In addition to this, other studies have reported high catalytic activity for Ru-Mn based surfaces such as Ru-Mn-Fe [9] and Ru/LaSrMnO.[10] Therefore, Ru/Mn may offer an ideal material system to experimentally investigate the mechanism by which alloying of transition metals increases catalytic activity on bimetallic surfaces.

In the first section of this chapter initial investigations into the inherent catalytic activity of bimetallic Ru/Mn surfaces towards molecular O were performed using in-situ XPS analysis. The focus of this study is to use a fully in-situ UHV experimental procedure in order to determine if the presence of Ru increases catalytic activity on the Mn/Ru surface. Changes

in catalytic activity were measured by investigating the impact of Ru on the thermodynamic stability of an ultra-thin Mn-oxide layer, as represented schematically in Figure 5.1(a). The second section of this study investigates the potential impact of this catalysis on industrial applications by determining if the presence of Ru alters the thermodynamic stability and chemical composition of ultra-thin (~5 nm) mixed phase $MnO/MnSiO_3$ (Figure. 5.1(b).) and single phase $MnSiO_3$ (Figure. 5.1(c)) Cu diffusion barrier layers.[11]

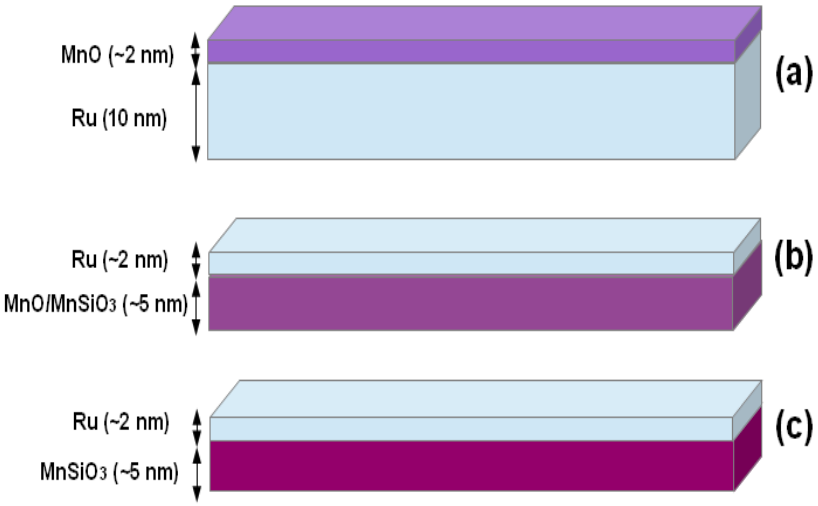

Figure 5.1 Schematic diagram representing the three separate experimental samples analysed in this study: **(a)** represents the formation of a ~2 nm MnO layer on Ru (~10 nm) investigated in section 5.3. **(b)** represents the deposition of a Ru liner layer (~2 nm) onto a mixed phase $MnO/MnSiO_3$ barrier layer (~5 nm) and **(c)** represents the deposition of a Ru liner layer (~2 nm) onto a single phase $MnSiO_3$ barrier layer (~5 nm), both of which will be investigated in section 5.4. All of the above sturctures are on an SiO_2 substrate.

5.2 Experimental details

High quality thermally grown SiO_2 layers on Si(111), with a measured thickness of 5 nm, were grown using the Semitool dry oxidation process in a Thermoco 9002 series furnace at 850 °C. The SiO_2 surfaces were prepared using a standard degreasing procedure of successive dips in acetone, methanol and isopropyl alcohol (IPA) before being loaded into a UHV deposition and analysis system. SiO_2 samples were then degassed at ~ 200 °C for 4 hours, with the UHV chamber reaching a maximum pressure of ~5×10^{-9} mbar during degassing. Ex-situ sputter deposited Ru layers with a nominal thickness of 10 nm were used as substrates for the formation of Ru/Mn bimetallic surfaces. Ru samples were degassed at 400 °C for 4 hours prior to Mn deposition, with the UHV chamber reaching a maximum pressure of 8×10^{-9} mbar during degassing. Mixed phase Mn monoxide (MnO)/Mn silicate ($MnSiO_3$) and single phase $MnSiO_3$ barrier layers were formed on SiO_2 surfaces following 500 °C annealing, using the growth procedure outlined by Casey et al.[11] An Oxford Applied Research EGC04 mini electron-beam evaporator was used for the room temperature evaporation of both Mn and Ru thin films using Mn and Ru source materials of 99.99 % purity at a deposition pressure of ~5×10^{-9} mbar. It should be noted that MnO and $MnSiO_3$ barrier layers with a thickness of ~5 nm were formed in this experiment in order to facilitate XPS analysis of these

surfaces, even though these thicknesses are greater than that required for interconnect applications.

Thermal annealing studies were carried out in-situ at a UHV pressure of ~5 × 10^{-9} mbar, with samples kept at the target temperature for 60 minutes. Following XPS analysis, samples were annealed again to the same temperature for an additional 60 minutes. As no further changes were observed in XPS spectra taken after this second anneal, it was assumed that chemical reactions reached thermodynamic equilibrium following these annealing cycles. This was done in order to ensure that the changes in XPS spectra observed following Ru deposition in Figure 5.4 through Figure 5.7 were due to the interaction of Ru with the barrier layer surface and not simply due to repeated thermal annealing of the barrier layer structure. All thickness values quoted in this study, with the exception of the 10 nm Ru substrate layer, are based on XPS thickness calculations.[12]

Section 5.3 details how a number of factors act to complicate the analysis of XPS data in this study. These include multiplet splitting and shake-up features within the Mn 2p spectrum and surface electron charging effects in the Si 2p spectra. Multiplet splitting can be described in simple terms as an energy coupling interaction between unpaired electrons in the valence shell and unpaired electrons within the core level, which occurs following the

excitation of core level electrons during the photoemission process.[13] The result of this energy coupling for manganese is that Mn 2p spectra taken from a single chemical species contain several multiplet peaks over a energy broad range (~10 eV). Another spectral feature known to affect the analysis of Mn 2p spectra are shake-up features which arise from photoelectrons which have lost energy through the promotion of valence electrons from an occupied energy to a higher unoccupied level. While these factors greatly complicate analysis, Nesbit et al[13] have outlined curve fitting parameters which can be used for the deconvolution of Mn 2p photoemission spectra taken from a number of specific Mn-based chemical species. In this study these curve fitting parameters[13] are used to curve fit Mn $2p^{3/2}$ spectra taken from Mn monoxide (MnO) surfaces. This allows MnO, a single chemical species, to be identified using six spectral lines. However, no such parameters are available for the Mn silicate species $MnSiO_3$, and attempting to curve fit Mn 2p spectra originating from $MnSiO_3$ using the parameters outlined for MnO would not be an accurate or relevant deconvolution of the XPS data. Therefore, Mn 2p spectra taken from $MnSiO_3$ and mixed phase $MnSiO_3$/MnO surfaces are presented as non-curve fitted data.

The XPS analysis was carried out using the XPS setup mentioned in section 3.2. The XPS core level spectra were curve fitted using Voigt profiles composed of Gaussian and Lorentzian line shapes in a 3:1 ratio and using a

Shirley-type background. The FWHM of the Si 2p bulk peak was 0.9 eV, with SiO_2 and Mn silicate component peaks in the range 1.1 eV to 1.2 eV. The FWHM of the O 1s SiO_2 component was 1.2 eV with Mn-silicate and Mn-oxide peaks in the range of 1.2 eV to 1.1 eV. Curve fitting parameters for the Mn $2p_{3/2}$ MnO spectrum are in agreement with Nesbit et al[13] while the metallic Mn peaks are curve fitted using a Voigt-asymmetric line-shape.

5.3 O_2 catalysis on bimetallic Ru/Mn surfaces

The catalytic activity of bimetallic Ru/Mn surfaces towards O_2 was investigated using XPS following a series of in-situ O_2 exposure and thermal annealing treatments. For the purpose of clarity it should be noted that the sample used in this experiment is schematically represented in Figure 5.1(a). While previous studies have reported the use of Ru/Mn based catalysts,[9,10] a fully in-situ ultra high vacuum experimental procedure has not been used to study the fundamental mechanism of molecular O catalysis on these surfaces. Ru substrate layers with a nominal thickness of 10 nm were loaded into the UHV system and thermally degassed using the procedure previously outlined in section 3.2. Photoemission core level spectra taken from the degassed surface (not shown) showed no evidence of O contamination within the O 1s and C 1s / Ru $3d_{3/2}$ spectra, to within the detection limit of XPS in agreement with previous results.[4] An ultra thin (~1 nm) metallic Mn layer was subsequently deposited onto the clean Ru

surface using in-situ electron beam evaporation. The Mn $2p_{3/2}$ spectrum taken from the deposited Mn film is shown in Figure 5.2, while the corresponding O 1s and Ru $3d_{5/2}$ spectra are shown in Figure 5.3. It should be noted that the Mn $2p_{3/2}$ and Ru $3d_{5/2}$ spectra taken following Mn deposition are identical to corresponding spectra taken from Mn and Ru reference materials (not shown). As such there is no evidence for the formation of any inter-metallic phases between the Mn and Ru layers, in agreement with Wojcik et al.[14]

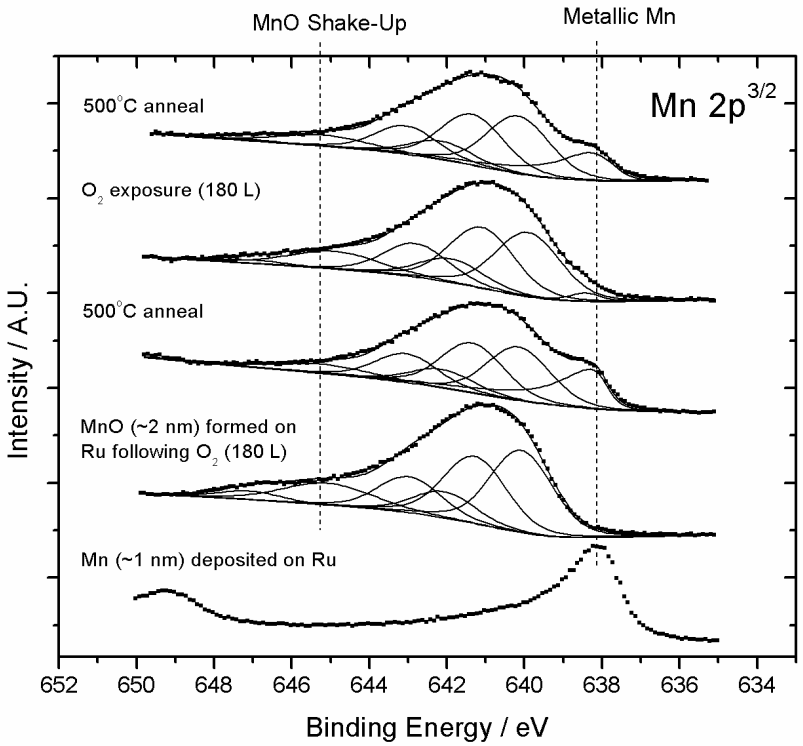

Figure 5.2 Non-normalised and curve fitted [13] Mn $2p_{3/2}$ XPS spectra taken following the deposition of a ~2 nm Mn film onto Ru and subsequent O_2 exposure and thermal annealing treatments. Spectra show the formation of metallic Mn and sub-stoichiometric Mn following 500 °C annealing, attributed to MnO dissociation. (BE positions in Mn 2p – metallic Mn = 638.1 eV, MnO shake-up = 645.2 eV). All peak fitting parameters included in Appendix A.

The interaction of the Ru/Mn surface with molecular O was subsequently investigated through controlled exposure to O_2 at a partial pressure of ~1 × 10^{-7} mbar for 30 minutes, amounting to a total O_2 exposure of 180 Langmuirs (180 L). It should be noted that the impact of Ru on the rate of O adsorption on the Mn surface was not investigated as part of this study. The

curve fitted XPS Mn $2p_{3/2}$ spectrum taken following O_2 exposure is shown in Figure 5.2. The spectrum shows the complete oxidation of the Mn film as evidenced by the removal of the metallic Mn component peak at ~638 eV binding energy (BE). The Mn-oxide species formed following O_2 exposure was identified as Mn monoxide (MnO) based on the Mn $2p_{3/2}$ curve fitting analysis procedure outlined previously.[13] However, it should be noted that the morphology of the corresponding Ru $3d_{3/2}$ spectrum in Figure 5.3 shows no change in spectral profile following O_2 exposure suggesting no Ru oxidation occurred on the Ru/Mn surface within the detection limit of XPS. These results are in agreement with the corresponding O 1s spectrum in Figure 5.3 which shows the formation of a single component peak at 530.0 eV binding energy (BE) attributed to MnO, as previously reported.[11,15] It should be noted that the morphology and continuity of the Mn layer was not measured following deposition onto the Ru surface. Therefore, while there is no evidence of Ru oxidation following O_2 exposure, it cannot be stated conclusively that O_2 dissociation did not occur on "uncovered" areas of the Ru surface. Previous studies[16] have shown that MnO is formed through the dissociative chemisorption of oxygen on Mn surfaces and as such it is suggested that this is the primary mechanism for O_2 dissociation on the bimetallic Ru/Mn surface.

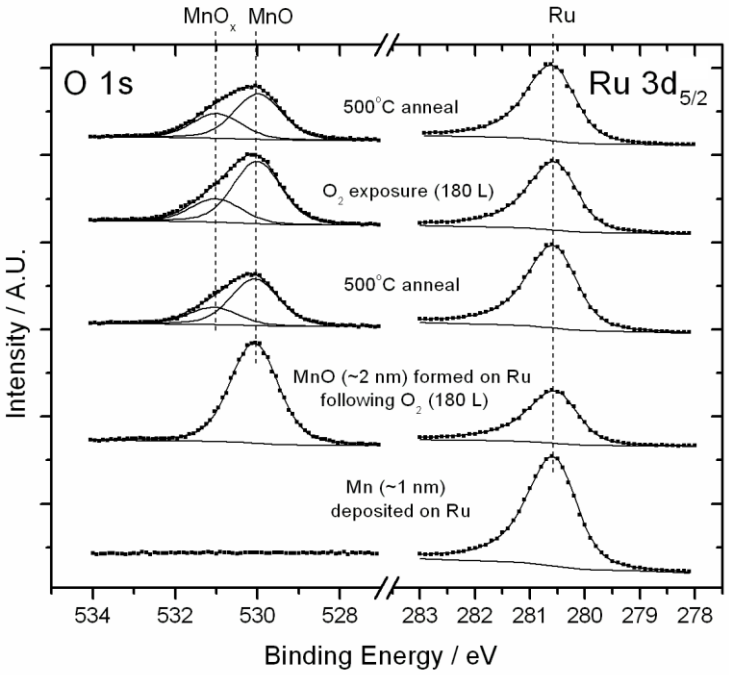

Figure 5.3 Non-normalised and curve fitted O 1s and Ru $3d_{5/2}$ XPS spectra corresponding to Figure 5.1. MnO dissociation following 500 °C annealing is shown by a reduction in the integrated area of relevant O 1s MnO component peak, which results in a corresponding change in the attenuation of the Ru $3d_{5/2}$ peak. For the purpose of image clarity the intensity of each of the Ru $3d_{5/2}$ spectra are magnified by a factor of 1.6. (BE positions in O 1s – MnOx = 531.1 eV, MnO = 530.1 eV; BE positions in Ru $3d_{5/2}$ – Ru metal = 280.6 eV). All peak fitting parameters included in Appendix A.

The thermodynamic stability of MnO chemisorbed on Ru/Mn surfaces was subsequently investigated using a series of high temperature in-situ UHV annealing treatments. The Mn $2p_{3/2}$ spectrum in Figure 5.2 taken following 500 °C annealing shows the re-emergence of a metallic Mn component peak at ~638 eV along with a reduction in the intensity of the MnO shake-up

feature at ~645.5 eV.[33] These results suggest that 500 °C annealing resulted in the dissociation of MnO on the Ru/Mn surface leading to the formation of metallic Mn along with a sub-stoichiometric Mn-oxide species labelled MnO_x (where $x < 1$). The corresponding O 1s spectrum in Figure 5.3 is consistent with these findings, showing a 50 % reduction in the integrated area of the MnO component peak along with the formation of an additional component peak at ~531 eV BE attributed to the MnO_x species. As stated previously, the focus of this study is to determine if the presence of Ru impacts upon catalytic activity by changing the thermodynamic stability of the chemisorbed MnO species on the Ru/Mn surface. Therefore, it is important to note that the thermal dissociation of MnO on Ru/Mn surfaces following 500 °C annealing is in contrast to results taken from a MnO control sample which showed no evidence of MnO dissociation following 700 °C annealing in the absence of Ru. As such it is suggested that the presence of Ru acts to "weaken" the Mn-O bond and reduce the MnO dissociation barrier, hence increasing the catalytic activity of the surface.[17] It should also be noted that the peak profile of the Mn 2p spectrum taken from the MnO control layer was the same as that taken from the ~2 nm MnO layer in Figure 5.2 and as such spectra from the control sample are not shown in this study.

XPS spectra taken following a further series of O_2 exposure and thermal annealing treatments, shown in Figure 5.2 and Figure 5.3, confirm this result. These spectra show the oxidation of metallic Mn on the Ru/Mn surface following a second O_2 exposure (180 L) as evidenced by the reduction of the metallic Mn component peak in the Mn $2p_{3/2}$ spectrum and a corresponding increase in the integrated area of the O 1s MnO component peak. However, spectra taken following a subsequent 500 °C thermal anneal again show the re-emergence of the metallic Mn component in Figure 5.2 along with a concurrent reduction in the O 1s MnO peak area, suggesting that the dissociation of MnO on Ru/Mn surfaces at 500 °C is a repeatable process.

Reduction of the MnO dissociation energy on the Ru/Mn surface is in agreement with previous studies[1,2,3] which have shown that catalytic activity can be increased through the alloying of transition metals. However, as stated previously, the mechanism for oxygen catalysis on bimetallic surfaces has not been conclusively understood within the literature.[6] One suggested mechanism for this process is that strain caused by combining metals with different lattice constants alters the electronic structure of the metal surface leading to changes in adsorbate dissociation energy.[1,2] Therefore, based on this theory, oxygen catalysis on bimetallic surfaces is not induced through chemical changes in both surface metals. The Ru $3d_{5/2}$ spectra in Figure 5.3

provide experimental evidence in agreement with this as the spectra show no evidence of chemical change within the Ru layer during the experiment. It should be noted that while reaction kinetics were not investigated as part of this study, the XPS spectra in Figure 5.3 clearly show that the Ru is present in a metallic state when the Ru/Mn surface returns to a state of thermodynamic equilibrium following thermal annealing. These results do not preclude the formation of Ru based intermediate chemical species during the MnO dissociation process. As such, further study is required to conclusively determine the mechanism by which Ru reduces the dissociation energy of MnO. It should also be noted that the O 1s spectra in Figure 5.3 show a reduction in total peak area equal to 30 % following the first 500 °C anneal, suggesting that the presence of Ru reduces the barrier to oxygen desorption from the Ru/Mn surface following MnO dissociation. While Deng et al [7] have previously reported the thermal desorption of O_2 from catalytic gold surfaces, the chemical or electronic state of the O desorbed from the Ru/Mn surface during MnO dissociation has not been determined as part of this study.

As stated previously, two of the limiting factors for the formation of reaction products in heterogeneous gas catalysis experiments are the rate of gas dissociation on the catalyst surface and the thermodynamic stability of the intermediate species dissociatively chemisorbed on the catalyst surface.

Therefore, it should be noted that the results of this study show that Ru/Mn surfaces offer a high rate of O_2 dissociation in addition to the ability to reduce the dissociation energy of chemisorbed MnO in the presence of Ru. As such, while specific applications for bimetallic Ru/Mn catalytic surfaces are not investigated as part of this study, it may be suggested that these surfaces offer an interesting material system for potential applications in heterogeneous gas catalysis.

5.4 Impact of Ru catalysis on the thermodynamic stability of preformed Mn-O based barrier layers

The thermodynamic stability of preformed Mn-O based Cu diffusion barrier layers in contact with Ru liners was investigated in two separate experiments. In the first experiment a mixed phase $MnSiO_3$/MnO barrier with a thickness of ~5 nm which was formed on a SiO_2 surface following 500 °C annealing.[11] Following barrier formation a Ru layer (~2 nm) was deposited onto the $MnSiO_3$/MnO surface, as represented schematically in Figure 5.1(b). Figure 5.4 shows O 1s and Si 2p spectra taken from the surface before and after barrier layer formation. The curve-fitted O 1s spectrum shows clear evidence for the presence of both $MnSiO_3$ and MnO within the barrier layer region as evidenced by the presence of component peaks at 531.4 eV and 530.0 eV BE respectively, as previously reported.[11,15]

The corresponding Si 2p spectrum is consistent with this analysis, showing the presence of a $MnSiO_3$ component peak separated from the SiO_2 component by 1.3 eV, in agreement with previous studies.[11,18] Non-curve fitted Mn $2p_{3/2}$ spectra taken from the $MnSiO_3$/MnO surface are shown in Figure 5.5. As described earlier, curve fitting parameters have not been established for Mn 2p spectra taken from $MnSiO_3$ surfaces, however, based on the non-curve fitted data in Figure 5.5 it can be clearly stated that there is no metallic Mn present on the surface following barrier layer formation.

Therefore, using combined analysis of the O 1s, Si 2p and Mn 2p spectra, the chemical composition of the $MnSiO_3$/MnO layer was determined. Angular dependent spectra taken from the surface suggest that the MnO layer was surface localised with respect to the $MnSiO_3$. This is attributed to the interaction of deposited MnO with the underlying SiO_2 forming $MnSiO_3$ at the "buried" interface,[11] resulting in the presence of residual un-reacted MnO on the barrier layer surface.

An ultra-thin (~2 nm) Ru film was subsequently deposited on the $MnO/MnSiO_3$ surface using in-situ electron beam evaporation and the corresponding spectra are shown in Figure 5.4 and Figure 5.5. It should be noted that the corresponding Ru 3d spectra (not shown) had an identical spectral profile to those shown in Figure 5.3 indicating that the deposited Ru film was in a metallic state. The O 1s spectrum in Figure 5.4 shows no changes in spectral profile following Ru deposition, while the corresponding Si 2p spectrum shows no change in the relative intensities of the SiO_2, $MnSiO_3$ and Si^0 component peaks. As such, results show no evidence of changes in chemical composition at the $Ru/MnO/MnSiO_3$ interface following room temperature deposition.

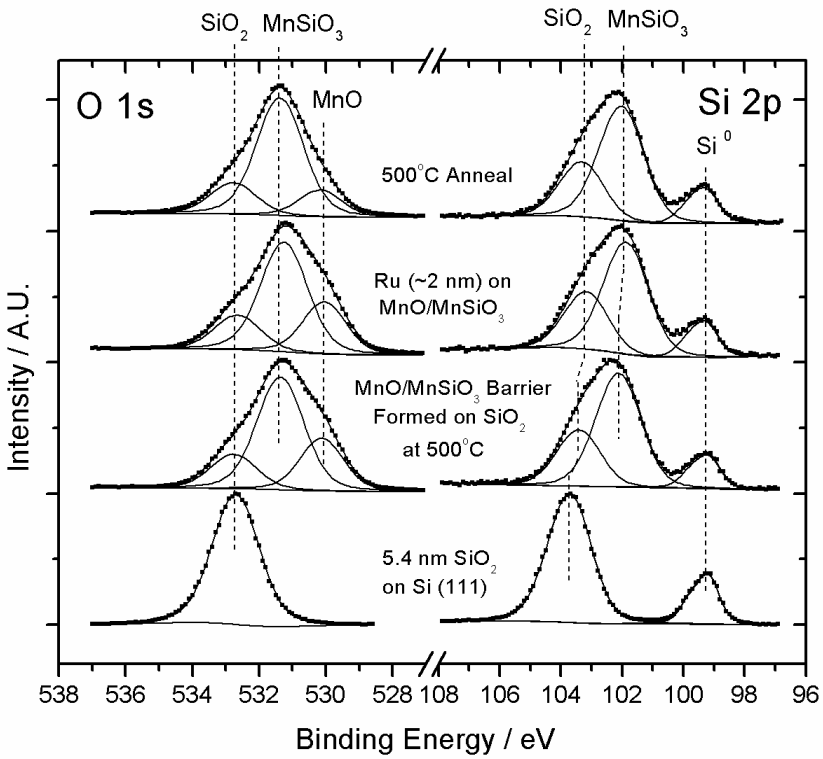

Figure 5.4 Normalised and curve fitted O 1s and Si 2p XPS spectra showing the interaction of Ru (~2 nm) with a mixed phase $MnO/MnSiO_3$ barrier layer (~5 nm). O 1s spectra show the dissociation of MnO within the barrier layer following interaction within Ru at 500 °C. (BE positions in O 1s – SiO_2 = 532.7 eV, $MnSiO_3$ = 531.5 eV, MnO = 530.1 eV; BE positions in Si 2p – SiO_2 = 103.8 eV, $MnSiO_3$ = 102.2 eV, Si^0 = 99.3 eV). All peak fitting parameters included in Appendix A.

It should be noted that changes in the BE separation between the Si 2p substrate component (Si^0) and the SiO_2 component are observed in Figure 5.4 following the formation of $MnSiO_3$ on the SiO_2 surface. It has been shown by Iwata et al [19] that this BE separation value may be increased as a function of increasing SiO_2 thickness, due to the build-up of surface

electronic charge during the photoemission process. Therefore, the reduction in BE separation observed in Figure 5.4 is attributed to a reduction in SiO_2 thickness as a function of $MnSiO_3$ growth, as previously reported by Casey et al.[11] A similar effect is also observed in the Si 2p spectrum in Figure 5.4 following Ru deposition onto the barrier layer surface and this change is again attributed to changes in surface electron charge in agreement with Ofner et al.[20] The affects of surface charging are accommodated for during the peak fitting process by linking the BE position of the Mn-silicate component to that of the SiO_2 component, using a BE separation of 1.4 eV in agreement with previous studies.[11,18]

The sample was subsequently annealed to 500 °C in order to determine if the presence of Ru impacted upon the thermodynamic stability of the barrier layer. The O 1s spectrum in Figure 5.4 shows a significant reduction in the intensity of the MnO component peak following 500 °C thermal annealing, while the corresponding Mn 2p spectrum also shows a concurrent growth of the metallic Mn component peak. Based on these results, it is suggested that the presence of Ru on the surface of $MnO/MnSiO_3$ barrier layers results in the dissociation of MnO and the formation of metallic Mn. The corresponding Ru 3d spectra taken from the $Ru/MnO/MnSiO_3$ surface (not shown) again showed no evidence of any changes in the chemical composition of the Ru layer, in agreement with the results in Figure 5.3. It

should be noted that while the O 1s spectra in Figure 5.4 show clear evidence for MnO dissociation following 500 °C annealing, there is no conclusive evidence for the dissociation of $MnSiO_3$ within the mixed phase barrier. However, given that XPS results suggest that the MnO was surface localised with respect to the $MnSiO_3$ within the barrier layer it may be suggested that the deposited Ru was not in direct contact with the $MnSiO_3$ species.

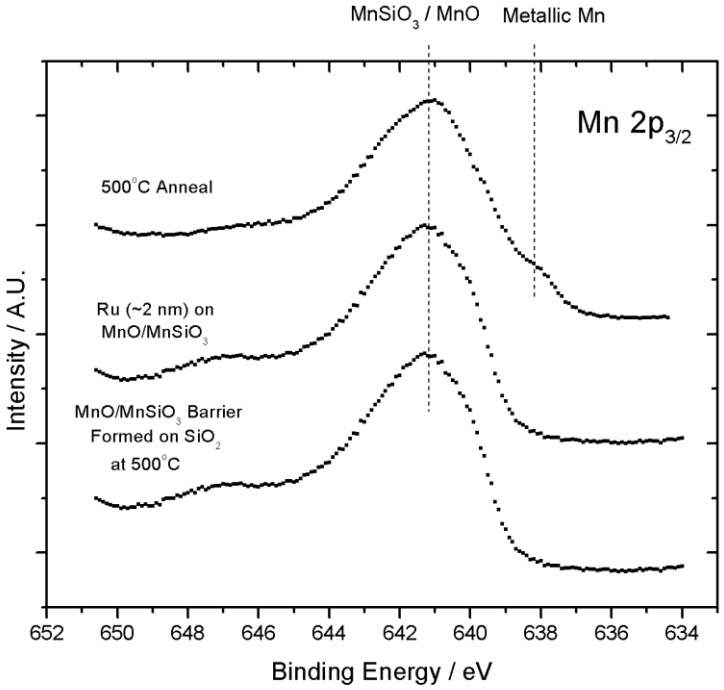

Figure 5.5 Normalised and non-curve fitted Mn $2p_{3/2}$ XPS spectra corresponding to Figure 5.3. Spectra show the formation of metallic Mn following MnO dissociation at 500 °C. (BE positions in Mn 2p; metallic Mn = 638.1 eV, MnSiO3/MnO = 641.1 eV).

Therefore, in a separate experiment the impact of a Ru liner layer on the chemical composition of a single phase $MnSiO_3$ barrier layer was also investigated, with this sample being represented schematically in Figure 5.1(c). Figure 5.6 and Figure 5.7 show XPS spectra taken from an $MnSiO_3$ layer with an approximate thickness of ~5 nm formed on SiO_2 following 500 °C anneal. The O 1s spectrum in Figure 5.6 taken following $MnSiO_3$ formation shows no evidence for Mn-oxide (530.1 eV) while the corresponding Mn 2p spectrum shows no evidence for the presence of metallic Mn (638.2 eV) within the barrier layer region. Following $MnSiO_3$ formation a ~2 nm Ru layer was deposited onto the surface and thermally annealed to 500 °C, with all relevant spectra being shown in Figure 5.6 and Figure 5.7. It can be seen from the Mn 2p spectra in Figure 5.7 that 500 °C annealing results in the formation of metallic Mn within the $MnSiO_3$ barrier layer. In agreement with this, the corresponding Si 2p and O 1s spectra in Figure 5.6 show a concurrent reduction in the intensity of the $MnSiO_3$ component peaks, observable as a slight change in the intensity ratio between the SiO_2 and $MnSiO_3$ component peaks in both spectra. Based on these results it is suggested that the presence of Ru facilitates the dissociation of $MnSiO_3$ following 500 °C annealing, impacting upon the thermodynamic stability of the barrier layers. However, it should be noted that the extent of Mn metal formation seen following $MnSiO_3$ dissociation seen in Figure 5.7 is considerably less than that seen following MnO

dissociation in Figure 5.2 and Figure 5.5. As such, it may be suggested that while the presence of Ru impacts upon the chemical composition of both MnO and $MnSiO_3$, the $MnSiO_3$ barrier layer has comparatively higher thermodynamic stability in the presence of Ru liner layers.

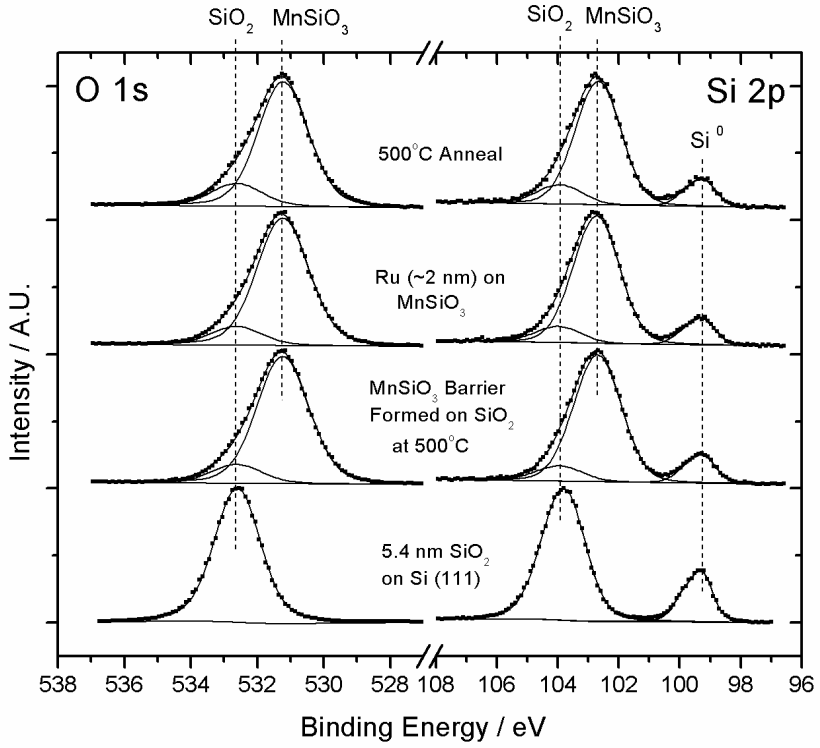

Figure 5.6 Normalised and curve fitted O 1s and Si 2p XPS spectra showing the interaction of Ru (~2 nm) with a single phase $MnSiO_3$ barrier layer (~5 nm). (BE positions in O 1s – SiO_2 = 532.8 eV, $MnSiO_3$ = 531.5 eV; BE positions in Si 2p – SiO_2 = 103.8 eV, $MnSiO_3$ = 102.2 eV, Si^0 = 99.3 eV). All peak fitting parameters included in Appendix A.

Based on the results of the three separate experiments performed in this study it can be stated that Ru acts to change the chemical composition of both $MnSiO_3$ and MnO barrier layers by reducing the dissociation energy of

Mn-O bonds and reducing the O desorption energy on these surfaces. Therefore, it is suggested that these conductive liner layers are not chemically inert at the liner/barrier interface, a result which may have significant implications on the use of Ru/Mn based barrier layers. In particular, the dissociation of both MnO and $MnSiO_3$ in the presence of Ru may act to degrade the Cu diffusion barrier properties of these layers which is of significant importance given that the physical thickness of the barrier layer will need to be reduced to below 2 nm for the 16 nm technology node.[21] Furthermore, the upward diffusion of O released from the barrier layer during this dissociation process may also impact upon the resistivity of the overlying Cu interconnect.

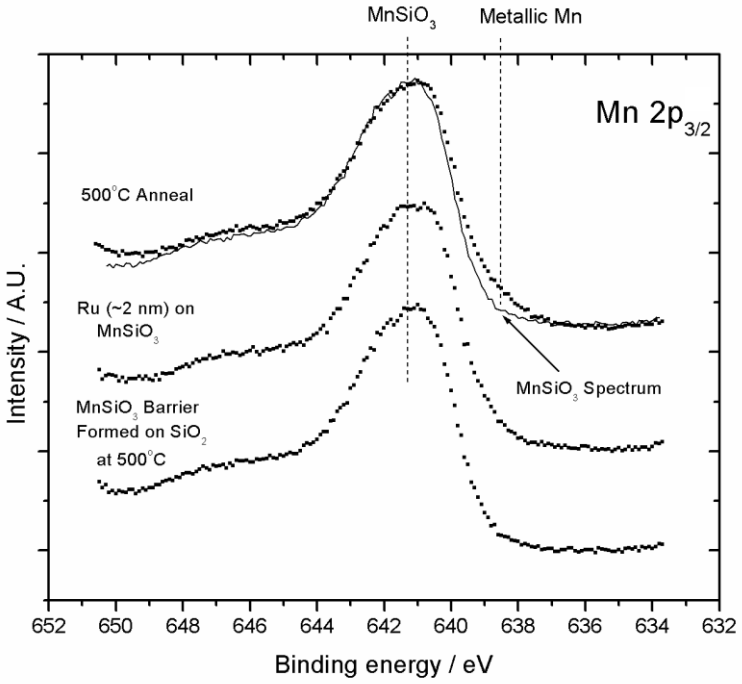

Figure 5.7 Normalised and non-curve fitted Mn $2p_{3/2}$ XPS spectra corresponding to Figure 5.5. The Mn $2p_{3/2}$ spectrum taken following 500 °C annealing in the presence of Ru has been overlaid with the Mn $2p_{3/2}$ spectrum taken from the $MnSiO_3$ barrier layer (solid line) in order to clearly show the formation of metallic Mn in the absence of relevant curve fitting parameters. (BE positions in Mn 2p; metallic Mn = 638.1 eV, $MnSiO_3$ = 641.1 eV).

5.5 Conclusions

In the first section of this chapter the catalytic activity of bimetallic Ru/Mn surfaces towards O_2 was investigated using a fully in-situ UHV experimental procedure, for the first time within the literature. XPS analysis performed following a controlled UHV O_2 exposure of 180 L showed that O_2 is dissociatively chemisorbed on the Ru/Mn surface to form MnO. Subsequent thermal annealing resulted in the dissociation of MnO as evidenced by the formation of metallic Mn along with evidence for the desorption of O from the Ru/Mn surface. The dissociation of MnO at this temperature is in contrast to results taken from MnO control samples and as such it is suggested that the presence of Ru catalytically reduces the dissociation energy of MnO and the oxygen desorption energy. XPS spectra show no evidence of chemical changes in the Ru 3d spectra as a function of MnO dissociation, offering experimental evidence in agreement with the proposed mechanism for O catalysis on bimetallic surfaces. The second section of this chapter investigated the impact of Ru catalysis on the chemical composition and thermodynamic stability of preformed Mn-O based Cu diffusion barrier layers. It has been shown that the presence of Ru liner layers results in the partial dissociation of both MnO and $MnSiO_3$ barrier layers on SiO_2 surfaces following a 500 °C thermal anneal. This result is again attributed to the catalytic activity of Ru/Mn surfaces reducing the dissociation energy of Mn-O bonds within the barrier layer region. It

should be noted that the thermodynamic stability of the $MnSiO_3$ layers in the presence of Ru was higher than that of the MnO layers.

5.6 References

[1]Otero, R.; Calleja, F.; Garcıa-Suarez, V.M.; Hinarejos, J.J.; de la Figuera, J.; Ferrer, J.; Vazquez de Parga, A.L.; Miranda, R.; Tailoring Surface Electronic States Via Strain

to Control Adsorption :O/Cu/Ru(0001) *Surf. Sci.*, ***550***, 65-72 (2004)

[2]Mavrikakis, M.; Hammer, B.; Nørskov J.K.; Effect of Strain on the Reactivity of Metal Surfaces, *Phys. Rev. Letts.* ***81***, 13, 2819-2822 (1998)

[3]Nørskov, J. K.; Bligaard, T.; Rossmeisl, J.; Christensen, C.H.; Towards the computational design of solid catalysts, *Nat. Chem.* ***1***, 37-46 (2009)

[4]Lu, C.; Lee, I.C.; Masel, R.I.; Wieckowski, A.; Rice, C.; Correlations between the heat of adsorption and the position of the center of the d-band: differences between computation and experiment, *J. Phys. Chem. A*, ***106***, 3084-3091 (2002)

[5]Lee, Y.-L.; Kleis, J.; Rossmeisl, J.; Shao-Horn, Y.; Morgan, D.; Prediction of solid oxide fuel cell cathode activity with first-principles descriptors, *Energy Environ. Sci.*, ***4***, 3966-3970 (2011)

[6]Hofmann, T.; Yu, T.H.; Folse, M.; Weinhardt, L.; Bär, M.; Zhang, Y.; Merinov, B.V.; Myers, D.J.; Goddard, W.A.; Heske, C.; Using Photoelectron Spectroscopy and Quantum Mechanics to Determine d-Band Energies of Metals for Catalytic Applications, *J. Phys. Chem. C*, ***116***, 24016-24026 (2012)

[7]Deng, X.; Koun Min, B.; Guloy, A.; Friend, C. M.; Enhancement of O_2 Dissociation on Au (111) by Adsorbed Oxygen: Implications for Oxidation Catalysis, *J. Am. Chem. Soc*. ***127***, 9267-9270 (2005)

[8]Lescop, B.; Initial oxidation of Mn surface studied by ultraviolet photoelectron spectroscopy and metastable induced electron spectroscopy *Appl. Surf. Sci*. ***252***, 2276-2280 (2006)

[9]Ji, H. B.; Ebitani, K.; Mizugaki, T.; Kaneda, K.; Environmentally friendly alcohol oxidation using heterogeneous catalyst in the presence of air at room temperature, *Catalysis Communications* ***3***, 511-517 (2002)

[10]Monteiro, N.K.; Noronha, F.B.; da Costa, L.O.O.; Linardi, M.; Fonseca, F.C.; A direct ethanol anode for solid oxide fuel cell based on a chromite-manganite with catalytic ruthenium nanoparticles, *Int. J. Hydrogen Energy* ***37***, 9816-9829 (2012)

[11]Casey, P.; Bogan, J.; Lozano, J. G.; Nellist, P. D.; Hughes, G.; Chemical and structural investigation of the role of both Mn and Mn oxide in the formation of manganese silicate barrier layers on SiO_2, *J. Appl. Phys.* ***110***, 054507-054507-6 (2011)

[12]Seah, M.P.; Spencer, S.J.; Ultrathin SiO2 on Si II. Issues in Quantification of the Oxide Thickness, *Surf. Interface Anal.* ***33***, 640-652 (2002)

[13]Nesbitt, H.W.; Banerjee, D.; Interpretation of XPS Mn (2p) spectra of Mn oxyhydroxides and constraints on the mechanism of MnO2 precipitation *American Mineralogist* ***83***, 305-315 (1998)

[14]Wojcik, H.; Krien, C.; Merkel, U.; Bartha, J.W.; Knaut, M.; Geidel, M.; Adolphi, B.; Neumann, V.; Wenzel, C.; Bendlin, M.; et al.; Characterization of Ru–Mn composites for ULSI interconnects, *Microelectronic Engineering*; **112,** 103-109 (2013)

[15]Audi, A.A.; Sherwood, P. M. A.; Valence-band x-ray Photoelectron Spectroscopic Studies of Manganese and its Oxides Interpreted by Cluster and Band Structure Calculations, *Surf. Interface Anal.* ***33***, 274-282 (2002)

[16]Lescop, B.; Initial oxidation of Mn surface studied by ultraviolet photoelectron spectroscopy and metastable induced electron spectroscopy *Appl. Surf. Sci*. ***252***, 2276-2280 (2006)

[17]Nørskov, J. K.; Bligaard, T.; Rossmeisl, J.; Christensen, C.H.; Towards the computational design of solid catalysts, *Nat. Chem.* ***1***, 37-46 (2009)

[18]Casey, P.; Bogan, J.; Brennan, B.; Hughes, G.; Synchrotron radiation photoemission study of in-situ manganese silicate formation on SiO2 for barrier layer applications, *Appl. Phys. Lett.* ***98***, 113508-113508-6 (2011)

[19]Iwata, S.; Ishizaka, A.; Electron Spectroscopic Analysis of the SiO_2/Si System and Correlation with Metal–Oxide–Semiconductor Device Characteristics *J. Appl. Phys.* ***79***, 6653-6653-5 (1996)

[20]Ofner. H.; Hofmann. R; Kraft. J.; Netzer. F.P.; Paggel, J.J.; Horn, K.; Metal-Overlayer-Induced Charge-Transfer Effects in Thin SiO_2-Si Structures, *Phys. Rev. B.* ***50***, 15120-15125 (1994)

[21]*International Technology Roadmap for Semiconductors*, Interconnect edition, 2010.

Chapter 6

Photoemission studies of silicon referencing, chemical modification of carbon doped oxide surfaces for Mn-silicate formation, and Ru interactions on low-κ surfaces

6.1 Introduction

While the majority of studies to date have focused on the formation of $MnSiO_3$ barrier layers on SiO_2 surfaces,[1-5] the growth of Mn-based barrier layers on ultralow dielectric constant (ULK) materials has also been the subject of some interest.[6-11] ULK materials are being developed in an effort to address resistance-capacitance (RC) delay problems associated with current dielectrics.[9] The introduction of carbon into SiO_2 in the form of Si-CH_3 bonds, forms the basis for one dielectric material system thought to be most compatible with modern device fabrication processes. The reduced polarity of this bonding structure and the introduction of voids within the carbon doped oxide (CDO), acts to reduce the dielectric constant of the substrate, thereby improving the RC time delay of the interconnect. The formation of barrier layers on these surfaces is essential if they are to be adopted by the industry. It will be shown in section 6.3 of this chapter that the chemical identification of Mn-silicate by XPS on CDO dielectric materials is extremely difficult as the binding energy positions of the

oxidised Si 2p in $MnSiO_3$ and in CDO are almost identical (~103.3 eV). As such, alternative identification methods of $MnSiO_3$ on these surfaces will be investigated. In section 6.4 of this chapter the surface modification of CDO substrates by oxygen treatment will be analysed as a means of altering the chemical environment of the surface for the subsequent formation of Mn-based barrier layers. Finally, section 6.5 investigates the chemical interactions of deposited Ru with Mn-based barrier layers on industrially relevant carbon doped oxide dielectric surfaces.

6.2 Experimental details

The CDO samples studied in this work varied in carbon content from 14% to 48% and were degassed up to ~300 °C for 4 hours following insertion into the UHV chamber of base pressure ~1 x 10^{-9} mbar. The samples had no associated porosity. Atomic oxygen was used to treat the surface of the CDO samples by passing molecular oxygen through a cracker at 60 V. Hydrochloric acid (HCL) etched Mn chips (~99.9% purity) were used as a source material for the deposition of Mn thin films using an Oxford Applied Research EGC04 mini electron-beam evaporator. The chamber pressure during Mn deposition was 1 x 10^{-8} mbar. Fully oxidised Mn-oxide thin films were deposited through the simultaneous deposition of Mn in an O_2 partial pressure of ~5 × 10^{-8} mbar. Room temperature e-beam evaporation of silicon was performed using a Si source material of 99.9 % purity, at a

deposition pressure of ~5 × 10^{-9} mbar. The XPS analysis was carried out using a VG Microtech electron spectrometer at a base pressure of ~1 × 10^{-9} mbar as described in section 3.2. The XPS core level spectra of the O 1s, Si 2p and C 1s were curve fitted using Voigt profiles composed of Gaussian and Lorentzian line shapes in a 3:1 ratio and using a Shirley-Sherwood type background. The full width at half maximum (FWHM) of the Si 2p CDO substrate peaks varied between 1.4 eV and 1.8 eV, with a Mn-silicate component peak of 1.5 eV. The FWHM of the O 1s CDO component was 1.5 eV with Mn-silicate and Mn-oxide peaks in the range of 1.4 eV to 1.6 eV. The FWHM of the C 1s CDO component was 1.3 eV with a Mn-carbide peak of 1.2 eV. The FWHM of the Si 2p bulk peak was 0.9 eV, with SiO_2 and Mn-silicate component peaks in the range 1.1 eV to 1.2 eV. The FWHM of the O 1s SiO_2 component was 1.2 eV with Mn silicate and Mn oxide peaks in the range of 1.1 eV to 1.2 eV. All curve fitting analysis presented in this study was performed using AAnalyzer curve fitting software program. It should be noted that curve fitting of the Mn 2p spectrum could not be performed given that XPS ghost peaks emanating from the Mn $2p_{1/2}$ are present within the peak profile of the Mn $2p_{3/2}$ component. As such, only non-curve fitted Mn 2p spectra are included in this study. As outlined in section 3.3 the Mn 2p spectra shown in this study are primarily used to identify the presence of oxidised Mn species on the sample surface, with the O 1s and Si 2p spectra used to conclusively

identify the presence of differing oxidised Mn species such as Mn-silicate and Mn-oxide.

6.3 Photoemission study of Si referencing of carbon doped oxide materials

Electrically insulating materials are prone to surface charging during XPS measurements. The mechanism for this charging effect involves the accumulation of a positive charge on the surface of the sample as a result of x-ray irradiation, which acts to reduce the kinetic energy of emitted photoelectrons. As a result, the observed peaks in spectra obtained from such samples appear at higher binding energy positions than they would in the absence of sample charging. Traditionally, a low energy electron flood gun is used to replace emitted electrons and reduce surface charging effects. A slight overcompensation is normally used, setting up an equilibrium state with peaks in the spectrum shifted to lower binding energy. The peaks are then subsequently shifted back to a set internal standard such as adventitious carbon or a known species in that particular sample. However, in the case of CDO the C1s spectra cannot be used as an internal reference as the carbon within the substrates may be in one or more different chemical states. As such, the precise binding energy positions of materials in CDO substrates are difficult to accurately determine. In this section, XPS is used to systematically investigate a number of CDO substrates of varying carbon content and porosity. In situ e-beam evaporation of Si and Mn-oxide is

utilized to chemically reference the binding energy positions of the Si 2p and O 1s core level spectra for the various CDO substrates. Following the completion of chemical referencing studies, the same set of CDO samples were used as substrates for the subsequent deposition and attempted formation of Mn-based barrier layers.

Figure 6.1 shows the Si 2p spectra after the deposition of Si from the e-beam evaporator on four different carbon doped oxide surfaces of varying carbon content. The Si was deposited in order to accurately determine the binding energy positions of the Si 2p for each of the dielectric materials. As stated, surface charging on insulating substrates such as CDO surfaces poses a problem when attempting to determine the binding energy positions of the emergent peaks. As the binding energy position of Si^0 is well known, it acts as an ideal reference material to establish the peak positions of the different carbon content CDO substrates. Fixing the BE position of the deposited Si^0 peak to the well known BE position of 99.3 eV in Figure 6.1 indicates the Si 2p substrate peak systematically decreases in BE with increasing carbon content consistent with a reduction in the dielectric polarity. The highest carbon content 'CDO 48' Si 2p peak emerges at a binding energy position of ~1.5 eV closer to the Si^0 peak than that of a reference SiO_2 layer. It should be noted that although the CDO Si 2p spectra are fitted with one peak, it is likely there are multiple overlapping peaks representing the

different chemical environments of the substrate Si. The CDO samples used in these experiments were acquired externally and as such the exact bonding structure is unknown. Table 6.1 shows the carbon content, Si 2p and O 1s binding energy positions obtained from the four CDO substrates after Si referencing.

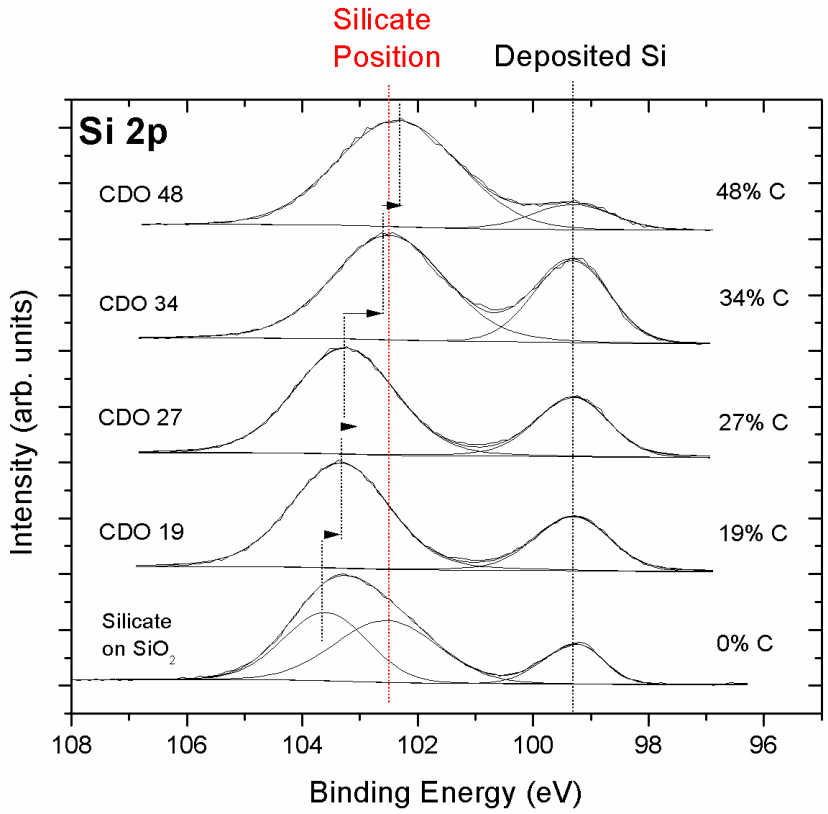

Figure 6.1 Si 2p spectra taken from Si deposited on multiple carbon doped oxide surfaces showing substrate shift to LBE with increasing carbon content. Silicate was formed on SiO_2 by depositing ~1 nm Mn on SiO_2 followed by an anneal at 400 ^{o}C. (BE positions in Si 2p – deposited Si = 99.3 eV, Mn-Silicate = 102.3 eV, CDO 19 = 103.3 eV, CDO 27 = 103.2 eV, CDO 34 = 102.5 eV, CDO 48 = 102.4 eV). All peak fitting parameters included in Appendix A.

Substrate	%C	Si 2p B.E (eV)	O 1s B.E (eV)
CDO 8	8%	103.42	532.81
CDO 14	14%	103.64	532.53
CDO 19 (Black diamond 2)	19%	103.34	532.47
CDO 34	34%	102.52	532.22
CDO 48	48%	102.38	532.13

Table 6.1 Si 2p and O 1s binding energy referencing for various carbon doped oxide substrates.

For direct comparison, Figure 6.2 shows the Si 2p spectra of the highest carbon content 'CDO 48', $MnSiO_3$ and SiO_2. It can be clearly seen that the binding energy position of the 'CDO 48' (~102.38 eV) is almost indistinguishable from that of $MnSiO_3$. The proximity of CDO Si 2p peaks to $MnSiO_3$ makes the identification of $MnSiO_3$ on these substrates very difficult to identify using this peak due to the resolution limits imposed by non-monochromated XPS. In previous studies the Si 2p peak was the

primary identifier of $MnSiO_3$, however as this peak is no longer useful in this regard, an attempt was made to use the binding energy positions of the O 1s and the Mn 2p core levels to identify the presence of silicate.

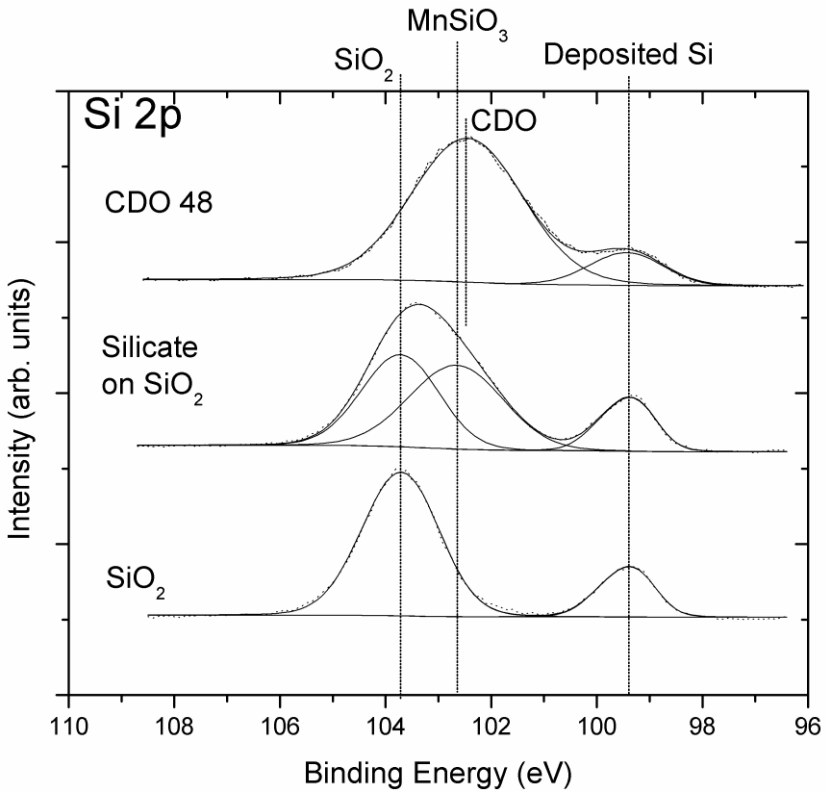

Figure 6.2 Curve fitted Si 2p spectra taken from 5 nm SiO_2, $MnSiO_3$ on 5 nm SiO_2 and as received 'CDO 48' highlighting the difficulty in confirming silicate formation on a high carbon content CDO surface. (BE positions in Si 2p – deposited Si = 99.3 eV, SiO_2 = 103.8 eV, Mn-Silicate = 102.3 eV, CDO 48 = 102.4 eV). All peak fitting parameters included in Appendix A.

Figure 6.3 shows the O 1s spectra for the four different CDO substrates after the controlled deposition of ~2 nm of MnO. The fully oxidised nature of the deposited MnO film on the different CDO's is apparent from the Mn 2p

spectra shown in Figure 6.4. As such, the MnO deposition enables binding energy referencing of the O 1s signal emerging from the dielectric substrate. It can be seen that the O 1s substrate peak appears at LBE with increasing carbon content, an effect also seen in the Si 2p as previosuly stated. The appearance of a small peak situated between the MnO and CDO O 1s peaks should be noted, providing limited evidence for the growth of Mn-silicate. Although this additional peak is in the correct region for Mn-silicate, stronger evidence would be required to conclusively determine the presence of this chemical state.

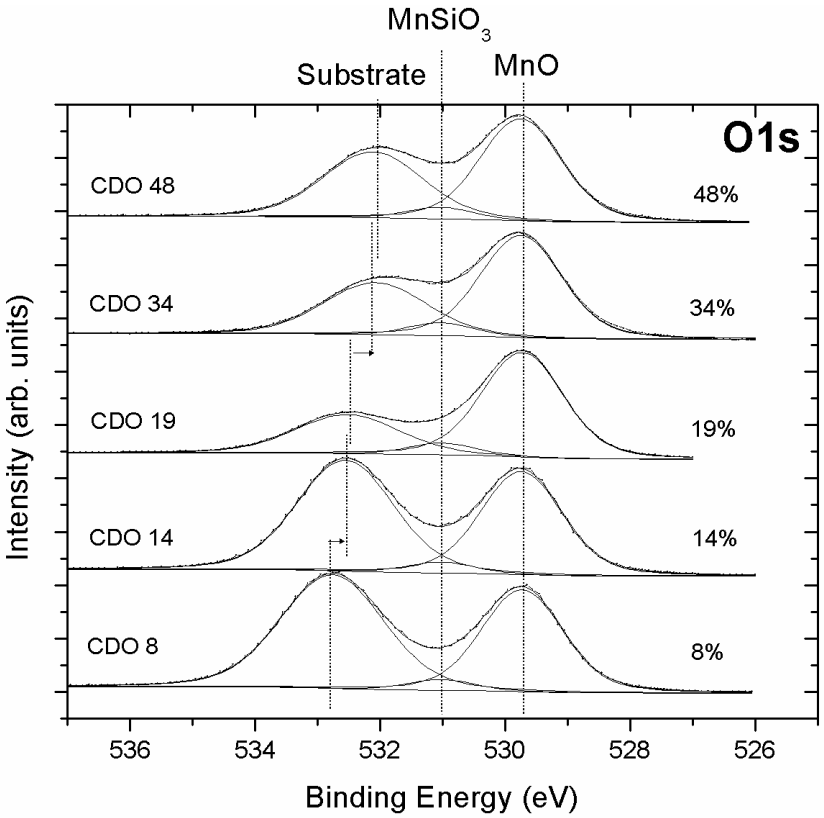

Figure 6.3 Curve fitted O 1s spectra taken from MnO deposited on multiple carbon doped oxide surfaces showing a similar shift to LBE with increasing carbon content as observed in

Figure 6.1. There is a 1.2 eV binding energy separation between MnO and $MnSiO_3$. Binding energy positions outlined in table 6.1.

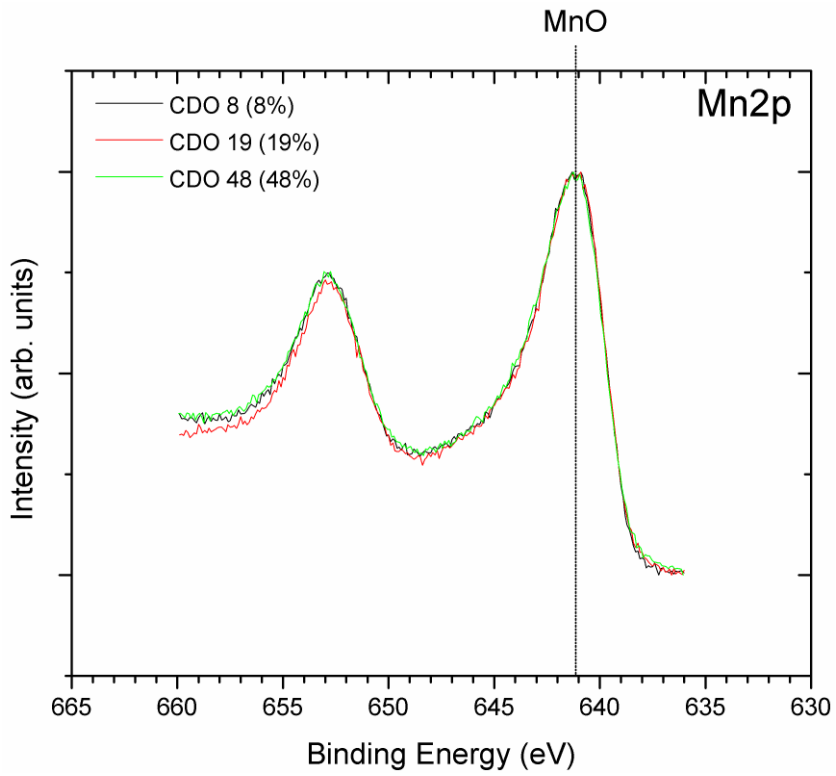

Figure 6.4 Mn 2p spectra of Mn oxide deposited on various substrates. Spectra show the reproducibility of deposited Mn oxide across multiple samples and can be used as a chemical reference within O 1s spectra. (BE position in Mn 2p MnO peak = 641.1 eV)

Previous studies have shown that the growth of Mn-silicate on Si based oxides require thermal treatment after the deposition of Mn. Figure 6.5 shows the O 1s spectra for ~2 nm of MnO deposited on SiO_2 followed by subsequent annealing to 400 ^{o}C for 1 hour. The growth of a significant peak 1.38 eV on the HBE side of the MnO peak is identified as $MnSiO_3$, which is

supported by a concurrent peak in the Si 2p (not shown). This separation of 1.38 eV between the known MnO peak and $MnSiO_3$ provides a good reference for identifying $MnSiO_3$ on the various CDO substrates. Figure 6.6 shows the four ~2 nm MnO/CDO samples mentioned above following thermal annealing treatment at 400 ^oC for 1 hour. As in the MnO/SiO_2 system, there is clear evidence for the growth of a peak between the CDO substrate and the deposited MnO layer. The same fitting parameters and binding energy separations were used in all cases strongly suggesting that the additional peak emerges from $MnSiO_3$ on all of the CDO surfaces.

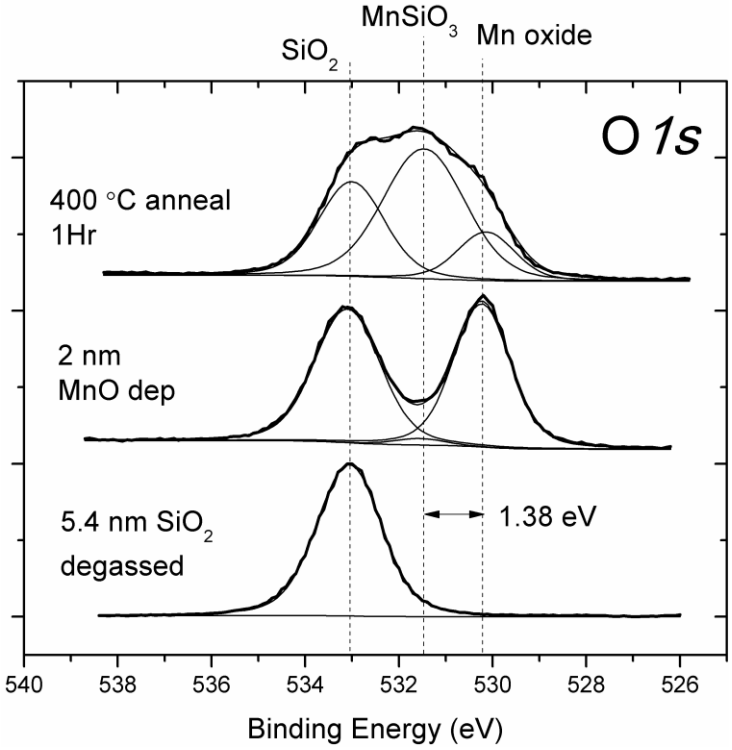

Figure 6.5 Curve fitted O 1s spectra showing Mn silicate growth on SiO_2 after thermal anneal. (BE positions in O 1s – Mn-oxide = 530.1 eV, $MnSiO_3$ = 531.5 eV, SiO_2 = 533.0 eV). All peak fitting parameters included in Appendix A.

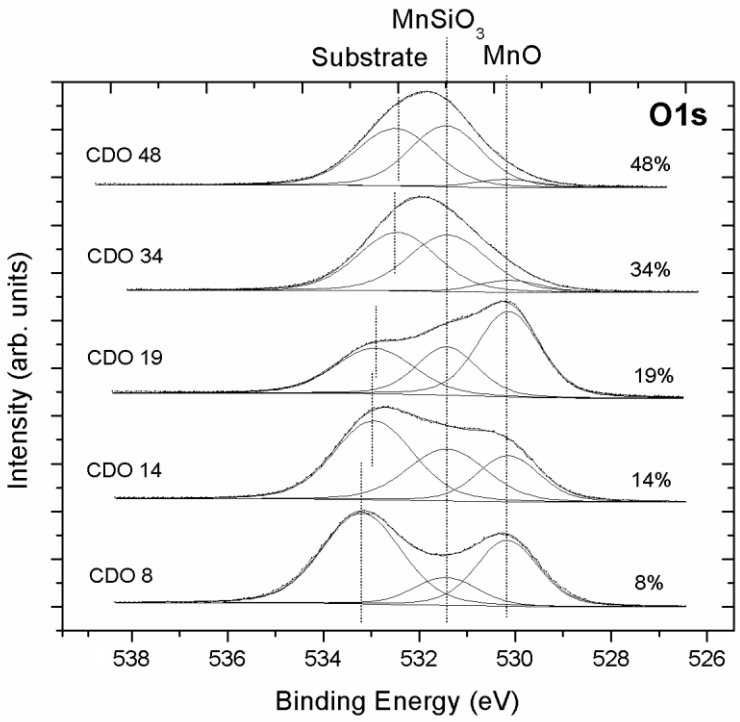

Figure 6.6 Curve fitted O1s spectra highlighting possible Mn-silicate formation on CDO substrates of varying carbon content after 400 ^{o}C anneal. (BE positions in O 1s – MnO = 530.1 eV, $MnSiO_3$ = 531.5 eV, CDO 8 = 533.2 eV, CDO 14 = 532.5 eV, CDO 19 = 532.5 eV, CDO 34 = 532.2 eV, CDO 48 = 532.1 eV. All peak fitting parameters included in Appendix A.

The Mn 2p spectra shown in Figure 6.7 indicates the difference in peak profile between MnO and $MnSiO_3$. The presence of a feature at ~647 eV is indicative of $MnSiO_3$, which was obtained from the well established $MnSiO_3$ phase on a reference SiO_2 sample. The same 'silicate identifying' feature appears on all the MnO/CDO samples after 400 ^{o}C. Although Mn-silicate cannot be identified from the Si 2p on CDO substrates, careful analyses of the both O 1s and Mn 2p provides an alternative method of

identification. It should also be noted that throughout the course of all experiments the C 1s spectra shows very little evidence for Mn-carbide formation, as seen in Figure 6.8. This is in agreement with previous studies which used MnO to minimize carbide formation on CDO substrates.[14] The inability to analyse the Si 2p spectra for these chemical interactions makes it difficult to definitively state that silicate formation is occurring. However, there is sufficient evidence to warrant further investigation by complementary characterization techniques which have the capability to uniquely identify compound formation such as EXAFS.

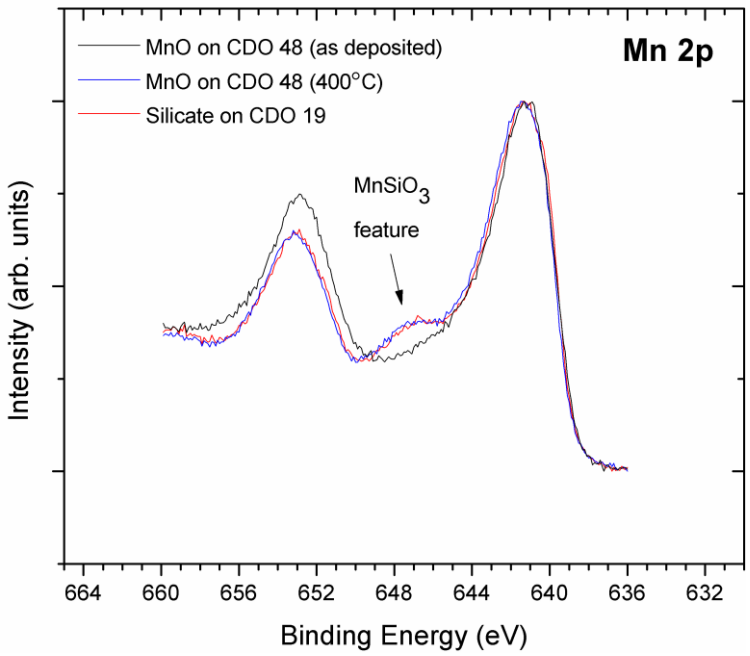

Figure 6.7 Mn 2p spectra highlighting possible silicate formation on high carbon content CDO. Mn 2p spectra comparing Mn silicate growth on SiO_2 with possible silicate formation on high carbon content CDO.

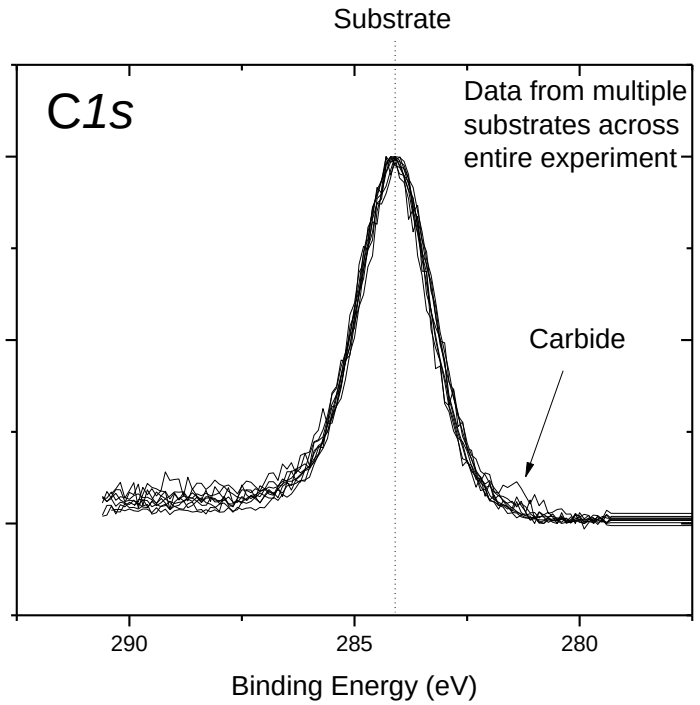

Figure 6.8 C 1s spectra taken all studied samples showing little evidence of Mn carbide formation.

6.4 Oxygen modification of carbon doped oxide surfaces for Mn-silicate barrier formation

It has been shown by Casey et al. that the formation of a Mn-based barrier layer on a CDO dielectric substrate can result in the formation of Mn-carbide species due to the presence of carbon at the surface.[10] The presence of Mn-carbide in the barrier layer region is undesirable as it complicates the interface chemistry and acts as a source of uncertainty. As such, a dielectric surface with minimal carbon provides a more suitable substrate for the subsequent formation of a Mn-based barrier layer – limiting the production

of Mn-carbide. Additionally, the removal of carbon by oxygen treatment has the added benefit of providing increased surface oxygen to facilitate the growth of $MnSiO_3$. It has been shown in section 6.3 that the chemical identification of Mn-silicate by XPS on CDO dielectric materials is extremely difficult as the binding energy positions of the Si 2p for $MnSiO_3$ and CDO are almost identical (~103.3 eV). As such, the Si 2p peaks for both CDO and Mn-silicate cannot be devolved by conventional peak fitting analysis and therefore the presence of Mn-silicate cannot be conclusively determined on this substrate. Another benefit of removing carbon and adding oxygen to the CDO dielectric surface is that Si in a more oxygen rich environment has a HBE Si 2p peak than that of Si in a carbon environment. As such, the Si 2p signal emerging from a modified 'oxygen rich' CDO surface will have a shifted binding energy position to that of the untreated surface thereby increasing the binding energy separation between the $MnSiO_3$ and the substrate. The advantage of this process is that the $MnSiO_3$ could then be identified by XPS as the peaks are sufficiently resolvable. This study will aim to address two core issues associated with the formation of $MnSiO_3$ on CDO surfaces; (1) Investigate the potential of cracked oxygen treatment to reduce the surface carbon content while minimising the damage caused to the dielectric material (2) To ascertain the potential for a modified CDO surface to facilitate the identification of $MnSiO_3$ by XPS. It should also be noted that the reduction of carbon from dielectric surfaces has been

performed by other methods such as oxygen plasma treatment, however significant damage to the dielectric has been reported resulting in the degradation of the dielectric constant of the material. The cracked oxygen treatment used in this study is much less reactive than plasma treatments thereby limiting any carbon reduction to the surface of the substrate and maintaining the dielectric integrity.[11]

The XPS survey scans shown in Figure 6.9 indicate the change in relative elemental concentrations at the carbon doped oxide dielectric surface as a result of increasing exposure to cracked oxygen. The precise concentrations of Si, C and O were calculated using the integrated area of the Si 2p, C 1s and O 1s XPS peaks respectively. It can be seen that the carbon concentration of the CDO 48 sample was reduced from 44% to 29% after exposure to ~5400 Langmuir of cracked O_2. Additionally, a significant increase in the surface O signal (36% to 59%) was also evident suggesting that O effectively replaced C at the surface.

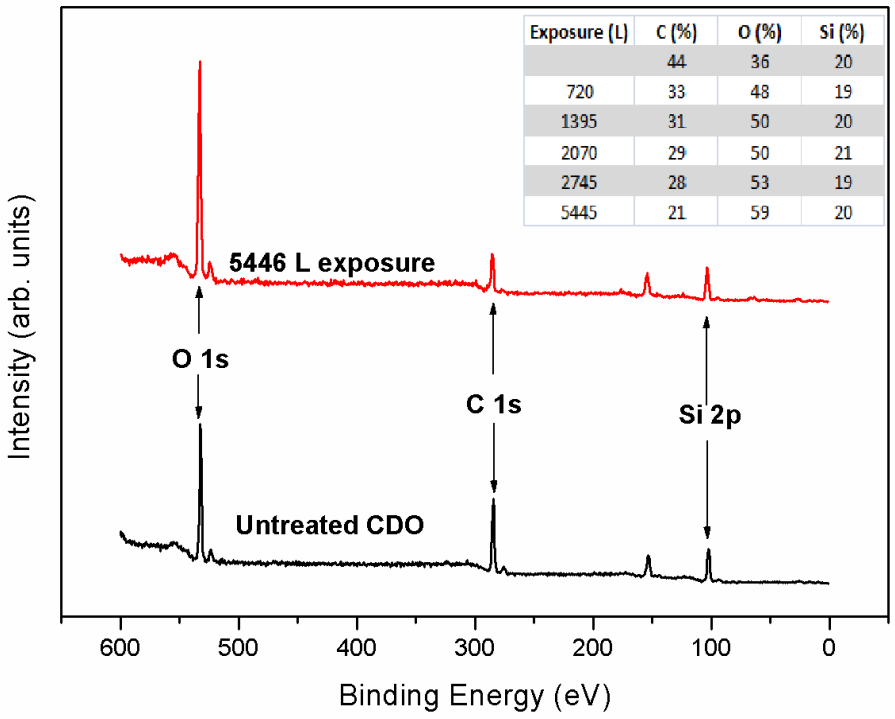

Figure 6.9 XPS survey scans taken from the CDO 48 surface before and after exposure to cracked oxygen, showing the systematic reduction in surface carbon.

It should be noted that although the relative concentration of Si remained constant throughout the experiment, the position of the Si 2p peak appears to shift to HBE as seen in Figure 6.10, which is consistent with a change in the chemical environment of the Si at the surface. The native CDO 48 Si 2p peak consists of contributions from a combination of Si-O and Si-C bonds. As the electronegativity of O is higher than that of C, Si in an oxygen environment will tend to appear at higher binding energy than Si in a carbon containing environment. As such, the chemical shift of the Si 2p to HBE is

consistent with the increased presence of oxygen at the surface. It should be noted that the most oxygen rich environment that Si can attain is that of SiO_2 which has a Si 2p binding energy position of 104.3 eV. The O 1s spectra seen in Figure 6.10 also shifts to HBE as a function of exposure to atomic ogygen.

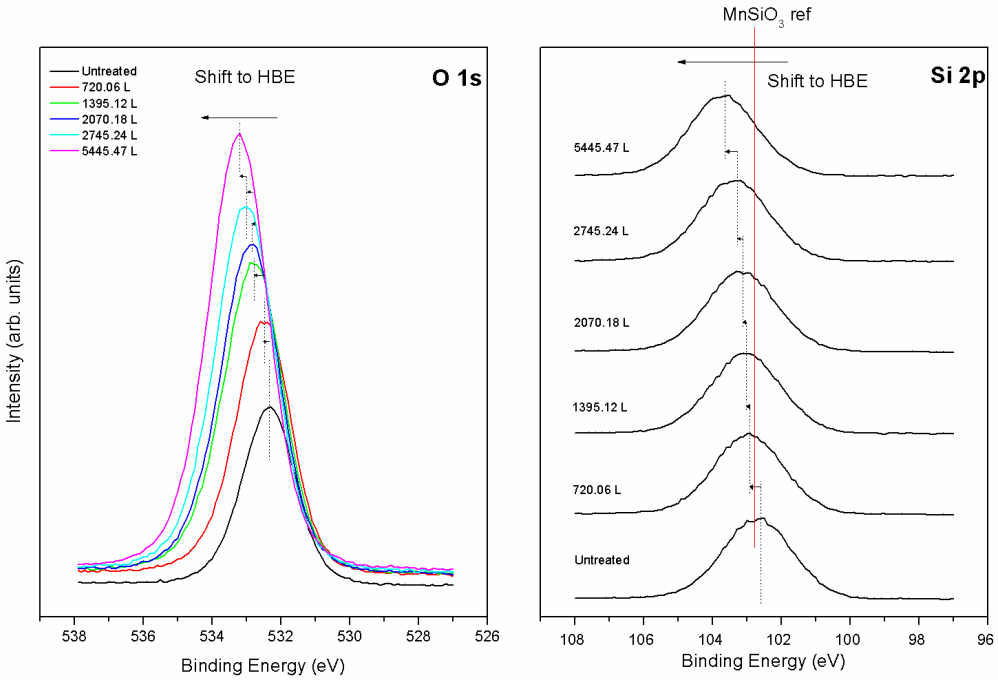

Figure 6.10 The evolution of the O 1s and Si 2p peaks as a result of increasing exposure to cracked oxygen on CDO 48. Both peaks chemically shift to higher binding energy as the surface carbon content is reduced. Binding energy of Si 2p shifts from 102.7 eV in the untreated sample to 103.5 eV after 5445.47L of exposure. Binding energy of O 1s shifts from 532.2 eV in the untreated sample to 533.1 eV after 5445.47L of exposure.

Following the final atomic oxygen exposure, approximately ~1 nm of Mn was deposited by e-beam evaporation on the modified CDO 48 surface and the Mn/CDO structure was subsequently annealed to 400 ^{o}C. It can be seen

from the O 1s spectra in Figure 6.11 that a limited amount of Mn-oxide was present on the surface upon deposition evidenced by a peak at a binding energy position of 530 eV.[1] The growth of additional peaks on the LBE side of both the O 1s and oxidised Si 2p bulk signals as a result of thermal annealing can be seen at binding energy positions of 531.5 eV and 102.3 eV, respectively. The concurrent growth of peaks at these binding energy positions have previously been attributed to evidence of the formation of $MnSiO_3$.[1] The appearance of distinct $MnSiO_3$ peaks on the modified CDO 48 surface are in contrast to the results presented in section 6.3 which suggested that $MnSiO_3$ may form on the untreated surface, but cannot be identified as a result of overlapping peaks as illustrated by the untreated CDO 48 reference peak marked in Figure 6.11. The atomic oxygen modification in this study has 'moved' the substrate peaks sufficiently to allow identification of a $MnSiO_3$ phase in the Si 2p peak profile. Angular resolved spectra with a take off angle of 45^o reveal the surface localised nature of the Mn-silicate with respect to the CDO substrate.

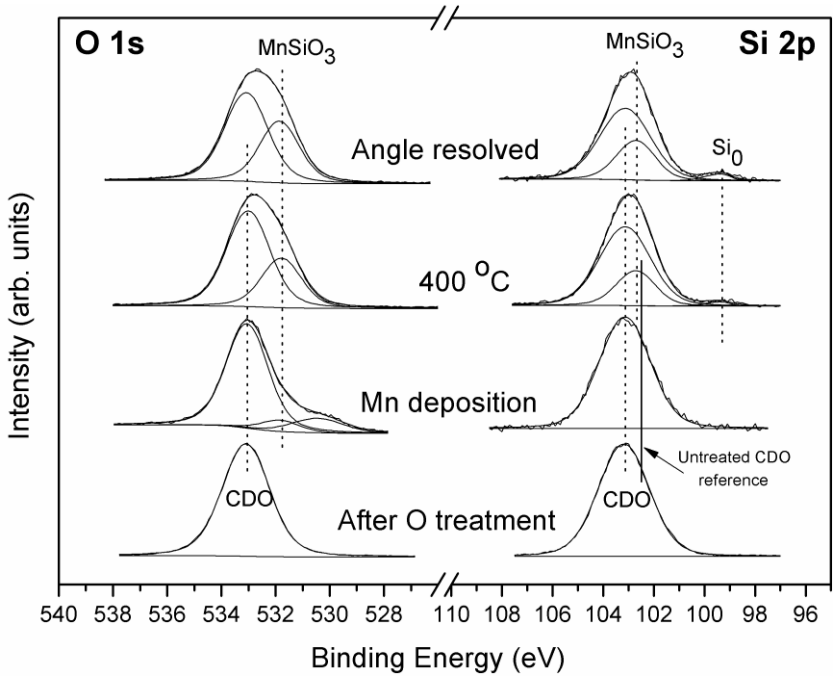

Figure 6.11 O 1s and Si 2p peaks identifying the growth of $MnSiO_3$ on the modified CDO 48 dielectric surface. (BE positions in O 1s – $MnSiO_3$ = 531.5 eV) All peak fitting parameters included in Appendix A. Angle resolved scans taken at 45°.

Figure 6.12 shows the C 1s and Mn 2p spectra from the modified CDO 48 substrate before and after Mn deposition and the subsequent formation of the $MnSiO_3$ layer. The growth of an additional peak on the LBE side of the C 1s provides strong evidence for the formation of a limited quantity of Mn-carbide as a result of the presence of residual surface carbon. Although the carbon content was significantly reduced by the oxygen treatment process, it was not completely removed. As such, the formation of Mn-carbide in this manner is to be expected and has been reported previously.[12] It should be noted that the formation of Mn-carbide on CDO surfaces can be

significantly reduced by the deposition of oxidized Mn instead of metal Mn.[12]

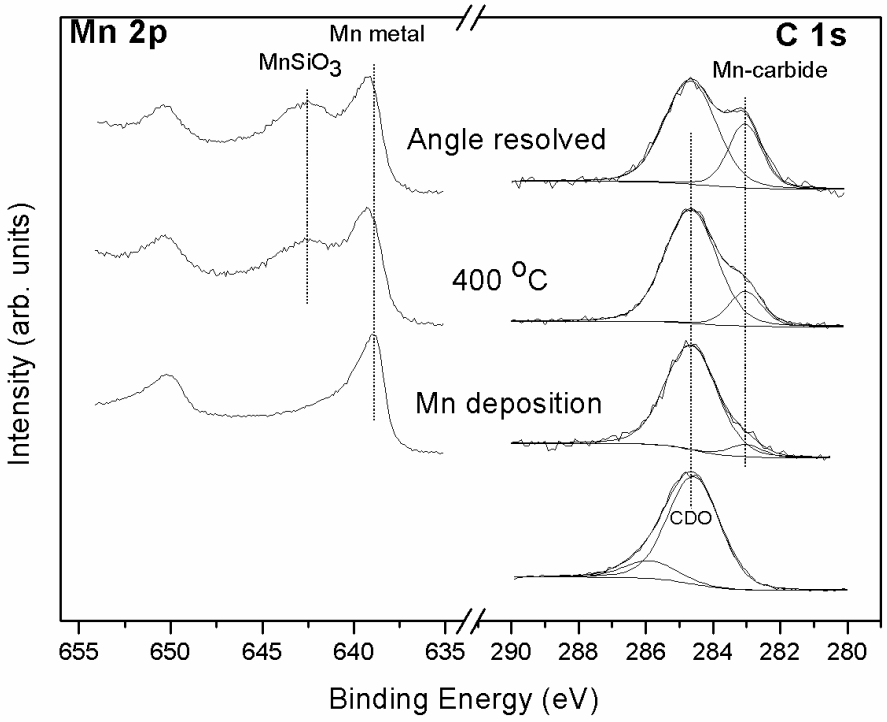

Figure 6.12 C 1s and Mn 2p peaks showing the growth of a limited quantity of Mn-carbide on CDO 48 after the deposition of MnO and subsequent annealing. Angular resolved spectra also shown at 45^{o} to normal emission increasing surface sensitivity.

6.5 Chemical investigations of Ru interactions with Mn based barrier layers and carbon doped oxide dielectrics

The focus of this section is to investigate the chemical interactions of Ru on Mn-based barrier layers on both CDO 34 and CDO 48. The depth sensitivity of the XPS exceeds the thickness of the deposited layers allowing signals from the dielectric substrate to be detected. This ability to detect XPS signals from the dielectric substrate provides an internal chemical reference for the subsequent deposition of metal layers. However, the BE position of the strongest Ru peak (Ru 3d) overlaps that of the substrate carbon peak complicating the devolution of the C 1s from the CDO and Ru 3d spectra. As such, it was necessary to initially analyse the C 1s and Ru 3d peaks in the absence of Mn in order to accurately determine their relative peak positions. Approximately ~1 nm of Ru was deposited by in-situ e-beam evaporation directly on the two different carbon doped oxide (CDO) substrates in a UHV environment of base partial pressure of ~$1x10^{-9}$ mbar and the associated C 1s and Ru 3d core spectra are shown in Figure 6.13. It can be seen from Figure 6.13 that the C 1s and Ru $3d_{3/2}$ peaks from the CDO substrate and the deposited Ru layer, respectively, overlap making the spectra difficult to resolve. The fitting parameters for the C 1s peaks were acquired from the CDO substrates before the deposition of Ru and remained locked throughout the experiment with a FWHM value of 1.3 eV. Similarly, the metal Ru 3d peak parameters were obtained from a clean 3 nm ALD

metallic Ru film and kept locked at each experimental stage. The Ru 3d peak was fitted using a Doniach-Sunjic line profile to allow for the asymmetric nature of the metal peak.

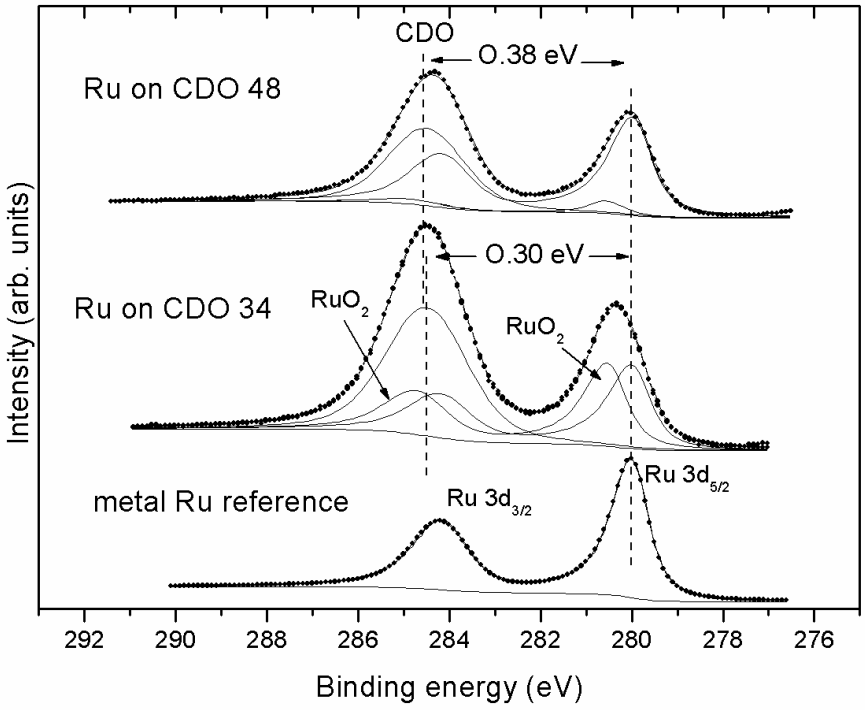

Figure 6.13 Ru 3d and C 1s spectra taken from a 3 nm metal Ru reference sample and a Ru thin film on two different carbon doped oxide surfaces. (BE positions in Ru 3d – Ru metal = 280.0 eV, RuO2 = 280.6 eV) All peak fitting parameters included in Appendix A.

The C 1s signals from both CDO samples arise on the higher binding energy (HBE) side of the metal Ru $3d_{3/2}$ spectra with a BE separation to the metal of ~0.30 eV and ~0.38 eV for CDO 34 and CDO 48, respectively. The chemical state of the deposited Ru on the high carbon content CDO 48 surface was largely metallic (~95%), with the presence of a small peak

separated from the metal by 0.7 eV on the HBE side associated with RuO_2 in agreement with Stoch et al.[13] However, there is a significantly higher Ru-oxide component peak in the Ru 3d peak profile following Ru deposition on the high porosity CDO 34 sample after thermal anneal. This would indicate evidence of a stronger chemical interaction between the Ru and the high porosity substrate in comparison with the high carbon content sample. A potential reason for this increased oxidation of the Ru may be due to the intrinsic higher surface area of the porous substrate resulting in a greater level of chemical interaction between the deposited Ru and the essentially three-dimensional surface. The corresponding Si 2p spectra for both substrates (not shown) do not change profile or peak position throughout the experiment suggesting that the basic chemical structure of the substrate remained unchanged by this interaction with the Ru overlayer. Likewise, there is no discernable change in the carbon peak profiles for either CDO substrate indicating no strong chemical interaction with the Ru other than oxidation. These experimental findings can only be extracted from the data by careful and consistent curve fitting, given the overlap between the C 1s and Ru $3d_{3/2}$ peaks.

Although it is important to understand the basic chemical interactions of Ru directly with CDO dielectric substrates and determine the relative binding energy peak positions of the core level electrons, the introduction of a

copper diffusion barrier layer between the Ru liner and the dielectric is more relevant from an industrial perspective. As such, in a separate experiment, approximately ~1 nm of metal Mn was deposited by in-situ e-beam evaporation on both CDO 34 And CDO 48 substrates in a UHV environment and the Mn/CDO structure was subsequently thermally annealed in an effort to produce a Mn-based copper diffusion barrier. It has been reported that Mn interacts with dielectric materials to produce Mn-silicate which is an effective barrier to copper diffusion.[1,2,10] The interaction of Mn on these particular CDO dielectric substrates has been documented in section 6.3, and as such this study will mainly focus on the subsequent deposition and interaction of Ru on the Mn/CDO structures. Figure 6.14 shows the Si 2p, C 1s and Ru 3d spectra after Mn-barrier formation and the subsequent Ru deposition on both CDO surfaces. The interaction of Mn with the two CDO substrates results in the growth of a peak on the LBE side of the C 1s associated with the formation of a Mn-carbide species. The ratio of the area of the carbide peak to that of the substrate is greater in the higher carbon content CDO 48 dielectric sample as may be expected. However, precise quantitative analysis of the relative amount of carbide formation in the two different CDO's was not performed as the metal Mn thickness could not be exactly reproduced in the two Mn depositions. In addition to Mn-carbide formation, the growth of a peak on the LBE side of the Si 2p CDO spectra suggests the release of Si from the substrates, an effect that has been

documented[14] and linked to the formation of Mn-silicate on the surface. However, the unambiguous identification of Mn-silicate could not be confirmed in this study due to the difficulty in resolving the Si 2p peaks as a result of almost identical binding energy positions of the CDO and Mn-silicate peaks. Figure 6.14 also shows the Si 2p, C 1s and Ru 3d spectra after the deposition of approximately ~1 nm of Ru on the Mn/CDO structure.

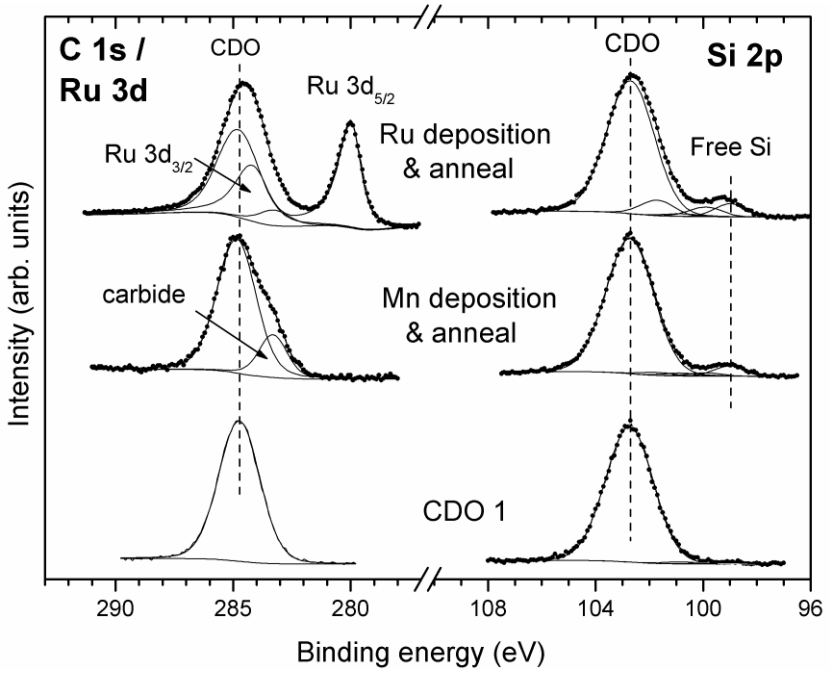

Figure 6.14(a) Ru 3d, C1s and Si 2p spectra taken from a Ru/Mn barrier/liner bilayer deposited on a high porosity carbon doped oxide surface. (BE position of Mn carbide ~283 eV).

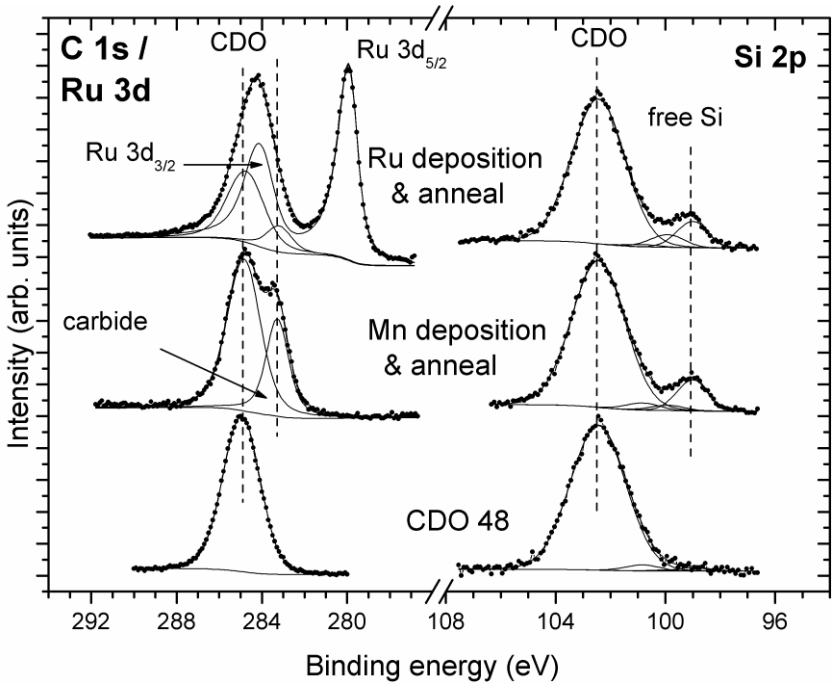

Figure 6.14(b) Ru 3d, C1s and Si 2p spectra taken from a thin Ru/Mn barrier/liner bilayer deposited on a high carbon content carbon doped oxide surface. (BE positions in Ru 3d – Ru metal = 280.0 eV, Mn carbide = 283.3 eV) All peak fitting parameters included in Appendix A.

The absence of a Ru-oxide peak in the high porosity CDO 34 sample is in contrast to the experiment where Ru was directly deposited on the dielectric in the absence of Mn, indicating that the Mn interlayer is effective at preventing the oxidation of the deposited Ru layer. The interaction of metal Mn with high porosity CDO dielectrics may also increase the oxidation of the Mn film, however this cannot be conclusively determined as the origin of any Mn-oxide contribution in the Mn 2p spectra could be due to chamber oxidation upon deposition which cannot be removed by thermal annealing in the same manner as Ru-oxide. As such, it is difficult to separate the Mn

oxide component which occurs as result of chamber oxidation and that which is due to the interaction with the dielectric. Careful peak fitting analysis indicates the metal Ru $3d_{3/2}$ peak has a binding energy position of 284.2 eV, which is situated between the C 1s and the Mn-carbide peaks in both CDO samples. There is some evidence that the area of the Mn-carbide C 1s peak reduced relative to that of the CDO C 1s upon Ru deposition in both samples. Given the complexity of the Ru 3d / C 1s spectrum further analysis would be required to ascertain any potential reduction of the Mn-carbide peak as a result of the interaction with Ru. It should be noted that Ru has been reported to reduce Mn-oxide.[15] The Si 2p spectra also indicates the presence of small component peaks on the HBE side of the free Si associated with the presence of Si sub oxides which occur as a result of the interaction of Mn with the CDO substrates. The peak fitting parameters used to fit the Ru $3d_{5/2}$ peak in Figure 6.14 (a) & (b) were identical to those acquired from the metal Ru reference film. As such, there was no evidence for the chemical interaction of the deposited Ru layer with any of the Mn species, including Mn carbide. The apparent stability of metal Ru films on Mn and oxidized Mn species is in agreement with Casey et. al,[15] however these results suggest Ru is also chemically stable in the presence of the Mn-carbide. The deposition of Si on CDO 34 and CDO 48 in the absence of Mn and Ru was performed in a separate experiment showing a BE separation of ~3.5 eV between the bulk/free Si^0 peak and the Si CDO substrate peaks,

correlating to that seen in Figure 6.14 and confirming the peak seen at 99 eV is free Si.

6.6 Conclusions

In summary, it has been shown that deposited Si can be used as an internal reference to determine accurate binding energy positions for XPS peaks from low-κ substrates of various carbon concentrations. Binding energy positions are otherwise difficult to determine on such substrates due to surface charging. The correlation between carbon content and binding energy position of the various substrates was seen within the Si 2p and O 1s spectra. Evidence for Mn-silicate formation on high carbon content CDO's was provided by careful analysis of the O 1s and Mn 2p spectra, as opposed to the usual method of analyzing the Si 2p. MnO was deposited and used as a reference material for the O 1s spectrum and an accurate binding energy position was achieved for the MnO in the O 1s. This approach produced some further evidence of a $MnSiO_3$ peak in the O 1s. Although this peak could still be another stoichiometry of MnO instead of a silicate, the Mn2p peaks also suggest it is in a Mn-silicate form.

Additionally, the surface treatment of carbon doped oxide layers by exposure to atomic oxygen has been demonstrated and investigated by XPS. It has been shown that the simultaneous depletion of carbon and addition of

oxygen at the dielectric surface modifies the chemical environment of the CDO providing a more suitable substrate for $MnSiO_3$ barrier layer formation. The altered binding energy positions of the Si 2p and O 1s core levels on the modified substrate enable the chemical identification of $MnSiO_3$, which is difficult on an untreated CDO surface due to peak overlap.

Finally, the relative peak positions of the Ru $3d_{3/2}$ and C 1s core level peaks were accurately determined in two industrially relevant Ru liner/CDO systems. The chemical, interactions of Ru layers with Mn-based barriers on CDO surfaces were also investigated. It was shown that a high porosity CDO surface appears to have an oxidizing effect on Ru liners. This chemical interaction was inhibited by the prior deposition and annealing of a thin Mn interlayer. Evidence for the metallic stability of Ru films on Mn species, including Mn-carbide, was demonstrated.

6.6 References

[1]P. Casey, J. Bogan, and G. Hughes, J. Appl. Phys. **110**, 054507 (2011).

[2]P. Casey, J. Bogan, B. Brennan, and G. Hughes, Appl. Phys. Lett. 98,113508 (2011).

[3]Y. Otsuka, J. Koike, H. Sako, K. Ishibashi, N. Kawasaki, S. M. Chung, and I. Tanaka, Appl. Phys. Lett. **96**, 012101 (2010).

[4]J. Koike and M. Wada, Appl. Phys. Lett. **87**, 041911 (2005).

[5]A. P. McCoy, P. Casey, J. Bogan, J. G. Lozano, P. D. Nellist, and G. Hughes, Appl. Phys. Lett. **101**, 231603 (2012).

[6]J. M. Ablett, J. C. Woicik, Z. Tokei, S. List, and E. Dimasi, Appl. Phys. Lett. **94**, 042112 (2009).

[7]C. J. Wilson, H. Volders, K. Croes, M. Pantouvaki, G. P. Beyer, A. B. Horsfall, A. G. O'Neill, and Z. Tokei, Microelectron. Eng. **87**, 398 (2010).

[8]Z. Tokei, K. Croes, and G. P. Beyer, Microelectron. Eng. **87**, 348 (2010).

[9]Y. Furukawa, R. Wolters, H. Roosen, J. H. M. Snijders, and R. Hoofman, Microelectron. Eng. **76**, 25 (2004).

[10]P. Casey, J. Bogan, and G. Hughes, J. Appl. Phys **110**, 124512 (2011)

[11] Y.H. Wang, R. Kumar, X. Zhou, J.S. Pan and J.W. Chai, Thin Solid Films **473**, 132 – 136 (2005).

[12]Y. Ohoka, Y. Ohba, A. Isobayashi, T. Hayashi, N. Komai, S. Arakawa, R. Kanamura, and S. Kadomura, International Interconnect Technology Conference (IEEE, New York, 2007), p. 67.

[13]Stoch J., Dao H.Q., Szeppe T., Bull. Polish. Acad. Sci. Chemistry. **35**, 387 (1987).

[14] A. P.McCoy., P.Casey., J. Bogan., C. Byrne., G. Hughes, *Appl. Phys. Lett.* ***102***, 201603-201603-4 (2013).

[15]P Casey, AP McCoy, J Bogan, C Byrne, L Walsh, R O'Connor, G Hughes The Journal of Physical Chemistry C **117** 16136-16143 (2014).

Chapter 7

Conclusions and future work

This thesis has focussed on issues related to the integration of Ru based copper diffusion barrier layers for future generations of interconnects. Details of the specific material systems are summarised below.

7.1 Mn and Mn oxide on 3 nm Ru thin films

Photoemission studies have shown that Mn can be diffused through a 3 nm ALD Ru thin film following thermal annealing at temperatures lower than 500 °C. It has also been shown using XPS analysis that diffused Mn interacts with the underlying SiO_2 dielectric substrate to form the Mn-silicate species $MnSiO_3$ which is known to be a barrier to Cu diffusion. The EELS profile of the Mn elemental distribution across the Ru layer supports this finding suggesting that Mn may be a suitable metal to 'stuff' the grain boundaries of Ru films thereby improving the integrity of the film as a barrier to Cu diffusion. It has also been shown that a thin deposited layer of partially oxidized Mn on a 3 nm ALD Ru film results in the diffusion of Mn through the Ru film and the subsequent formation of Mn-silicate at the Ru/SiO_2 interface upon anneal. EDX and SIMS analysis indicate that Si is released from the SiO_2 interface during the formation of interfacial silicate, and the free Si diffuses upward through the Ru film. XPS analysis indicates

the growth of a substantial quantity of Mn-silicate formed at both the Ru/SiO_2 interface and within the Mn/MnO_x deposited layer as a result of this upward Si diffusion. These results have implications for the integration of Ru/Mn layers into future interconnects in that the release of silicon from the underlying dielectric layer as a result of silicate formation could have detrimental consequences in terms of subsequent copper plating and operational longevity. This issue would need to be addressed if Ru/Mn is to be integrated into future devices.

7.2 Al on 3 nm Ru thin films

In a reference study, it has been shown that Al deposited on a 5.4 nm SiO_2 film results in the formation of Al_2O_3 during thermal anneal which is accompanied by the release of Si from the dielectric surface. In a separate experiment Al was deposited on a 3nm ALD Ru film and annealed to 500 °C. It was shown that thermal annealing results in the diffusion of Al through the liner layer and the subsequent chemical interaction with the underlying SiO_2 dielectric substrate to form Al_2O_3, Ru-silicide and Ru-oxide at the Ru/SiO_2 interface. XPS analysis of the Si 2p also indicates the concurrent release of Si from the SiO_2 dielectric layer. The chemical interaction of Si with Ru has also been shown which may have possible diffusion barrier layer applications.

7.3 Oxygen Catalysis on Ruthenium/Manganese Surfaces

The catalytic activity of bimetallic Ru/Mn surfaces towards molecular oxygen was investigated using a fully in-situ UHV experimental procedure, for the first time within the literature. XPS analysis performed following a controlled UHV O_2 exposure of 180 L showed that oxygen is dissociatively chemisorbed on the Ru/Mn surface to form MnO. Subsequent thermal annealing resulted in the dissociation of MnO as evidenced by the formation of metallic Mn along with evidence for the desorption of oxygen from the Ru/Mn surface. The dissociation of MnO at this temperature is in contrast to results taken from MnO control samples and as such it is suggested that the presence of Ru catalytically reduces the dissociation energy of MnO and the oxygen desorption energy. XPS spectra show no evidence of chemical changes in the Ru 3d spectra as a function of MnO dissociation, offering experimental evidence in agreement with the proposed mechanism for oxygen catalysis on bimetallic surfaces. The impact of Ru catalysis on the chemical composition and thermodynamic stability of preformed Mn-O based copper diffusion barrier layers was also investigated and showed that the presence of Ru layers results in the partial dissociation of both MnO and $MnSiO_3$ following a 500 °C thermal anneal. This result is again attributed to the catalytic activity of Ru/Mn surfaces reducing the dissociation energy of Mn-O bonds within the barrier layer region. However, it should also be

noted that the thermodynamic stability of the $MnSiO_3$ layers in the presence of Ru was higher than that of the MnO layers.

7.4 Ru / Mn based barrier layers on carbon doped oxide surfaces

It has been shown that deposited Si can be used as an internal reference to determine accurate binding energy positions for XPS peaks from low-κ substrates of various carbon concentrations. Binding energy positions are otherwise difficult to determine on such substrates due to surface charging. The correlation between carbon content and binding energy position of the various substrates was seen within the Si 2p and O 1s spectra. Evidence for Mn-silicate formation on high carbon content CDO's was provided by careful analysis of the O 1s and Mn 2p spectra, as opposed to the usual method of analyzing the Si 2p. MnO was deposited and used as a reference material for the O 1s spectrum and an accurate binding energy position was achieved for the MnO in the O 1s core level spectrum. This approach produced some further evidence of a $MnSiO_3$ peak in the O 1s peak profile. Although this peak could still be another stoichiometry of MnO instead of a silicate, the Mn 2p peaks also suggest it is in a Mn-silicate form. Additionally, the surface treatment of carbon doped oxide layers by exposure to atomic oxygen has been demonstrated and investigated by XPS. It has been shown that the simultaneous depletion of carbon and addition of oxygen at the dielectric surface modifies the chemical environment of the

CDO providing a more suitable substrate for $MnSiO_3$ barrier layer formation. The altered binding energy positions of the Si 2p and O 1s core levels on the modified substrate enable the chemical identification of $MnSiO_3$, which is difficult on an untreated CDO surface due to peak overlap.

Finally, the relative peak positions of the Ru $3d_{3/2}$ and C 1s core level peaks were accurately determined in two industrially relevant Ru liner/CDO systems. The chemical, interactions of Ru layers with Mn-based barriers on CDO surfaces were also investigated. It was shown that a high porosity CDO surface appears to have an oxidizing effect on Ru liners. This chemical interaction was inhibited by the prior deposition and annealing of a thin Mn interlayer. Evidence for the metallic stability of Ru films on Mn species, including Mn-carbide, was demonstrated.

7.5 Future work

The findings in this work provide the basis for further developing an understanding of Ru layers for use as copped diffusion barriers. Although an in depth chemical analysis of Ru liners was achieved using XPS, there was very little information on the structural aspect of the layers. Therefore, the barrier layer structures could be investigated using TEM while the copper diffusion barrier properties could be EELS elemental profiles to determine the effectiveness of the Ru/Mn and Ru/Al layers at inhibiting Cu diffusion.

Secondary ion mass spectroscopy analysis could also be used to determine the chemical depth profiles in conjunction with the EELS analysis. In addition to the barrier properties of Ru/Mn and Ru/Al structures, the diffusion mechanism of Mn, Cu and Al through these layers as a function of grain boundary density will also be assessed.

Metal-oxide-semiconductor (MOS) capacitor test structures formed by depositing copper on the Ru/Mn and Ru/Al based barrier layers formed on industrially relevant CDO dielectric substrates could also be used in the overall assessment of this barrier structures. The effectiveness of the layers at preventing copper diffusion could be determined by undertaking time-dependent dielectric breakdown (TDDB) and bias-temperature stress (BTS) measurements. Capacitance-voltage measurements could also be used to detect evidence of copper diffusion into the dielectric layer.

The concept of barrierless interconnects is also developing traction in the industry. The need for a barrier makes device miniaturisation very challenging due to the physical space requirement and the induced resistance of the layers. A potential solution based on the enhanced chemical and thermal stability of Cu alloys films has been proposed,[1] where the Cu interconnects are replaced with a new material system without the

need for a barrier layer. Ruthenium has been targeted as a potential material of interest for this purpose and will be studied in the coming year.[2]

7.6 References

[1] X.N. Li, L.J. Liu, X.Y. Zhang, J.P. Chu, Q. Wang, and C. Dong, Journal of Electronic Materials; **41**, No. 12 (2012).

[2] J. P. Chu, C. H. Lin, P. L. Sun, and W. K. Leaud, Journal of The Electrochemical Society; **156,** 7 H540-H543 (2009).

Appendix A

peak		BE position	Peak shape	Gaussian	Lorentzian
Si 2p	SiO2	103.8	Voigt	1.2	0.4
	Si	99.3	Voigt	0.6	0.4
	Ru silicide	99.6	Voigt	0.8	0.4
	MnSiO3	102.2	Voigt	1.4	0.4
	CDO 19	103.3	Voigt	1.8	0.4
	CDO 27	103.2	Voigt	1.7	0.4
	CDO 34	102.5	Voigt	1.7	0.4
	CDO 48	102.4	Voigt	1.8	0.4
O 1s	SiO2	532.7	Voigt	1.3	0.6
	Al2O3	531.9	Voigt	1.6	0.6
	MnO	530.1	Voigt	1	0.6
	MnSiO3	531.5	Voigt	1.9	0.6
	CDO 19	532.5	Voigt	2	0.6
	CDO 34	532.2	Voigt	1.9	0.6
	CDO 48	532.1	Voigt	1.9	0.6
Al 2p	Al metal	72.7	Voigt	0.8	0.1
	Al2O3	75.3	Voigt	1.8	0.1
Ru 3d	Ru metal	280.0	Don Sun	0.6	0.5
	Ru silicide	276.6	Don Sun	0.7	0.5
	RuO2	280.6	Voigt	1.1	0.5